



# Symbol-Based Analysis of Finite Element and Isogeometric B-Spline Discretizations of Eigenvalue Problems: Exposition and Review

Carlo Garoni<sup>1,2</sup> · Hendrik Speleers<sup>3</sup> · Sven-Erik Ekström<sup>4</sup> · Alessandro Reali<sup>5,6,7</sup> · Stefano Serra-Capizzano<sup>1,4</sup> · Thomas J. R. Hughes<sup>8</sup>

Received: 3 September 2018 / Accepted: 15 September 2018 / Published online: 7 January 2019  
© CIMNE, Barcelona, Spain 2019

## Abstract

We present an example-based exposition and review of recent advances in symbol-based spectral analysis. We consider constant- and variable-coefficient, second-order eigenvalue problems discretized through the (isogeometric) Galerkin method based on B-splines of degree  $p$  and smoothness  $C^k$ ,  $0 \leq k \leq p - 1$ . For each discretized problem, we compute the so-called symbol, which is a function describing the asymptotic singular value and eigenvalue distribution of the associated discretization matrices. Using the symbol, we are able to formulate analytical predictions for the eigenvalue errors occurring when the exact eigenvalues are approximated by the numerical eigenvalues. In this way, we recover and extend previous analytical spectral results. We are also able to predict the existence of  $p - k$  spectral branches, one “acoustical” and  $p - k - 1$  “optical”, when discretizing the one-dimensional Laplacian eigenvalue problem. We provide explicit and implicit analytical expressions for these branches, and we quantify the divergence to infinity with respect to  $p$  of the largest optical branch in the case of  $C^0$  smoothness (the case of classical finite element analysis).

## 1 Introduction

The two primary classes of mathematical techniques for studying finite element methods are functional analysis and spectral analysis. The purposes they serve tend to be complementary.

Functional analysis typically provides stability bounds, convergence proofs and error estimates in integral norms, and is applicable to unstructured meshes on complex geometries. It is fair to say that it is the mathematical standard for the finite element method. However, it often only provides asymptotic information, for example, the rate at which a measure of error decreases as mesh refinement is taken to the limit. In engineering, computations are not

---

✉ Alessandro Reali  
alessandro.reali@unipv.it

Carlo Garoni  
carlo.garoni@uninsubria.it

Hendrik Speleers  
speleers@mat.uniroma2.it

Sven-Erik Ekström  
sven-erik.ekstrom@it.uu.se

Stefano Serra-Capizzano  
stefano.serrac@uninsubria.it

Thomas J. R. Hughes  
hughes@ices.utexas.edu

<sup>1</sup> Department of Science and High Technology, University of Insubria, Como, Italy

<sup>2</sup> Institute of Computational Science, USI University, Lugano, Switzerland

<sup>3</sup> Department of Mathematics, University of Rome Tor Vergata, Rome, Italy

<sup>4</sup> Department of Information Technology, Uppsala University, Uppsala, Sweden

<sup>5</sup> Department of Civil Engineering and Architecture, University of Pavia, Pavia, Italy

<sup>6</sup> Institute of Applied Mathematics and Information Technology, CNR, Pavia, Italy

<sup>7</sup> Institute for Advanced Studies, Technical University of Munich, Munich, Germany

<sup>8</sup> Institute for Computational Engineering and Sciences, The University of Texas at Austin, Austin, TX, USA

performed in the limit. There may be, at most, a few meshes of different resolution, but usually there is only one, and the results for it are influenced by all eigenmodes composing the system, even ones that are not resolved at all, that is, not in the asymptotic range. This is well known in engineering circles and an issue of significant practical importance [18].

Spectral analysis typically provides a global portrait of *all* the modes comprising a discretization, that is, for a particular mesh, it reveals the precise errors in each eigenvalue and eigenfunction, from which the total error may be constructed for various classes of boundary and initial-value problems [20]. It often also provides results in analytical form, including explicit information about how parameters influence results. However, it is traditionally only applicable to highly structured situations, for example, uniform meshes with constant-coefficient differential operators, which are more typical of finite differences than finite elements. Consequently, it has played a minor role compared to functional analysis in the mathematical finite element literature.

Recent advances of spectral analysis have occurred in the mathematics literature that have extended its realm of applicability. As an example, we may mention that it is now possible to apply spectral analysis to differential equations with smoothly-varying, non-constant coefficients, using a geometry map and varying material properties. These advances have emerged from a deeper study of the *symbol*, a function associated with a sequence of Generalized Locally Toeplitz (GLT) matrices, which often arise in finite element and isogeometric discretizations of problems of practical interest. When the matrices are Hermitian (in particular, symmetric), one can extract information about the distribution of eigenvalues from the symbol.

In [20], the authors made the case for the importance of spectral analysis in understanding finite element and spline-based discretizations. Significant differences in the behavior of discretization procedures are often manifestly evident in spectral analysis, but entirely missed by functional analysis, and these are of the utmost importance in practical engineering problem solving. The purposes of this paper are to present an elementary, example-based exposition and review of the recent developments in symbol-based spectral analysis, accessible to the computational engineering community.

Consider a discretized version of a linear differential problem defined on a (uniform) mesh characterized by a discretization parameter  $n$  (related to the number of mesh elements), and let  $\mathbf{L}_n$  be the matrix associated with the linear discrete problem. The size of  $\mathbf{L}_n$  grows as  $n$  increases, that is, as the mesh is progressively refined, and ultimately we are left with a sequence of discretization

matrices  $\mathbf{L}_n$  such that  $\text{size}(\mathbf{L}_n) \rightarrow \infty$  as  $n \rightarrow \infty$ . What is often observed in practice is that the sequence  $\{\mathbf{L}_n\}_n$  is a GLT sequence and we can associate with  $\{\mathbf{L}_n\}_n$  a special function  $\mathbf{e}$ , the so-called symbol. The symbol describes the asymptotic distribution of the singular values of  $\mathbf{L}_n$ . In many cases, it also describes the asymptotic distribution of the eigenvalues of  $\mathbf{L}_n$ ; this happens, for example, if (but not only if) the matrices  $\mathbf{L}_n$  are Hermitian. The symbol may take values in the space of  $s \times s$  matrices for some  $s$  independent of  $n$ .

The theory of GLT sequences is a mathematically complicated machinery [25, 26] and will not be presented herein; the interested reader is referred to [14] for an introduction to this subject and to [1, 13–15, 17] for advanced studies. The precise definitions of asymptotic singular value and eigenvalue distributions for a given sequence of matrices  $\{\mathbf{L}_n\}_n$  are technical concepts and are stated in Appendix. Throughout this paper, we use the notation  $\{\mathbf{L}_n\}_n \sim_{\text{GLT}} \mathbf{e}$  to indicate that  $\{\mathbf{L}_n\}_n$  is a GLT sequence with symbol  $\mathbf{e}$ . Moreover, we write  $\{\mathbf{L}_n\}_n \sim_{\sigma} \mathbf{e}$  (resp.,  $\{\mathbf{L}_n\}_n \sim_{\lambda} \mathbf{e}$ ) whenever  $\{\mathbf{L}_n\}_n$  has an asymptotic singular value distribution (resp., eigenvalue distribution) described by  $\mathbf{e}$ . If both the relations  $\{\mathbf{L}_n\}_n \sim_{\sigma} \mathbf{e}$  and  $\{\mathbf{L}_n\}_n \sim_{\lambda} \mathbf{e}$  are satisfied, we sometimes write  $\{\mathbf{L}_n\}_n \sim_{\sigma, \lambda} \mathbf{e}$  for brevity.

In Sects. 2 and 3, which deal with the constant- and variable-coefficient cases, respectively, we will analyze several one-dimensional second-order eigenvalue problems discretized through the (isogeometric) Galerkin method based on B-splines of degree  $p$  and smoothness  $C^k$ ,  $0 \leq k \leq p - 1$ . In this specific context, we will illustrate:

- the practical procedures for computing symbols, that is, for proving relations such as  $\{\mathbf{L}_n\}_n \sim_{\text{GLT}} \mathbf{e}$ ;
- the practical meaning and the engineering implications of the eigenvalue distribution  $\{\mathbf{L}_n\}_n \sim_{\lambda} \mathbf{e}$ .

Among the implications, we will see that the symbol  $\mathbf{e}$  allows us to formulate analytical predictions for the eigenvalue errors occurring when the exact eigenvalues are approximated through the numerical eigenvalues. In this way, we will be able to recover and extend some of the analytical spectral results that have already appeared in the engineering literature [5, 20, 21, 23]. Using the symbol, we will also predict the existence of  $p - k$  spectral branches when discretizing the one-dimensional Laplacian eigenvalue problem by the Galerkin method based on B-splines of degree  $p$  and smoothness  $C^k$ . The first branch is known as the “acoustical branch” and provides good approximations to the Laplacian eigenvalues, while the other  $p - k - 1$  branches are the so-called “optical branches”, which are spurious and do not provide approximations to the Laplacian eigenvalues. In the case of maximal smoothness  $C^{p-1}$ ,

which is representative of Isogeometric Analysis (IgA) [4, 19], we will provide the analytical expression for all degrees  $p$  of the unique branch (the acoustical branch). In the case of minimal smoothness  $C^0$ , which is typical of classical Finite Element Analysis (FEA) [18], we have  $p$  different spectral branches (one acoustical and  $p - 1$  optical); we will provide implicit analytical expressions of these branches and we will quantify the divergence to infinity of the largest optical branch with respect to  $p$ .

## 2 Galerkin Discretization of the Laplacian Eigenvalue Problem

Consider the one-dimensional Laplacian eigenvalue problem:

$$\begin{cases} -u_j''(x) = \lambda_j u_j(x), & x \in (0, 1), \\ u_j(0) = u_j(1) = 0. \end{cases} \tag{2.1}$$

The corresponding weak formulation reads as follows: find eigenvalues  $\lambda_j \in \mathbb{R}^+$  and eigenfunctions  $u_j \in H_0^1([0, 1])$ , for  $j = 1, 2, \dots, \infty$ , such that, for all  $v \in H_0^1([0, 1])$ ,

$$a(u_j, v) = \lambda_j (u_j, v),$$

where

$$a(u_j, v) := \int_0^1 u_j'(x)v'(x)dx, \quad (u_j, v) := \int_0^1 u_j(x)v(x)dx.$$

In the Galerkin method, we first fix a set of basis functions  $\{\varphi_1, \dots, \varphi_{N_n}\} \subset H_0^1([0, 1])$  and define the approximation space  $\mathcal{W}_n := \text{span}(\varphi_1, \dots, \varphi_{N_n})$ . Then, we obtain approximations of the exact eigenpairs

$$\lambda_j := j^2 \pi^2, \quad u_j(x) := \sin(j\pi x), \quad j = 1, 2, \dots, \infty,$$

by solving the following Galerkin problem: find  $\lambda_{j,n} \in \mathbb{R}^+$  and  $u_{j,n} \in \mathcal{W}_n$ , for  $j = 1, \dots, N_n$ , such that, for all  $v_n \in \mathcal{W}_n$ ,

$$a(u_{j,n}, v_n) = \lambda_{j,n} (u_{j,n}, v_n). \tag{2.2}$$

Assuming the numerical eigenvalues  $\lambda_{j,n}$  are arranged in non-decreasing order, the pair  $(\lambda_{j,n}, u_{j,n})$  is taken as an approximation of the pair  $(\lambda_j, u_j)$  for all  $j = 1, \dots, N_n$ . The corresponding quantities

$$\frac{\lambda_{j,n} - \lambda_j}{\lambda_j} = \frac{\lambda_{j,n}}{\lambda_j} - 1, \quad j = 1, \dots, N_n,$$

are referred to as the (relative) eigenvalue errors.

In view of the canonical identification of each function  $v_n \in \mathcal{W}_n$  with its coefficient vector with respect to the basis  $\{\varphi_1, \dots, \varphi_{N_n}\}$ , solving the Galerkin problem (2.2) is equivalent to solving the generalized matrix eigenvalue problem

$$\mathbf{K}_n \mathbf{u}_{j,n} = \lambda_{j,n} \mathbf{M}_n \mathbf{u}_{j,n}, \tag{2.3}$$

where  $\mathbf{u}_{j,n}$  is the coefficient vector of  $u_{j,n}$  with respect to  $\{\varphi_1, \dots, \varphi_{N_n}\}$  and

$$\mathbf{K}_n := [a(\varphi_j, \varphi_i)]_{i,j=1}^{N_n} = \left[ \int_0^1 \varphi_j'(x)\varphi_i'(x)dx \right]_{i,j=1}^{N_n}, \tag{2.4}$$

$$\mathbf{M}_n := [(\varphi_j, \varphi_i)]_{i,j=1}^{N_n} = \left[ \int_0^1 \varphi_j(x)\varphi_i(x)dx \right]_{i,j=1}^{N_n}. \tag{2.5}$$

The matrices  $\mathbf{K}_n$  and  $\mathbf{M}_n$  are, respectively, the stiffness and mass matrices. Both  $\mathbf{K}_n$  and  $\mathbf{M}_n$  are always symmetric positive definite, regardless of the chosen basis functions  $\varphi_1, \dots, \varphi_{N_n}$ . Moreover, it is clear from (2.3) that the numerical eigenvalues  $\lambda_{j,n}$ ,  $j = 1, \dots, N_n$ , are just the eigenvalues of the matrix

$$\mathbf{L}_n := (\mathbf{M}_n)^{-1} \mathbf{K}_n. \tag{2.6}$$

### 2.1 Basics on B-Splines

We aim to use B-splines of various degree and smoothness on uniform meshes as the basis functions  $\varphi_1, \dots, \varphi_{N_n}$  in the discretization of (2.1). To this end, we start by recalling some basic properties of the B-splines of interest. For  $0 \leq k \leq p - 1$ , let  $\mathcal{V}_{n,[p,k]}$  be the space of functions in  $C^k([0, 1])$  that are piecewise polynomials of degree at most  $p$  on each subinterval  $[\frac{i}{n}, \frac{i+1}{n})$ ,  $i = 0, \dots, n - 1$ . In formulas,

$$\mathcal{V}_{n,[p,k]} := \{v \in C^k([0, 1]) : v|_{[\frac{i}{n}, \frac{i+1}{n})} \in \mathbb{P}_p \text{ for } i = 0, \dots, n - 1\},$$

where  $\mathbb{P}_p$  is the space of polynomials of degree at most  $p$ . We denote by

$$B_{i,[p,k]}, \quad i = 1, \dots, n(p - k) + k + 1, \tag{2.7}$$

the B-splines of degree  $p$  and smoothness  $C^k$  ( $0 \leq k \leq p - 1$ ) defined on the knot sequence

$$\{t_1, t_2, \dots, t_{n(p-k)+p+k+2}\} := \left\{ \underbrace{0, \dots, 0}_{p+1}, \underbrace{\frac{1}{n}, \dots, \frac{1}{n}}_{p-k}, \underbrace{\frac{2}{n}, \dots, \frac{2}{n}}_{p-k}, \dots, \underbrace{\frac{n-1}{n}, \dots, \frac{n-1}{n}}_{p-k}, \underbrace{1, \dots, 1}_{p+1} \right\}.$$

The B-splines (2.7) form a basis for the space  $\mathcal{V}_{n,[p,k]}$ . The support of the  $i$ -th B-spline is given by

$$\text{supp}(B_{i,[p,k]}) = [t_i, t_{i+p+1}], \quad i = 1, \dots, n(p - k) + k + 1. \tag{2.8}$$

Except for the first and the last one, all the other B-splines vanish on the boundary of  $[0, 1]$ , i.e.,

$$B_{i,[p,k]}(0) = B_{i,[p,k]}(1) = 0, \quad i = 2, \dots, n(p - k) + k.$$



$$\begin{bmatrix} \gamma_0 & \gamma_{-1} & \cdots & \gamma_{-t} \\ \gamma_1 & \ddots & \ddots & \ddots \\ \vdots & \ddots & \ddots & \ddots \\ \gamma_t & \ddots & \ddots & \ddots \end{bmatrix} = \mathbf{T}_m(g),$$

(2.10)

where

$$g(\theta) := \sum_{\ell=-t}^t \gamma_\ell e^{i\ell\theta}. \tag{2.11}$$

Indeed, by the orthogonality relations

$$\int_{-\pi}^{\pi} e^{i\ell\theta} e^{-ik\theta} d\theta = \begin{cases} 2\pi, & \text{if } k = \ell, \\ 0, & \text{if } k \neq \ell, \end{cases} \tag{2.12}$$

the function  $g$  in (2.11) satisfies

$$\hat{g}_k = \begin{cases} \gamma_k, & \text{if } k \in \{-t, \dots, t\}, \\ 0, & \text{otherwise,} \end{cases}$$

and so (2.10) follows from (2.9). The matrices  $\frac{1}{n}\mathbf{K}_n$  and  $n\mathbf{M}_n$  are then the  $(n - 1)$ -th Toeplitz matrices generated by, respectively,

$$f(\theta) := -e^{i\theta} + 2 - e^{-i\theta} = 2 - 2 \cos \theta,$$

and

$$h(\theta) := \frac{1}{6} (e^{i\theta} + 4 + e^{-i\theta}) = \frac{2}{3} + \frac{1}{3} \cos \theta.$$

It is known that  $\{\mathbf{T}_m(g)\}_m \sim_{\text{GLT}} g$  for all  $g$ , and so we obtain the relations

$$\left\{ \frac{1}{n} \mathbf{K}_n \right\}_n \sim_{\text{GLT}} f(\theta), \tag{2.13}$$

$$\left\{ n \mathbf{M}_n \right\}_n \sim_{\text{GLT}} h(\theta). \tag{2.14}$$

In other words,  $f(\theta)$  and  $h(\theta)$  are, respectively, the symbol of the sequence of normalized stiffness matrices  $\{\frac{1}{n}\mathbf{K}_n\}_n$  and the symbol of the sequence of normalized mass matrices  $\{n\mathbf{M}_n\}_n$ . As for the matrix  $\mathbf{L}_n := (\mathbf{M}_n)^{-1}\mathbf{K}_n$ , we observe that  $\frac{1}{n^2}\mathbf{L}_n$  is an algebraic combination of  $n\mathbf{M}_n$  and  $\frac{1}{n}\mathbf{K}_n$ , namely  $\frac{1}{n^2}\mathbf{L}_n = (n\mathbf{M}_n)^{-1}(\frac{1}{n}\mathbf{K}_n)$ . Since any algebraic combination of GLT sequences is again a GLT sequence

with its symbol given by the same algebraic combination of the symbols, we conclude that

$$\left\{ \frac{1}{n^2} \mathbf{L}_n \right\}_n \sim_{\text{GLT}} e(\theta) := (h(\theta))^{-1}f(\theta) = \frac{6(1 - \cos \theta)}{2 + \cos \theta}, \tag{2.15}$$

meaning that  $e(\theta)$  is the symbol of  $\{\frac{1}{n^2}\mathbf{L}_n\}_n$ . Figure 3 depicts the diagram used to compute the symbols  $f(\theta)$ ,  $h(\theta)$ ,  $e(\theta)$ . The relations (2.13)–(2.14) immediately imply the singular value distributions  $\{\frac{1}{n}\mathbf{K}_n\}_n \sim_{\sigma} f(\theta)$ ,  $\{n\mathbf{M}_n\}_n \sim_{\sigma} h(\theta)$  and also the eigenvalue distributions  $\{\frac{1}{n}\mathbf{K}_n\}_n \sim_{\lambda} f(\theta)$ ,  $\{n\mathbf{M}_n\}_n \sim_{\lambda} h(\theta)$  (because the matrices  $\mathbf{K}_n$  and  $\mathbf{M}_n$  are symmetric). Since it is not clear whether  $\mathbf{L}_n$  is symmetric or not, the relation (2.15) apparently ensures only the validity of the singular value distribution  $\{\frac{1}{n^2}\mathbf{L}_n\}_n \sim_{\sigma} e(\theta)$ . However, a symmetrization argument can be applied to show the validity of the eigenvalue distribution  $\{\frac{1}{n^2}\mathbf{L}_n\}_n \sim_{\lambda} e(\theta)$ . This argument is detailed in the following items:

- $\frac{1}{n^2}\mathbf{L}_n = (n\mathbf{M}_n)^{-1}(\frac{1}{n}\mathbf{K}_n)$  is similar to the symmetric matrix  $\frac{1}{n^2}\hat{\mathbf{L}}_n := (n\mathbf{M}_n)^{-1/2}(\frac{1}{n}\mathbf{K}_n)(n\mathbf{M}_n)^{-1/2}$ ;
- $\{\frac{1}{n^2}\hat{\mathbf{L}}_n\}_n \sim_{\text{GLT}} (h(\theta))^{-1/2}f(\theta)(h(\theta))^{-1/2} = e(\theta)$  by (2.13), (2.14) and the theory of GLT sequences;
- $\{\frac{1}{n^2}\hat{\mathbf{L}}_n\}_n \sim_{\lambda} e(\theta)$  because  $\{\frac{1}{n^2}\hat{\mathbf{L}}_n\}_n \sim_{\text{GLT}} e(\theta)$  and  $\frac{1}{n^2}\hat{\mathbf{L}}_n$  is symmetric;
- $\{\frac{1}{n^2}\mathbf{L}_n\}_n \sim_{\lambda} e(\theta)$  because  $\frac{1}{n^2}\mathbf{L}_n$  has the same eigenvalues as  $\frac{1}{n^2}\hat{\mathbf{L}}_n$ .

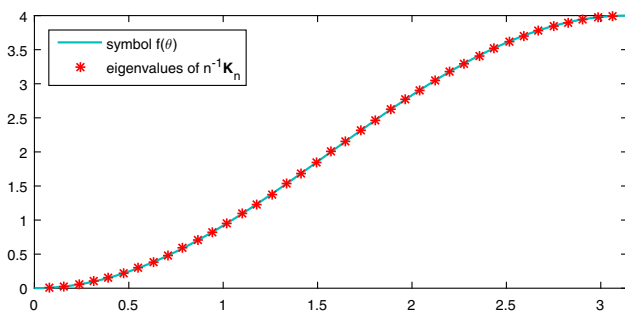
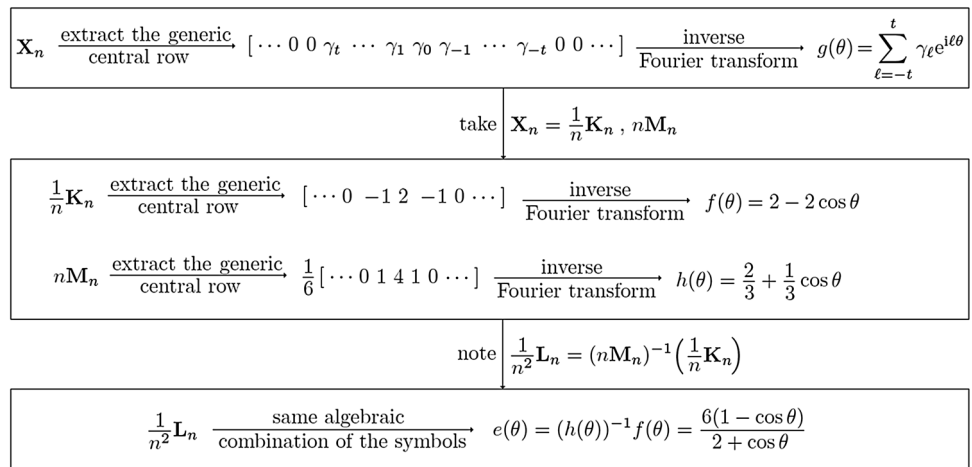
It is worth emphasizing that if a GLT relation such as  $\{\frac{1}{n^2}\mathbf{L}_n\}_n \sim_{\text{GLT}} e(\theta)$  is satisfied, the corresponding eigenvalue distribution  $\{\frac{1}{n^2}\mathbf{L}_n\}_n \sim_{\lambda} e(\theta)$  is often satisfied as well, even if a formal proof could be quite involved.

Figure 4 shows the graph of the symbol  $f(\theta)$  over  $[0, \pi]$  and the eigenvalues of  $\frac{1}{n}\mathbf{K}_n$  for  $n = 40$ . The eigenvalues  $\lambda_j(\frac{1}{n}\mathbf{K}_n)$ ,  $j = 1, \dots, n - 1$ , are sorted so as to match the graph of  $f(\theta)$  (i.e., in increasing order) and are represented by the red asterisks placed at the points  $(\frac{j\pi}{n}, \lambda_j(\frac{1}{n}\mathbf{K}_n))$ ,  $j = 1, \dots, n - 1$ . We see from the figure that the eigenvalues are (in this case) exact samples of the symbol  $f(\theta)$  over a uniform grid in  $[0, \pi]$ . This is no surprise as it is known for this case that

$$\lambda_j\left(\frac{1}{n}\mathbf{K}_n\right) = 2 - 2 \cos \frac{j\pi}{n}, \quad j = 1, \dots, n - 1.$$

Nevertheless, the present example highlights a general aspect: an asymptotic eigenvalue distribution relation such as  $\{\frac{1}{n}\mathbf{K}_n\}_n \sim_{\lambda} f(\theta)$ , with  $f(\theta)$  a scalar function, means that, for all sufficiently large  $n$ , the eigenvalues of  $\frac{1}{n}\mathbf{K}_n$  (except

**Fig. 3** Diagram for the computation of the symbols  $f(\theta)$ ,  $h(\theta)$ ,  $e(\theta)$



**Fig. 4** Linear  $C^0$  B-spline discretization: comparison between the symbol  $f(\theta)$  and the eigenvalues of  $\frac{1}{n} \mathbf{K}_n$  for  $n = 40$

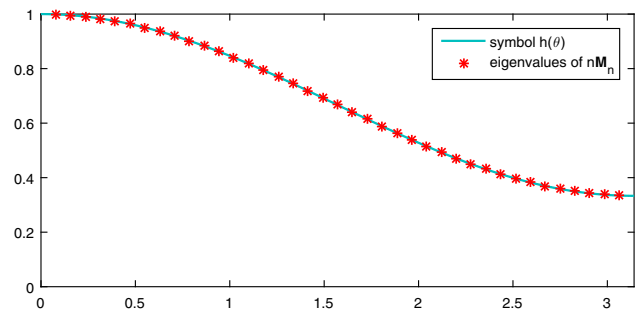


**Fig. 5** Linear  $C^0$  B-spline discretization: comparison between the symbol  $h(\theta)$  and the eigenvalues of  $n\mathbf{M}_n$  for  $n = 40$

possibly for a small number of outliers) are approximated by the samples of the function  $f(\theta)$  over a uniform grid in its domain. In our case the domain of  $f(\theta)$  is  $[-\pi, \pi]$ , but since  $f(\theta)$  is symmetric around  $\theta = 0$ , the eigenvalues of  $\frac{1}{n} \mathbf{K}_n$  are also approximated by the samples of  $f(\theta)$  over a uniform grid in  $[0, \pi]$ , as shown in Fig. 4. Figures 5 and 6 are the analogs of Fig. 4 for the cases of the symbols  $h(\theta)$ ,  $e(\theta)$  and the matrices  $n\mathbf{M}_n, \frac{1}{n^2} \mathbf{L}_n$ . Note that, contrary to the eigenvalues of  $\frac{1}{n} \mathbf{K}_n$  and  $\frac{1}{n^2} \mathbf{L}_n$ , the eigenvalues of  $n\mathbf{M}_n$  are arranged in decreasing order, so as to match the graph of  $h(\theta)$ . Also the eigenvalues of  $n\mathbf{M}_n$  and  $\frac{1}{n^2} \mathbf{L}_n$  are exact samples of the symbols  $h(\theta)$  and  $e(\theta)$  over a uniform grid in  $[0, \pi]$ , because

$$\lambda_j(n\mathbf{M}_n) = \frac{2}{3} + \frac{1}{3} \cos \frac{j\pi}{n}, \quad j = 1, \dots, n-1,$$

$$\lambda_j \left( \frac{1}{n^2} \mathbf{L}_n \right) = \frac{6(1 - \cos \frac{j\pi}{n})}{2 + \cos \frac{j\pi}{n}}, \quad j = 1, \dots, n-1.$$

This agrees with the interpretation of the relations  $\{n\mathbf{M}_n\}_n \sim_j h(\theta)$  and  $\{\frac{1}{n^2} \mathbf{L}_n\}_n \sim_j e(\theta)$ .

Considering that the eigenvalues of  $\frac{1}{n^2} \mathbf{L}_n$  (sorted in increasing order) are given by the uniform samples  $e(\frac{j\pi}{n})$ ,

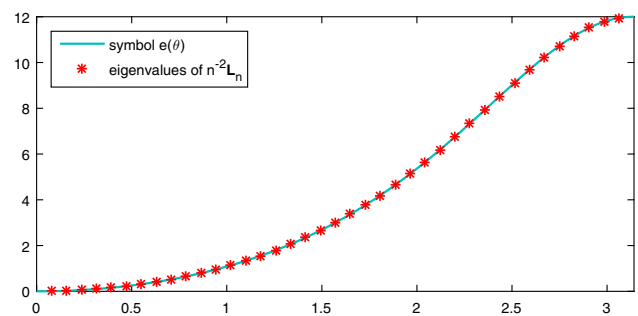


**Fig. 6** Linear  $C^0$  B-spline discretization: comparison between the symbol  $e(\theta)$  and the eigenvalues of  $\frac{1}{n^2} \mathbf{L}_n$  for  $n = 40$

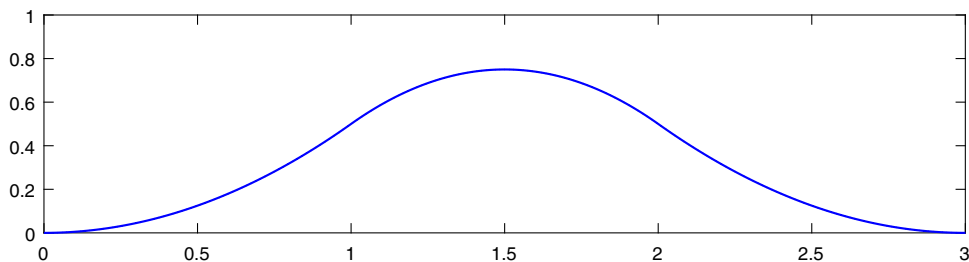
$j = 1, \dots, n-1$ , the eigenvalues of  $\mathbf{L}_n$  (i.e., the numerical eigenvalues  $\lambda_{j,n}$ ,  $j = 1, \dots, n-1$ ) are given by  $n^2 e(\frac{j\pi}{n})$ ,  $j = 1, \dots, n-1$ . Consequently, we have

$$\frac{\lambda_{j,n}}{\lambda_j} - 1 = \frac{e(\frac{j\pi}{n})}{\left(\frac{j\pi}{n}\right)^2} - 1, \quad j = 1, \dots, n-1.$$

In Fig. 7 we plot the analytical predictions  $e(\frac{j\pi}{n}) / (\frac{j\pi}{n})^2 - 1$  and the eigenvalue errors  $\lambda_{j,n} / \lambda_j - 1$  versus  $j / (n-1)$ , for



**Fig. 9** Reference quadratic  $C^1$  B-spline  $\phi_{[2,1]}$  defined on the knot sequence  $\{0, 1, 2, 3\}$



$$\{n\mathbf{M}_n\}_n \sim_{\text{GLT}} h(\theta). \tag{2.17}$$

Moreover, since  $\frac{1}{n^2}\mathbf{L}_n := (n\mathbf{M}_n)^{-1}(\frac{1}{n}\mathbf{K}_n)$  is an algebraic combination of  $n\mathbf{M}_n$  and  $\frac{1}{n}\mathbf{K}_n$ , we get

$$\begin{aligned} \left\{\frac{1}{n^2}\mathbf{L}_n\right\}_n &\sim_{\text{GLT}} e(\theta) := (h(\theta))^{-1}f(\theta) \\ &= \frac{20(3 - 2 \cos \theta - \cos(2\theta))}{33 + 26 \cos \theta + \cos(2\theta)}; \end{aligned} \tag{2.18}$$

this GLT relation holds for the same reason that we have seen in Sect. 2.2: any algebraic combination of GLT sequences is again a GLT sequence with its symbol given by the same algebraic combination of the symbols. In conclusion,  $f(\theta)$ ,  $h(\theta)$ ,  $e(\theta)$  are the symbols of  $\{\frac{1}{n}\mathbf{K}_n\}_n$ ,  $\{n\mathbf{M}_n\}_n$ ,  $\{\frac{1}{n^2}\mathbf{L}_n\}_n$ , respectively. Note that the diagram used to compute these symbols is conceptually the same as in Fig. 3. Indeed, the generic central row of  $\frac{1}{n}\mathbf{K}_n$  is

$$\frac{1}{6} [\cdots 0 \quad -1 \quad -2 \quad 6 \quad -2 \quad -1 \quad 0 \cdots],$$

and the generic central row of  $n\mathbf{M}_n$  is

$$\frac{1}{120} [\cdots 0 \quad 1 \quad 26 \quad 66 \quad 26 \quad 1 \quad 0 \cdots].$$

The relations (2.16)–(2.18) immediately imply the singular value distributions  $\{\frac{1}{n}\mathbf{K}_n\}_n \sim_{\sigma} f(\theta)$ ,  $\{n\mathbf{M}_n\}_n \sim_{\sigma} h(\theta)$ ,  $\{\frac{1}{n^2}\mathbf{L}_n\}_n \sim_{\sigma} e(\theta)$  and also the eigenvalue distributions  $\{\frac{1}{n}\mathbf{K}_n\}_n \sim_{\lambda} f(\theta)$ ,  $\{n\mathbf{M}_n\}_n \sim_{\lambda} h(\theta)$  (because  $\mathbf{K}_n$  and  $\mathbf{M}_n$  are symmetric). The eigenvalue distribution  $\{\frac{1}{n^2}\mathbf{L}_n\}_n \sim_{\lambda} e(\theta)$  follows from (2.18) and from the same symmetrization argument that we have applied in Sect. 2.2.

Figures 10, 11 and 12 show the graphs of the symbols  $f(\theta)$ ,  $h(\theta)$ ,  $e(\theta)$  over  $[0, \pi]$  and the eigenvalues of  $\frac{1}{n}\mathbf{K}_n$ ,  $n\mathbf{M}_n$ ,  $\frac{1}{n^2}\mathbf{L}_n$  for  $n = 40$ . The eigenvalues of  $\frac{1}{n}\mathbf{K}_n$  are sorted so as to match as much as possible the graph of the corresponding symbol  $f(\theta)$ , and are represented by the red asterisks placed at the points  $(\frac{j\pi}{n}, \lambda_j(\frac{1}{n}\mathbf{K}_n))$ ,  $j = 1, \dots, n$ . The same is true for the eigenvalues of  $n\mathbf{M}_n$  and  $\frac{1}{n^2}\mathbf{L}_n$ . We see from the figures that the eigenvalues of the three matrices  $\frac{1}{n}\mathbf{K}_n$ ,  $n\mathbf{M}_n$ ,  $\frac{1}{n^2}\mathbf{L}_n$  are approximately samples

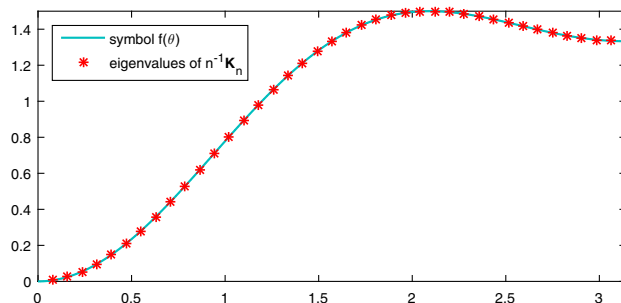


**Fig. 10** Quadratic  $C^1$  B-spline discretization: comparison between the symbol  $f(\theta)$  and the eigenvalues of  $\frac{1}{n}\mathbf{K}_n$  for  $n = 40$

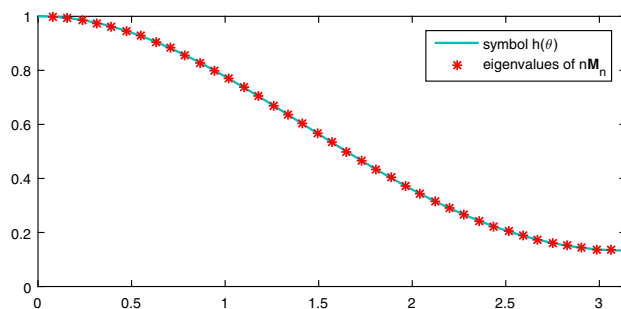


**Fig. 11** Quadratic  $C^1$  B-spline discretization: comparison between the symbol  $h(\theta)$  and the eigenvalues of  $n\mathbf{M}_n$  for  $n = 40$

(apparently, exact samples) of the symbols  $f(\theta)$ ,  $h(\theta)$ ,  $e(\theta)$  over a uniform grid in  $[0, \pi]$ . This agrees with the interpretation of the asymptotic eigenvalue distributions  $\{\frac{1}{n}\mathbf{K}_n\}_n \sim_{\lambda} f(\theta)$ ,  $\{n\mathbf{M}_n\}_n \sim_{\lambda} h(\theta)$ ,  $\{\frac{1}{n^2}\mathbf{L}_n\}_n \sim_{\lambda} e(\theta)$  given before (see Sect. 2.2).

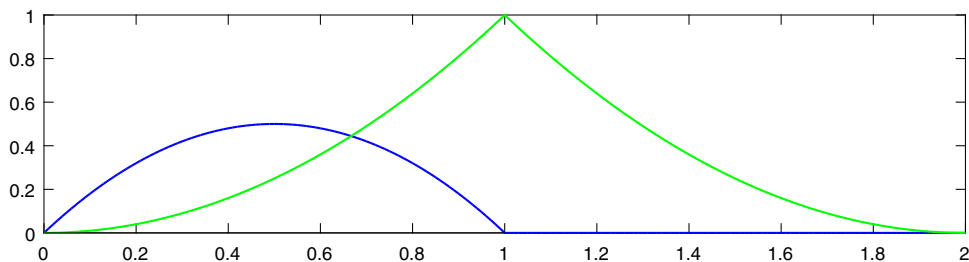
Considering that the eigenvalues of  $\frac{1}{n^2}\mathbf{L}_n$  (sorted in increasing order) are approximated by the uniform samples  $e(\frac{j\pi}{n})$ ,  $j = 1, \dots, n$ , the eigenvalues of  $\mathbf{L}_n$  (i.e., the numerical eigenvalues  $\lambda_{j,n}$ ,  $j = 1, \dots, n$ ) are approximated by  $n^2 e(\frac{j\pi}{n})$ ,  $j = 1, \dots, n$ . Consequently, we have

$$\frac{\lambda_{j,n}}{\lambda_j} - 1 \approx \frac{e(\frac{j\pi}{n})}{(\frac{j\pi}{n})^2} - 1, \quad j = 1, \dots, n.$$

In Fig. 13 we plot the analytical predictions  $e(\frac{j\pi}{n})/(\frac{j\pi}{n})^2 - 1$  and the eigenvalue errors  $\lambda_{j,n}/\lambda_j - 1$  versus  $j/n$ , for



**Fig. 15** Reference quadratic  $C^0$  B-splines  $\phi_{1,[2,0]}, \phi_{2,[2,0]}$  defined on the knot sequence  $\{0, 0, 1, 1, 2\}$



$$\mathbf{T}_m(\mathbf{g}) := \begin{bmatrix} \hat{\mathbf{g}}_0 & \hat{\mathbf{g}}_{-1} & \cdots & \cdots & \hat{\mathbf{g}}_{-(m-1)} \\ \hat{\mathbf{g}}_1 & \ddots & \ddots & & \vdots \\ \vdots & \ddots & \ddots & \ddots & \vdots \\ \vdots & & \ddots & \ddots & \hat{\mathbf{g}}_{-1} \\ \hat{\mathbf{g}}_{m-1} & \cdots & \cdots & \hat{\mathbf{g}}_1 & \hat{\mathbf{g}}_0 \end{bmatrix} \quad (2.19)$$

is referred to as the  $m$ -th (block) Toeplitz matrix generated by  $\mathbf{g}$ . In particular, for any fixed  $t \in \mathbb{N}$  and  $\gamma_{-t}, \dots, \gamma_t \in \mathbb{C}^{s \times s}$  we have

$$\begin{bmatrix} \gamma_0 & \gamma_{-1} & \cdots & \gamma_{-t} \\ \gamma_1 & \ddots & \ddots & \ddots & \ddots \\ \vdots & \ddots & \ddots & \ddots & \ddots \\ \gamma_t & & & & \\ \vdots & & & & \\ \vdots & & & & \\ \gamma_t & \cdots & \gamma_1 & \gamma_0 & \gamma_{-1} & \cdots & \gamma_{-t} \\ \vdots & & & & & & \vdots \\ \vdots & & & & & & \gamma_{-1} \\ \vdots & & & & & & \gamma_0 \end{bmatrix} = \mathbf{T}_m(\mathbf{g}), \quad (2.20)$$

where

$$\mathbf{g}(\theta) := \sum_{\ell=-t}^t \gamma_\ell e^{i\ell\theta}. \quad (2.21)$$

Just like (2.10)–(2.11), Eqs. (2.20)–(2.21) follow from the orthogonality relations (2.12), which imply that the matrix-valued function  $\mathbf{g}$  in (2.21) satisfies

$$\hat{\mathbf{g}}_k = \begin{cases} \gamma_k, & \text{if } k \in \{-t, \dots, t\}, \\ 0, & \text{otherwise.} \end{cases}$$

The matrix  $\frac{1}{n} \mathbf{K}_n$  (resp.,  $n \mathbf{M}_n$ ) contains as a principal submatrix the Toeplitz matrix  $\mathbf{T}_{n-1}(\mathbf{f})$  (resp.,  $\mathbf{T}_{n-1}(\mathbf{h})$ ), where  $\mathbf{f}(\theta)$  and  $\mathbf{h}(\theta)$  are the  $2 \times 2$  matrix-valued functions given by

$$\begin{aligned} \mathbf{f}(\theta) &:= \frac{1}{3} \left( \begin{bmatrix} 0 & -2 \\ 0 & -2 \end{bmatrix} e^{i\theta} + \begin{bmatrix} 4 & -2 \\ -2 & 8 \end{bmatrix} + \begin{bmatrix} 0 & 0 \\ -2 & -2 \end{bmatrix} e^{-i\theta} \right) \\ &= \frac{1}{3} \begin{bmatrix} 4 & -2 - 2e^{i\theta} \\ -2 - 2e^{-i\theta} & 8 - 4 \cos \theta \end{bmatrix}, \end{aligned}$$

and

$$\begin{aligned} \mathbf{h}(\theta) &:= \frac{1}{30} \left( \begin{bmatrix} 0 & 3 \\ 0 & 1 \end{bmatrix} e^{i\theta} + \begin{bmatrix} 4 & 3 \\ 3 & 12 \end{bmatrix} + \begin{bmatrix} 0 & 0 \\ 3 & 1 \end{bmatrix} e^{-i\theta} \right) \\ &= \frac{1}{30} \begin{bmatrix} 4 & 3 + 3e^{i\theta} \\ 3 + 3e^{-i\theta} & 12 + 2 \cos \theta \end{bmatrix}. \end{aligned}$$

Since  $\{\mathbf{T}_m(\mathbf{g})\}_m \sim_{\text{GLT}} \mathbf{g}$  for all  $\mathbf{g}$ , the theory of GLT sequences yields

$$\left\{ \frac{1}{n} \mathbf{K}_n \right\}_n \sim_{\text{GLT}} \mathbf{f}(\theta), \quad (2.22)$$

$$\left\{ n \mathbf{M}_n \right\}_n \sim_{\text{GLT}} \mathbf{h}(\theta). \quad (2.23)$$

Moreover, since any algebraic combination of GLT sequences such as  $\frac{1}{n^2} \mathbf{L}_n := (n \mathbf{M}_n)^{-1} (\frac{1}{n} \mathbf{K}_n)$  is again a GLT sequence with its symbol given by the same algebraic combination of the symbols, we get

$$\begin{aligned} \left\{ \frac{1}{n^2} \mathbf{L}_n \right\}_n &\sim_{\text{GLT}} \mathbf{e}(\theta) := (\mathbf{h}(\theta))^{-1} \mathbf{f}(\theta) \\ &= \frac{4}{3 - \cos \theta} \begin{bmatrix} 15 + 5 \cos \theta & (\cos \theta - 6)(2 + 2e^{i\theta}) \\ -5 - 5e^{-i\theta} & 11 - \cos \theta \end{bmatrix}. \end{aligned} \quad (2.24)$$

In conclusion,  $\mathbf{f}(\theta)$ ,  $\mathbf{h}(\theta)$ ,  $\mathbf{e}(\theta)$  are the symbols of  $\{\frac{1}{n} \mathbf{K}_n\}_n$ ,  $\{n \mathbf{M}_n\}_n$ ,  $\{\frac{1}{n^2} \mathbf{L}_n\}_n$ , respectively. Figure 16 depicts the diagram used to compute the symbols  $\mathbf{f}(\theta)$ ,  $\mathbf{h}(\theta)$ ,  $\mathbf{e}(\theta)$ . The relations (2.22)–(2.24) immediately imply the singular value distributions  $\{\frac{1}{n} \mathbf{K}_n\}_n \sim_\sigma \mathbf{f}(\theta)$ ,  $\{n \mathbf{M}_n\}_n \sim_\sigma \mathbf{h}(\theta)$ ,  $\{\frac{1}{n^2} \mathbf{L}_n\}_n \sim_\sigma \mathbf{e}(\theta)$  and the eigenvalue distributions  $\{\frac{1}{n} \mathbf{K}_n\}_n \sim_\lambda \mathbf{f}(\theta)$ ,  $\{n \mathbf{M}_n\}_n \sim_\lambda \mathbf{h}(\theta)$  (because  $\mathbf{K}_n$  and  $\mathbf{M}_n$  are symmetric). The eigenvalue distribution  $\{\frac{1}{n^2} \mathbf{L}_n\}_n \sim_\lambda \mathbf{e}(\theta)$  follows from (2.24) and from a symmetrization argument completely analogous to the one in Sect. 2.2.

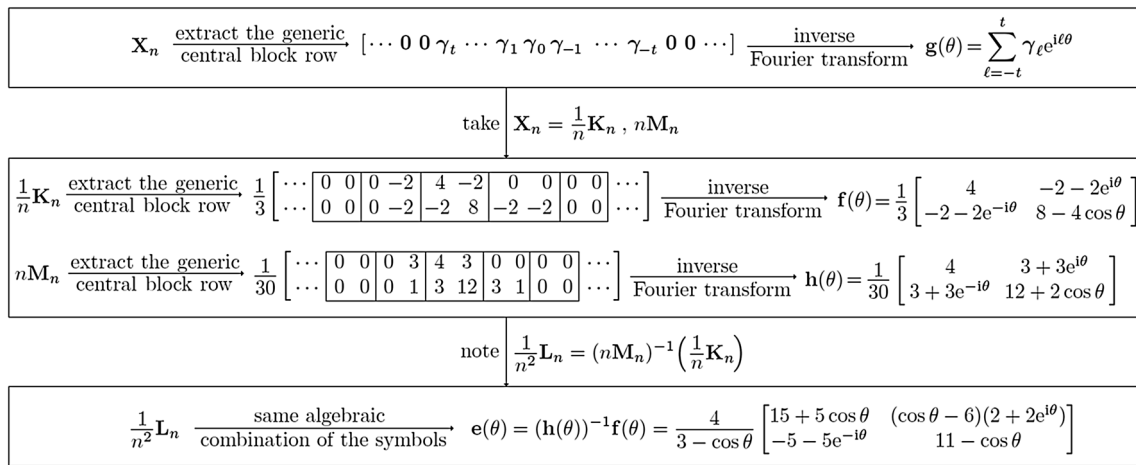


Fig. 16 Diagram for the computation of the symbols  $\mathbf{f}(\theta)$ ,  $\mathbf{h}(\theta)$ ,  $\mathbf{e}(\theta)$

The eigenvalues of  $\mathbf{f}(\theta)$ ,  $\mathbf{h}(\theta)$ ,  $\mathbf{e}(\theta)$  are given by

$$\lambda_{1,2}(\mathbf{f}(\theta)) = 2 - \frac{2}{3} \cos \theta \mp \frac{2}{3} \sqrt{3 + \cos^2 \theta},$$

$$\lambda_{1,2}(\mathbf{h}(\theta)) = \frac{4}{15} + \frac{1}{30} \cos \theta \mp \frac{1}{30} \sqrt{34 + 26 \cos \theta + \cos^2 \theta},$$

$$\lambda_{1,2}(\mathbf{e}(\theta)) = \frac{4(13 + 2 \cos \theta \mp \sqrt{124 + 112 \cos \theta - 11 \cos^2 \theta})}{3 - \cos \theta}.$$

Figure 17 shows the graphs of the eigenvalue functions  $\lambda_{1,2}(\mathbf{f}(\theta))$  over  $[0, \pi]$ , and the eigenvalues of  $\frac{1}{n} \mathbf{K}_n$  for  $n = 40$ . The eigenvalues  $\lambda_j(\frac{1}{n} \mathbf{K}_n)$ ,  $j = 1, \dots, 2n - 1$ , are sorted so as to match the graphs of the eigenvalue functions (i.e., in increasing order) and are represented in the figure by the red asterisks placed at the points  $(\frac{j\pi}{n}, \lambda_j(\frac{1}{n} \mathbf{K}_n))$ ,  $j = 1, \dots, n$ , and  $(\frac{(j-n)\pi}{n}, \lambda_j(\frac{1}{n} \mathbf{K}_n))$ ,  $j = n + 1, \dots, 2n - 1$ . We see from the figure that the eigenvalues of  $\frac{1}{n} \mathbf{K}_n$  can be subdivided into two different subsets of approximately the same cardinality, and the eigenvalues of the first (resp., second) subset are approximately samples of  $\lambda_1(\mathbf{f}(\theta))$  (resp.,  $\lambda_2(\mathbf{f}(\theta))$ ) over a uniform grid in  $[0, \pi]$ . This highlights a general aspect: an asymptotic eigenvalue distribution relation such as  $\{\frac{1}{n} \mathbf{K}_n\}_n \sim_\lambda \mathbf{f}(\theta)$ , with  $\mathbf{f}(\theta)$  an  $s \times s$

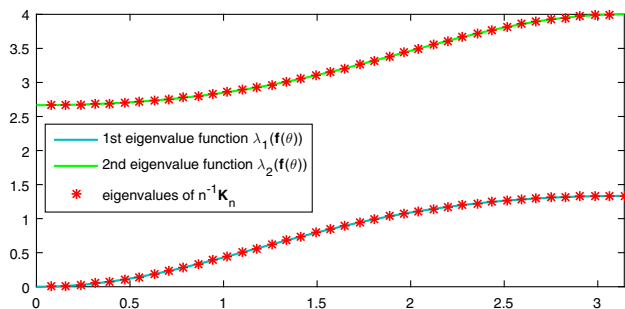


Fig. 17 Quadratic  $C^0$  B-spline discretization: comparison between the symbol  $\mathbf{f}(\theta)$  and the eigenvalues of  $\frac{1}{n} \mathbf{K}_n$  for  $n = 40$

matrix-valued function, means that, for all sufficiently large  $n$ , the eigenvalues of  $\frac{1}{n} \mathbf{K}_n$  can be subdivided into  $s$  different subsets of approximately the same cardinality; and the eigenvalues belonging to the  $i$ -th subset (except possibly for a small number of outliers) are approximated by the samples of the  $i$ -th eigenvalue function  $\lambda_i(\mathbf{f}(\theta))$  over a uniform grid in the domain of  $\mathbf{f}(\theta)$ . In our case the domain of  $\mathbf{f}(\theta)$  is  $[-\pi, \pi]$ , but since the eigenvalue functions  $\lambda_{1,2}(\mathbf{f}(\theta))$  are symmetric around  $\theta = 0$ , the eigenvalues of  $\frac{1}{n} \mathbf{K}_n$  are also approximated by their samples over a uniform grid in  $[0, \pi]$ , as shown in Fig. 17. It is important to observe that the two subsets of the spectrum of  $\frac{1}{n} \mathbf{K}_n$  corresponding to the two eigenvalue functions  $\lambda_1(\mathbf{f}(\theta))$  and  $\lambda_2(\mathbf{f}(\theta))$ , i.e., the subsets  $\{\lambda_j(\frac{1}{n} \mathbf{K}_n), j = 1, \dots, n\}$  and  $\{\lambda_j(\frac{1}{n} \mathbf{K}_n), j = n + 1, \dots, 2n - 1\}$ , are well separated from each other, due to the fact that

$$\max_{\theta} \lambda_1(\mathbf{f}(\theta)) < \min_{\theta} \lambda_2(\mathbf{f}(\theta)).$$

For this reason we say that the spectrum of  $\frac{1}{n} \mathbf{K}_n$  is composed of two branches, which are precisely the two subsets  $\{\lambda_j(\frac{1}{n} \mathbf{K}_n), j = 1, \dots, n\}$  and  $\{\lambda_j(\frac{1}{n} \mathbf{K}_n), j = n + 1, \dots, 2n - 1\}$  corresponding to the two eigenvalue functions  $\lambda_1(\mathbf{f}(\theta))$

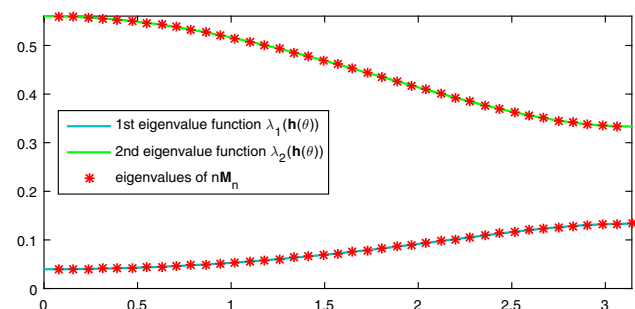
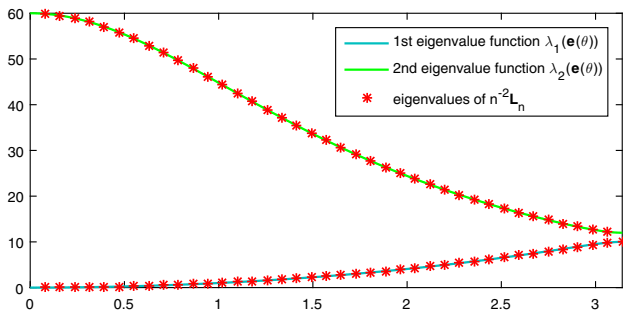
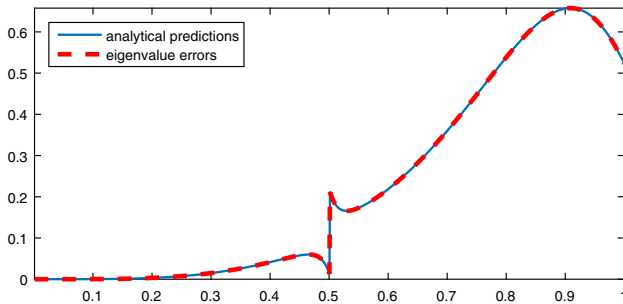


Fig. 18 Quadratic  $C^0$  B-spline discretization: comparison between the symbol  $\mathbf{h}(\theta)$  and the eigenvalues of  $n\mathbf{M}_n$  for  $n = 40$



**Fig. 19** Quadratic  $C^0$  B-spline discretization: comparison between the symbol  $\mathbf{e}(\theta)$  and the eigenvalues of  $\frac{1}{n^2}\mathbf{L}_n$  for  $n = 40$



**Fig. 20** Quadratic  $C^0$  B-spline discretization: analytical predictions  $w_j/(\frac{j\pi}{n})^2 - 1$  and eigenvalue errors  $\lambda_{j,n}/\lambda_j - 1$  versus  $j/N_n$ ,  $j = 1, \dots, N_n$  ( $N_n = 2n - 1$ ,  $n = 500$ )

and  $\lambda_2(\mathbf{f}(\theta))$ . Figures 18 and 19 are the analogs of Fig. 17 for the cases of the symbols  $\mathbf{h}(\theta)$ ,  $\mathbf{e}(\theta)$  and the matrices  $n\mathbf{M}_n$ ,  $\frac{1}{n^2}\mathbf{L}_n$ . They confirm the eigenvalue distributions  $\{n\mathbf{M}_n\}_n \sim_\lambda \mathbf{h}(\theta)$  and  $\{\frac{1}{n^2}\mathbf{L}_n\}_n \sim_\lambda \mathbf{e}(\theta)$ , and show that the spectra of  $n\mathbf{M}_n$  and  $\frac{1}{n^2}\mathbf{L}_n$  are composed of two branches, just like the spectrum of  $\frac{1}{n}\mathbf{K}_n$ .

Considering that the eigenvalues of  $\frac{1}{n^2}\mathbf{L}_n$  (sorted in increasing order) are approximated by the uniform samples  $\lambda_1(\mathbf{e}(\frac{j\pi}{n}))$ ,  $j = 1, \dots, n$ , and  $\lambda_2(\mathbf{e}(\frac{(2n-j)\pi}{n}))$ ,  $j = n + 1, \dots, 2n - 1$ , the eigenvalues of  $\mathbf{L}_n$  (i.e., the numerical eigenvalues  $\lambda_{j,n}$ ,  $j = 1, \dots, 2n - 1$ ) are approximated by the values  $n^2\lambda_1(\mathbf{e}(\frac{j\pi}{n}))$ ,  $j = 1, \dots, n$ , and  $n^2\lambda_2(\mathbf{e}(\frac{(2n-j)\pi}{n}))$ ,

$j = n + 1, \dots, 2n - 1$ . Consequently, we have

$$\frac{\lambda_{j,n}}{\lambda_j} - 1 \approx \frac{w_j}{(\frac{j\pi}{n})^2} - 1, \quad j = 1, \dots, 2n - 1,$$

where

$$w_j := \begin{cases} \lambda_1\left(\mathbf{e}\left(\frac{j\pi}{n}\right)\right), & j = 1, \dots, n, \\ \lambda_2\left(\mathbf{e}\left(\frac{(2n-j)\pi}{n}\right)\right), & j = n + 1, \dots, 2n - 1. \end{cases}$$

In Fig. 20 we plot the analytical predictions  $w_j/(\frac{j\pi}{n})^2 - 1$  and the eigenvalue errors  $\lambda_{j,n}/\lambda_j - 1$  versus  $j/(2n - 1)$ , for  $j = 1, \dots, 2n - 1$  and  $n = 500$ . Clearly, the analytical prediction is excellent. Note that the two branches in the spectrum of  $\frac{1}{n^2}\mathbf{L}_n$ , which are visible in Fig. 19, also produce in Fig. 20 two branches separated by the jump at  $j/N_n \approx 1/2$  ( $N_n = 2n - 1$ ). The location of this jump at  $1/2$  is a consequence of the relation  $\{\frac{1}{n^2}\mathbf{L}_n\}_n \sim_\lambda \mathbf{e}(\theta)$ , according to which one half of the spectrum of  $\frac{1}{n^2}\mathbf{L}_n$  is described by the first eigenvalue function  $\lambda_1(\mathbf{e}(\theta))$  and the other half is described by the second eigenvalue function  $\lambda_2(\mathbf{e}(\theta))$ .

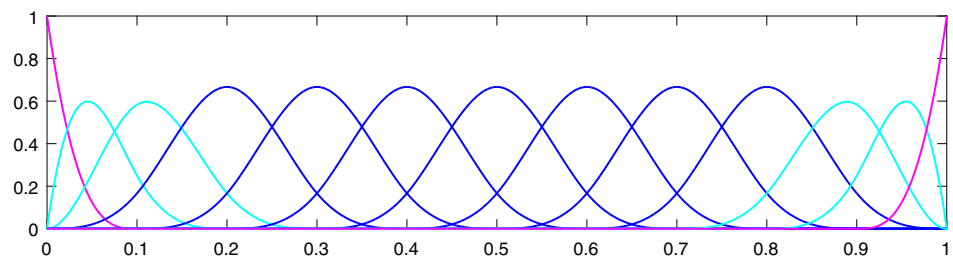
### 2.4 Cubic $C^k$ B-Spline Discretization

In this section we address cubic B-spline discretizations of (2.1) on uniform meshes, varying consecutively the smoothness from  $C^2$  to  $C^0$ .

#### 2.4.1 Cubic $C^2$ B-Spline Discretization

In the cubic  $C^2$  B-spline discretization on a uniform mesh with stepsize  $\frac{1}{n}$ , the basis functions  $\varphi_1, \dots, \varphi_{N_n}$  are chosen as the B-splines  $B_{2,[3,2]}, \dots, B_{n+2,[3,2]}$ ; see Fig. 21. Except for the four boundary functions in cyan, the basis functions are uniformly shifted-scaled versions of the fixed reference B-spline  $\phi_{[3,2]}$  in Fig. 22, which is the  $C^2$  B-spline of degree 3 defined on the knot sequence  $\{0, 1, 2, 3, 4\}$ . The resulting normalized stiffness and mass matrices are given by

**Fig. 21** Cubic  $C^2$  B-splines  $\{B_{1,[3,2]}, \dots, B_{n+3,[3,2]}\}$  defined on the knot sequence  $\{0, 0, 0, 0, \frac{1}{n}, \frac{2}{n}, \dots, \frac{n-1}{n}, 1, 1, 1, 1\}$  for  $n = 10$





$\{\mathbf{T}_{n+1}(f)\}_n \sim_{\text{GLT}} f(\theta)$  and  $\{\mathbf{T}_{n+1}(h)\}_n \sim_{\text{GLT}} h(\theta)$ , the theory of GLT sequences yields

$$\left\{ \frac{1}{n} \mathbf{K}_n \right\}_n \sim_{\text{GLT}} f(\theta), \tag{2.25}$$

$$\left\{ n \mathbf{M}_n \right\}_n \sim_{\text{GLT}} h(\theta), \tag{2.26}$$

and for  $\mathbf{L}_n := (\mathbf{M}_n)^{-1} \mathbf{K}_n$ ,

$$\left\{ \frac{1}{n^2} \mathbf{L}_n \right\}_n \sim_{\text{GLT}} e(\theta) := (h(\theta))^{-1} f(\theta) \tag{2.27}$$

$$= \frac{42(40 - 15 \cos \theta - 24 \cos(2\theta) - \cos(3\theta))}{1208 + 1191 \cos \theta + 120 \cos(2\theta) + \cos(3\theta)},$$

i.e.,  $f(\theta)$ ,  $h(\theta)$ ,  $e(\theta)$  are the symbols of  $\{\frac{1}{n} \mathbf{K}_n\}_n$ ,  $\{n \mathbf{M}_n\}_n$ ,  $\{\frac{1}{n^2} \mathbf{L}_n\}_n$ , respectively. The diagram used to compute these symbols is the same as in Fig. 3. Through the same line of argument used in the previous sections, one can show that (2.25)–(2.27) imply the singular value and eigenvalue distributions  $\{\frac{1}{n} \mathbf{K}_n\}_n \sim_{\sigma, \lambda} f(\theta)$ ,  $\{n \mathbf{M}_n\}_n \sim_{\sigma, \lambda} h(\theta)$ , and  $\{\frac{1}{n^2} \mathbf{L}_n\}_n \sim_{\sigma, \lambda} e(\theta)$ .

Figure 23 shows the graph of the symbol  $f(\theta)$  over  $[0, \pi]$  and the eigenvalues of  $\frac{1}{n} \mathbf{K}_n$  for  $n = 40$ . The eigenvalues  $\lambda_j(\frac{1}{n} \mathbf{K}_n)$ ,  $j = 1, \dots, n + 1$ , are represented by the red asterisks placed at the points  $(\frac{j\pi}{n}, \lambda_j(\frac{1}{n} \mathbf{K}_n))$ ,  $j = 1, \dots, n + 1$ ; they are sorted so as to match the graph of the symbol  $f(\theta)$ . Note that the last eigenvalue  $\lambda_{n+1}(\frac{1}{n} \mathbf{K}_n)$  is positioned at  $\frac{(n+1)\pi}{n}$  (outside the domain  $[0, \pi]$ ) and we do not associate it with any sample of  $f(\theta)$ . We see from the figure that, except for the last two outliers whose values are about 1.5750, the eigenvalues are approximately samples of the symbol  $f(\theta)$  over a uniform grid in  $[0, \pi]$ . When increasing  $n$ , the first  $n - 1$  eigenvalues converge to the graph of  $f(\theta)$  (i.e., the pairs  $(\frac{j\pi}{n}, \lambda_j(\frac{1}{n} \mathbf{K}_n))$ ,  $j = 1, \dots, n - 1$ , converge to the pairs  $(\frac{j\pi}{n}, f(\frac{j\pi}{n}))$ ,  $j = 1, \dots, n - 1$ ), whereas the last two eigenvalues remain outliers (and their values remain approximately 1.5750). Figures 24 and 25 are obtained in the same way as Fig. 23. The results of Figs. 23–25 agree with the interpretation of the asymptotic eigenvalue distributions  $\{\frac{1}{n} \mathbf{K}_n\}_n \sim_{\lambda} f(\theta)$ ,  $\{n \mathbf{M}_n\}_n \sim_{\lambda} h(\theta)$ ,  $\{\frac{1}{n^2} \mathbf{L}_n\}_n \sim_{\lambda} e(\theta)$  given in Sect. 2.2.

Considering that almost all the eigenvalues of  $\frac{1}{n^2} \mathbf{L}_n$  (sorted in increasing order) are approximated by the uniform samples  $e(\frac{j\pi}{n})$ ,  $j = 1, \dots, n + 1$ , almost all the eigenvalues of  $\mathbf{L}_n$  (i.e., almost all the numerical eigenvalues  $\lambda_{j,n}$ ,  $j = 1, \dots, n + 1$ ) are approximated by  $n^2 e(\frac{j\pi}{n})$ ,  $j = 1, \dots, n + 1$ . Consequently, we have

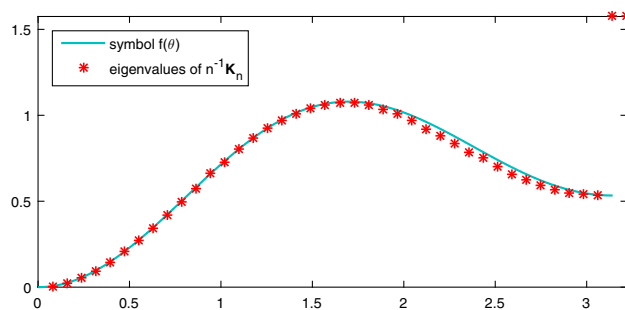


Fig. 23 Cubic  $C^2$  B-spline discretization: comparison between the symbol  $f(\theta)$  and the eigenvalues of  $\frac{1}{n} \mathbf{K}_n$  for  $n = 40$

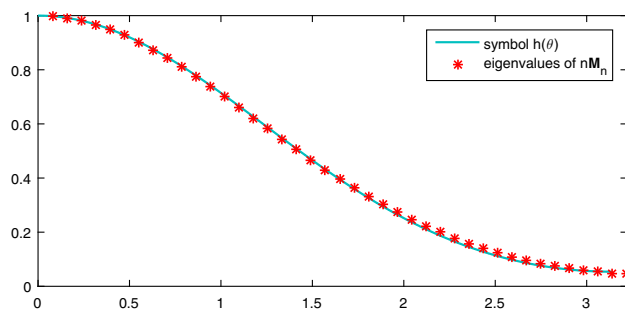


Fig. 24 Cubic  $C^2$  B-spline discretization: comparison between the symbol  $h(\theta)$  and the eigenvalues of  $n \mathbf{M}_n$  for  $n = 40$

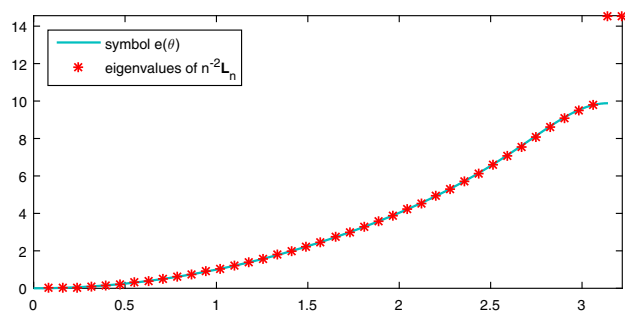


Fig. 25 Cubic  $C^2$  B-spline discretization: comparison between the symbol  $e(\theta)$  and the eigenvalues of  $\frac{1}{n^2} \mathbf{L}_n$  for  $n = 40$

$$\frac{\lambda_{j,n}}{\lambda_j} - 1 \approx \frac{e(\frac{j\pi}{n})}{(\frac{j\pi}{n})^2} - 1, \quad j = 1, \dots, n + 1.$$

It should be noted that the association of  $\lambda_{n+1,n}$  with  $n^2 e(\frac{(n+1)\pi}{n})$  is purely artificial, because the point  $\frac{(n+1)\pi}{n}$  lies outside the actual domain of  $e(\theta)$ . In Fig. 26 we plot the analytical predictions  $e(\frac{j\pi}{n})/(\frac{j\pi}{n})^2 - 1$  and the eigenvalue errors  $\lambda_{j,n}/\lambda_j - 1$  versus  $j/(n + 1)$ , for  $j = 1, \dots, n + 1$  and





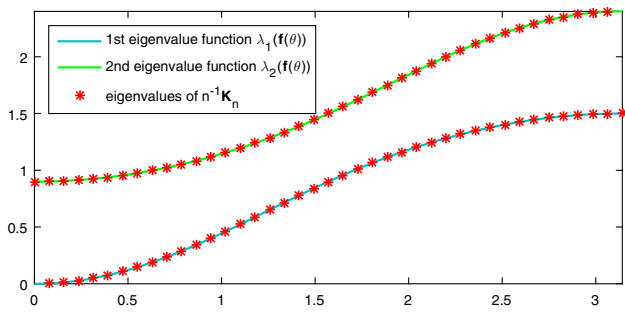


**Fig. 29** Cubic  $C^1$  B-spline discretization: comparison between the symbol  $\mathbf{f}(\theta)$  and the eigenvalues of  $\frac{1}{n}\mathbf{K}_n$  for  $n = 40$

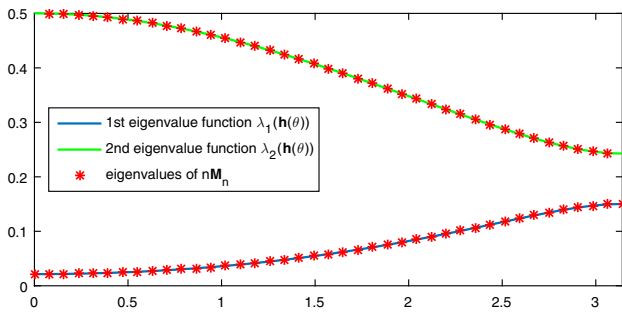


**Fig. 30** Cubic  $C^1$  B-spline discretization: comparison between the symbol  $\mathbf{h}(\theta)$  and the eigenvalues of  $n\mathbf{M}_n$  for  $n = 40$

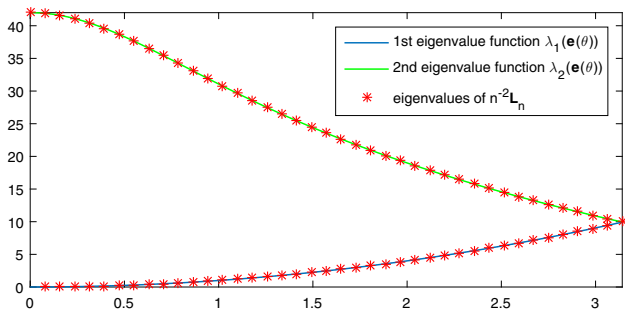


**Fig. 31** Cubic  $C^1$  B-spline discretization: comparison between the symbol  $\mathbf{e}(\theta)$  and the eigenvalues of  $\frac{1}{n^2}\mathbf{L}_n$  for  $n = 40$

spectrum of  $\frac{1}{n}\mathbf{K}_n$  corresponding to the two eigenvalue functions  $\lambda_1(\mathbf{f}(\theta))$  and  $\lambda_2(\mathbf{f}(\theta))$  are not separated, because  $\max_{\theta} \lambda_1(\mathbf{f}(\theta)) > \min_{\theta} \lambda_2(\mathbf{f}(\theta))$ .

Therefore, we observe a single branch instead of two branches in the spectrum of  $\frac{1}{n}\mathbf{K}_n$  when ordering the eigenvalues in ascending fashion. Figures 30 and 31 are the analogs of Fig. 29 for the cases of the symbols  $\mathbf{h}(\theta)$ ,  $\mathbf{e}(\theta)$  and the matrices  $n\mathbf{M}_n, \frac{1}{n^2}\mathbf{L}_n$ . Contrary to the case of  $\frac{1}{n}\mathbf{K}_n$ , the spectra of the matrices  $n\mathbf{M}_n$  and  $\frac{1}{n^2}\mathbf{L}_n$  show two branches, because

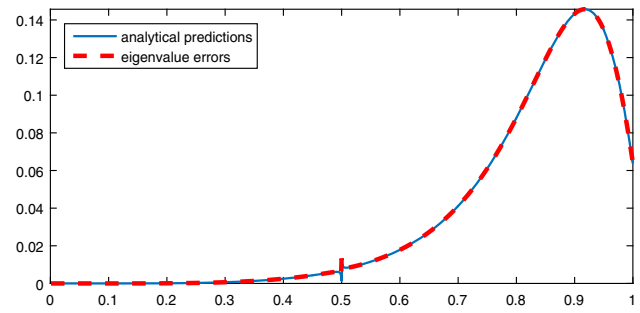


**Fig. 32** Cubic  $C^1$  B-spline discretization: analytical predictions  $w_j / (\frac{j\pi}{n})^2 - 1$  and eigenvalue errors  $\lambda_{j,n} / \lambda_j - 1$  versus  $j/N_n$ ,  $j = 1, \dots, N_n$  ( $N_n = 2n$ ,  $n = 500$ )

$$\begin{aligned} \max_{\theta} \lambda_1(\mathbf{h}(\theta)) &< \min_{\theta} \lambda_2(\mathbf{h}(\theta)), \\ \max_{\theta} \lambda_1(\mathbf{e}(\theta)) &< \min_{\theta} \lambda_2(\mathbf{e}(\theta)). \end{aligned}$$

Considering that the eigenvalues of  $\frac{1}{n^2}\mathbf{L}_n$  (sorted in increasing order) are approximated by the uniform samples  $\lambda_1(\mathbf{e}(\frac{j\pi}{n}))$ ,  $j = 1, \dots, n$ , and  $\lambda_2(\mathbf{e}(\frac{(2n-j)\pi}{n}))$ ,  $j = n + 1, \dots, 2n$ , the eigenvalues of  $\mathbf{L}_n$  (i.e., the numerical eigenvalues  $\lambda_{j,n}$ ,  $j = 1, \dots, 2n$ ) are approximated by the values  $n^2 \lambda_1(\mathbf{e}(\frac{j\pi}{n}))$ ,  $j = 1, \dots, n$ , and  $n^2 \lambda_2(\mathbf{e}(\frac{(2n-j)\pi}{n}))$ ,  $j = n + 1, \dots, 2n$ . Consequently, we have

$$\frac{\lambda_{j,n}}{\lambda_j} - 1 \approx \frac{w_j}{(\frac{j\pi}{n})^2} - 1, \quad j = 1, \dots, 2n,$$

where

$$w_j := \begin{cases} \lambda_1\left(\mathbf{e}\left(\frac{j\pi}{n}\right)\right), & j = 1, \dots, n, \\ \lambda_2\left(\mathbf{e}\left(\frac{(2n-j)\pi}{n}\right)\right), & j = n + 1, \dots, 2n. \end{cases}$$

In Fig. 32 we plot the analytical predictions  $w_j / (\frac{j\pi}{n})^2 - 1$  and the eigenvalue errors  $\lambda_{j,n} / \lambda_j - 1$  versus  $j/2n$ , for  $j = 1, \dots, 2n$  and  $n = 500$ . Clearly, there is a perfect match. Moreover, like in the case of quadratic  $C^0$  B-spline discretization, the two branches in the spectrum of  $\frac{1}{n^2}\mathbf{L}_n$  observed in Fig. 31 also produce in Fig. 32 two branches separated by the jump at  $j/N_n = 1/2$  ( $N_n = 2n$ ).

### 2.4.3 Cubic $C^0$ B-Spline Discretization

In the cubic  $C^0$  B-spline discretization on a uniform mesh with stepsize  $\frac{1}{n}$ , the basis functions  $\varphi_1, \dots, \varphi_{N_n}$  are chosen as the B-splines  $B_{2,[3,0]}, \dots, B_{3n,[3,0]}$ ; see Fig. 33. The basis functions are uniformly shifted-scaled versions of the fixed reference B-splines  $\phi_{1,[3,0]}, \phi_{2,[3,0]}, \phi_{3,[3,0]}$  in Fig. 34, which are the  $C^0$  B-splines of degree 3 defined on the knot sequence  $\{0, 0, 0, 1, 1, 1, 2\}$ . The resulting normalized stiffness and mass matrices are given by



**Fig. 33** Cubic  $C^0$  B-splines  $\{B_{1,[3,0]}, \dots, B_{3n+1,[3,0]}\}$  defined on the knot sequence  $\{0, 0, 0, 0, \frac{1}{n}, \frac{1}{n}, \frac{1}{n}, \frac{2}{n}, \frac{2}{n}, \frac{2}{n}, \dots, \frac{n-1}{n}, \frac{n-1}{n}, \frac{n-1}{n}, 1, 1, 1, 1\}$  for  $n = 10$

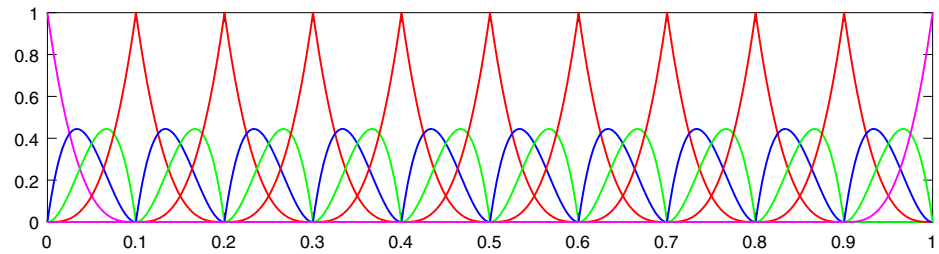
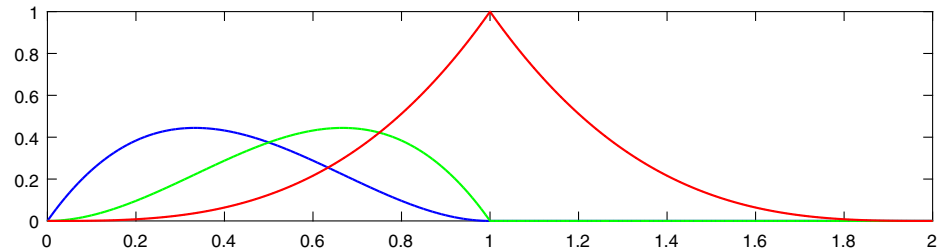


**Fig. 34** Reference cubic  $C^0$  B-splines  $\phi_{1,[3,0]}, \phi_{2,[3,0]}, \phi_{3,[3,0]}$  defined on the knot sequence  $\{0, 0, 0, 1, 1, 1, 2\}$



$$\{n\mathbf{M}_n\}_n \sim_{\text{GLT}} \mathbf{h}(\theta), \tag{2.32}$$

$$\left\{\frac{1}{n^2}\mathbf{L}_n\right\}_n \sim_{\text{GLT}} \mathbf{e}(\theta) := (\mathbf{h}(\theta))^{-1}\mathbf{f}(\theta), \tag{2.33}$$

i.e.,  $\mathbf{f}(\theta)$ ,  $\mathbf{h}(\theta)$ ,  $\mathbf{e}(\theta)$  are the symbols of  $\{\frac{1}{n}\mathbf{K}_n\}_n$ ,  $\{n\mathbf{M}_n\}_n$ ,  $\{\frac{1}{n^2}\mathbf{L}_n\}_n$ , respectively ( $\mathbf{L}_n := (\mathbf{M}_n)^{-1}\mathbf{K}_n$ ). The diagram used to compute these symbols is the same as in Fig. 16. As in the previous sections, (2.31)–(2.33) imply the singular value and eigenvalue distributions  $\{\frac{1}{n}\mathbf{K}_n\}_n \sim_{\sigma, \lambda} \mathbf{f}(\theta)$ ,  $\{n\mathbf{M}_n\}_n \sim_{\sigma, \lambda} \mathbf{h}(\theta)$ ,  $\{\frac{1}{n^2}\mathbf{L}_n\}_n \sim_{\sigma, \lambda} \mathbf{e}(\theta)$ .

The characteristic polynomials of  $\mathbf{f}(\theta)$ ,  $\mathbf{h}(\theta)$ ,  $\mathbf{e}(\theta)$  are

$$\begin{aligned} C_{\mathbf{f}(\theta)}(\lambda) &= \lambda^3 - \left(6 - \frac{3}{5}\cos\theta\right)\lambda^2 + \left(\frac{153}{20} - \frac{18}{5}\cos\theta\right)\lambda \\ &\quad - \frac{27}{10} + \frac{27}{10}\cos\theta, \\ C_{\mathbf{h}(\theta)}(\lambda) &= \lambda^3 - \left(\frac{16}{35} + \frac{1}{70}\cos\theta\right)\lambda^2 + \left(\frac{113}{2800} - \frac{1}{175}\cos\theta\right)\lambda \\ &\quad - \frac{3}{7000} - \frac{3}{28000}\cos\theta, \\ C_{\mathbf{e}(\theta)}(\lambda) &= \lambda^3 - \frac{540 - 30\cos\theta}{4 + \cos\theta}\lambda^2 + \frac{11520 + 1080\cos\theta}{4 + \cos\theta}\lambda \\ &\quad - \frac{25200 - 25200\cos\theta}{4 + \cos\theta}. \end{aligned}$$

By solving the characteristic equations  $C_{\mathbf{f}(\theta)}(\lambda) = 0$ ,  $C_{\mathbf{h}(\theta)}(\lambda) = 0$ ,  $C_{\mathbf{e}(\theta)}(\lambda) = 0$  with respect to  $\lambda$  (e.g., by using Cardano’s formula), one can find the (complicated!) analytical expressions of the eigenvalue functions  $\lambda_i(\mathbf{f}(\theta))$ ,  $\lambda_i(\mathbf{h}(\theta))$ ,  $\lambda_i(\mathbf{e}(\theta))$ ,  $i = 1, 2, 3$ . Figure 35 shows the graphs of the eigenvalue functions  $\lambda_1(\mathbf{f}(\theta))$ ,  $\lambda_2(\mathbf{f}(\theta))$ ,  $\lambda_3(\mathbf{f}(\theta))$

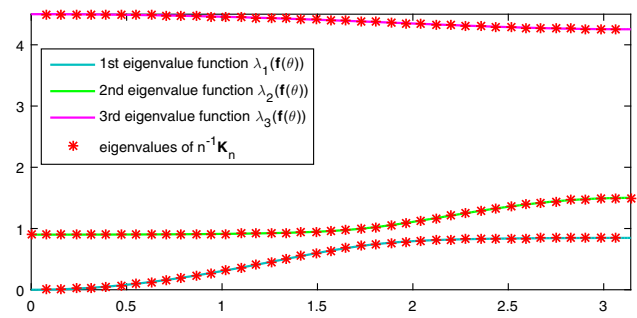


**Fig. 35** Cubic  $C^0$  B-spline discretization: comparison between the symbol  $\mathbf{f}(\theta)$  and the eigenvalues of  $\frac{1}{n}\mathbf{K}_n$  for  $n = 40$

over  $[0, \pi]$ , and the eigenvalues of  $\frac{1}{n}\mathbf{K}_n$  for  $n = 40$ . The eigenvalues  $\lambda_j(\frac{1}{n}\mathbf{K}_n)$ ,  $j = 1, \dots, 3n - 1$ , are represented by the red asterisks placed at the points  $(\frac{j\pi}{n}, \lambda_j(\frac{1}{n}\mathbf{K}_n))$ ,  $j = 1, \dots, n - 1$ ,  $(\frac{(j-n+1)\pi}{n}, \lambda_j(\frac{1}{n}\mathbf{K}_n))$ ,  $j = n, \dots, 2n$ , and  $(\frac{(j-2n)\pi}{n}, \lambda_j(\frac{1}{n}\mathbf{K}_n))$ ,  $j = 2n + 1, \dots, 3n - 1$ ; they are sorted so as to match the eigenvalue functions of the symbol  $\mathbf{f}(\theta)$ . We see from the figure that the eigenvalues are perfectly approximated by the samples of the eigenvalue functions of the symbol  $\mathbf{f}(\theta)$  over a uniform grid in  $[0, \pi]$ . This agrees with the interpretation of the asymptotic eigenvalue distribution  $\{\frac{1}{n}\mathbf{K}_n\}_n \sim_{\lambda} \mathbf{f}(\theta)$  given in Sect. 2.3.2. Figures 36 and 37 are the analogs of Fig. 35 for the cases of the symbols  $\mathbf{h}(\theta)$ ,  $\mathbf{e}(\theta)$  and the matrices  $n\mathbf{M}_n$ ,  $\frac{1}{n^2}\mathbf{L}_n$ .

Considering that the eigenvalues of  $\frac{1}{n^2}\mathbf{L}_n$  (sorted in increasing order) are approximated by the uniform samples  $\lambda_1(\mathbf{e}(\frac{j\pi}{n}))$ ,  $j = 1, \dots, n - 1$ ,  $\lambda_2(\mathbf{e}(\frac{(2n-j)\pi}{n}))$ ,  $j = n, \dots, 2n$ , and

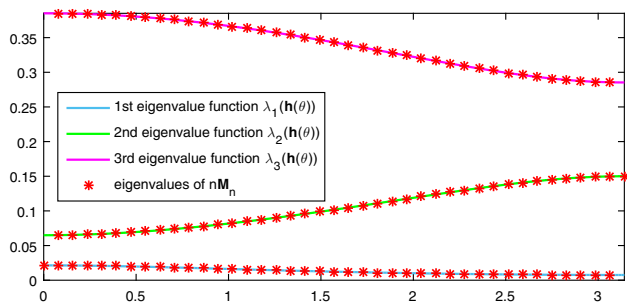


**Fig. 36** Cubic  $C^0$  B-spline discretization: comparison between the symbol  $\mathbf{h}(\theta)$  and the eigenvalues of  $n\mathbf{M}_n$  for  $n = 40$

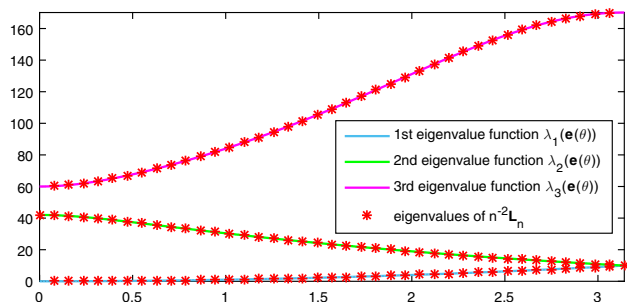


**Fig. 37** Cubic  $C^0$  B-spline discretization: comparison between the symbol  $\mathbf{e}(\theta)$  and the eigenvalues of  $\frac{1}{n^2}\mathbf{L}_n$  for  $n = 40$

$\lambda_3(\mathbf{e}(\frac{j-2n}{n}\pi)), j = 2n + 1, \dots, 3n - 1$ , the eigenvalues of  $\mathbf{L}_n$  (i.e., the numerical eigenvalues  $\lambda_{j,n}, j = 1, \dots, 3n - 1$ ) are approximated by the values  $n^2\lambda_1(\mathbf{e}(\frac{j\pi}{n})), j = 1, \dots, n - 1, n^2\lambda_2(\mathbf{e}(\frac{(2n-j)\pi}{n})), j = n, \dots, 2n,$  and  $n^2\lambda_3(\mathbf{e}(\frac{(j-2n)\pi}{n})), j = 2n + 1, \dots, 3n - 1$ . Consequently, we have

$$\frac{\lambda_{j,n}}{\lambda_j} - 1 \approx \frac{w_j}{(\frac{j\pi}{n})^2} - 1, \quad j = 1, \dots, 3n - 1,$$

where

$$w_j := \begin{cases} \lambda_1\left(\mathbf{e}\left(\frac{j\pi}{n}\right)\right), & j = 1, \dots, n - 1, \\ \lambda_2\left(\mathbf{e}\left(\frac{(2n-j)\pi}{n}\right)\right), & j = n, \dots, 2n, \\ \lambda_3\left(\mathbf{e}\left(\frac{(j-2n)\pi}{n}\right)\right), & j = 2n + 1, \dots, 3n - 1. \end{cases}$$

In Fig. 38 we plot the analytical predictions  $w_j/(\frac{j\pi}{n})^2 - 1$  and the eigenvalue errors  $\lambda_{j,n}/\lambda_j - 1$  versus  $j/(3n - 1)$ , for  $j = 1, \dots, 3n - 1$  and  $n = 500$ . Clearly, there is a perfect match. Note that the three branches in the spectrum of  $\frac{1}{n^2}\mathbf{L}_n$ , which are visible in Fig. 37, also produce in Fig. 38 three branches separated by the jumps at  $j/N_n \approx 1/3$  and  $j/N_n \approx 2/3$  ( $N_n = 3n - 1$ ). Actually, the jump at  $j/N_n \approx 1/3$  is hardly visible, and this is due to the fact that  $\max_\theta \lambda_1(\mathbf{e}(\theta)) \approx \min_\theta \lambda_2(\mathbf{e}(\theta))$ ; see Fig. 37.

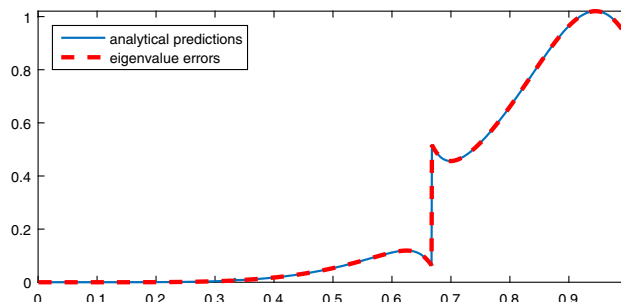


**Fig. 38** Cubic  $C^0$  B-spline discretization: analytical predictions  $w_j/(\frac{j\pi}{n})^2 - 1$  and eigenvalue errors  $\lambda_{j,n}/\lambda_j - 1$  versus  $j/N_n, j = 1, \dots, N_n$  ( $N_n = 3n - 1, n = 500$ )

### 2.5 $p$ -Degree $C^k$ B-Spline Discretization

It is now time to generalize what we have seen in Sects. 2.2–2.4. Consider the general Galerkin  $p$ -degree  $C^k$  B-spline discretization of the Laplacian eigenvalue problem (2.1) on a uniform mesh with stepsize  $\frac{1}{n}$ . That is the Galerkin discretization described at the beginning of Sect. 2, where the basis functions  $\{\varphi_1, \dots, \varphi_{N_n}\}$  are taken as  $\{B_{2,[p,k]}, \dots, B_{n(p-k)+k,[p,k]}\}$  defined in (2.7). The resulting stiffness and mass matrices are given by (2.4)–(2.5) with

$$\varphi_i := B_{i+1,[p,k]}, \quad i = 1, \dots, n(p - k) + k - 1,$$

i.e.,

$$\mathbf{K}_n := \left[ \int_0^1 B'_{j+1,[p,k]}(x) B'_{i+1,[p,k]}(x) dx \right]_{i,j=1}^{n(p-k)+k-1},$$

$$\mathbf{M}_n := \left[ \int_0^1 B_{j+1,[p,k]}(x) B_{i+1,[p,k]}(x) dx \right]_{i,j=1}^{n(p-k)+k-1}.$$

All the B-spline basis functions, except for the first  $k$  and the last  $k$ , are uniformly shifted-scaled versions of  $p - k$  fixed reference functions  $\phi_{1,[p,k]}, \dots, \phi_{p-k,[p,k]}$ , which are simply the first  $p - k$  B-splines defined on the reference knot sequence

$$\underbrace{0, \dots, 0}_{p-k}, \underbrace{1, \dots, 1}_{p-k}, \underbrace{\eta, \dots, \eta}_{p-k}, \quad \eta := \left\lfloor \frac{p+1}{p-k} \right\rfloor. \quad (2.34)$$

In formulas, we have

$$B_{k+1+(p-k)(i-1)+j,[p,k]}(x) = \phi_{j,[p,k]}(nx - i + 1),$$

$$i = 1, \dots, n - v, \quad j = 1, \dots, p - k, \quad (2.35)$$

where

$$v := \left\lfloor \frac{k+1}{p-k} \right\rfloor.$$

Let

$$\mathbf{K}_{[p,k]}^{[\ell]} := \left[ \int_{\mathbb{R}} \phi'_{j,[p,k]}(x) \phi'_{i,[p,k]}(x - \ell) dx \right]_{i,j=1}^{p-k}, \quad \ell = 0, 1, 2, \dots \tag{2.36}$$

$$\mathbf{M}_{[p,k]}^{[\ell]} := \left[ \int_{\mathbb{R}} \phi_{j,[p,k]}(x) \phi_{i,[p,k]}(x - \ell) dx \right]_{i,j=1}^{p-k}, \quad \ell = 0, 1, 2, \dots \tag{2.37}$$

Note that the integrals over  $\mathbb{R}$  appearing in (2.36)–(2.37) actually reduce to integrals over  $[0, \eta]$ , because the supports of the reference B-splines satisfy

$$\text{supp}(\phi_{1,[p,k]}) \subseteq \text{supp}(\phi_{2,[p,k]}) \subseteq \dots \subseteq \text{supp}(\phi_{p-k,[p,k]}) = [0, \eta].$$

For the same reason, the blocks (2.36)–(2.37) corresponding to indices  $\ell \geq \eta$  reduce to the zero block:

$$\mathbf{K}_{[p,k]}^{[\ell]} = \mathbf{M}_{[p,k]}^{[\ell]} = \mathbf{0}, \quad \ell \geq \eta.$$

Define the  $(p - k) \times (p - k)$  matrix-valued functions  $\mathbf{f}_{[p,k]}, \mathbf{h}_{[p,k]}, \mathbf{e}_{[p,k]} : [-\pi, \pi] \rightarrow \mathbb{C}^{(p-k) \times (p-k)}$  by

$$\mathbf{f}_{[p,k]}(\theta) := \mathbf{K}_{[p,k]}^{[0]} + \sum_{\ell=1}^{\eta-1} \left( \mathbf{K}_{[p,k]}^{[\ell]} e^{i\ell\theta} + \left( \mathbf{K}_{[p,k]}^{[\ell]} \right)^T e^{-i\ell\theta} \right), \tag{2.38}$$

$$\mathbf{h}_{[p,k]}(\theta) := \mathbf{M}_{[p,k]}^{[0]} + \sum_{\ell=1}^{\eta-1} \left( \mathbf{M}_{[p,k]}^{[\ell]} e^{i\ell\theta} + \left( \mathbf{M}_{[p,k]}^{[\ell]} \right)^T e^{-i\ell\theta} \right), \tag{2.39}$$

$$\mathbf{e}_{[p,k]}(\theta) := \left( \mathbf{h}_{[p,k]}(\theta) \right)^{-1} \mathbf{f}_{[p,k]}(\theta). \tag{2.40}$$

Due to the specific structure (2.35) of the basis functions, the normalized stiffness matrix  $\frac{1}{n} \mathbf{K}_n$  (resp., mass matrix  $n \mathbf{M}_n$ ) contains as a principal submatrix the Toeplitz matrix  $\mathbf{T}_{n-v}(\mathbf{f}_{[p,k]})$  (resp.,  $\mathbf{T}_{n-v}(\mathbf{h}_{[p,k]})$ ). Moreover, the generic central block row of  $\frac{1}{n} \mathbf{K}_n$  is

$$[\dots \mathbf{0} \ \mathbf{0} \ \mathbf{K}_{[p,k]}^{[\eta-1]} \ \dots \ \mathbf{K}_{[p,k]}^{[1]} \ \mathbf{K}_{[p,k]}^{[0]} \ \left( \mathbf{K}_{[p,k]}^{[1]} \right)^T \ \dots \ \left( \mathbf{K}_{[p,k]}^{[\eta-1]} \right)^T \ \mathbf{0} \ \mathbf{0} \ \dots],$$

just like the generic central block row of  $\mathbf{T}_{n-v}(\mathbf{f}_{[p,k]})$  with only some additional zeros to reach the length  $n(p - k) + k - 1$ ; and the generic central block row of  $n \mathbf{M}_n$  is

$$[\dots \mathbf{0} \ \mathbf{0} \ \mathbf{M}_{[p,k]}^{[\eta-1]} \ \dots \ \mathbf{M}_{[p,k]}^{[1]} \ \mathbf{M}_{[p,k]}^{[0]} \ \left( \mathbf{M}_{[p,k]}^{[1]} \right)^T \ \dots \ \left( \mathbf{M}_{[p,k]}^{[\eta-1]} \right)^T \ \mathbf{0} \ \mathbf{0} \ \dots],$$

just like the generic central block row of  $\mathbf{T}_{n-v}(\mathbf{h}_{[p,k]})$  with only some additional zeros to reach the length  $n(p - k) + k - 1$ .

The proof of all these results is not difficult, but it is omitted because it is full of technicalities. Since  $\{\mathbf{T}_{n-v}(\mathbf{f}_{[p,k]})\}_n \sim_{\text{GLT}} \mathbf{f}_{[p,k]}(\theta)$  and  $\{\mathbf{T}_{n-v}(\mathbf{h}_{[p,k]})\}_n \sim_{\text{GLT}} \mathbf{h}_{[p,k]}(\theta)$ , the theory of GLT sequences yields

$$\left\{ \frac{1}{n} \mathbf{K}_n \right\}_n \sim_{\text{GLT}} \mathbf{f}_{[p,k]}(\theta), \tag{2.41}$$

$$\left\{ n \mathbf{M}_n \right\}_n \sim_{\text{GLT}} \mathbf{h}_{[p,k]}(\theta), \tag{2.42}$$

$$\left\{ \frac{1}{n^2} \mathbf{L}_n \right\}_n \sim_{\text{GLT}} \mathbf{e}_{[p,k]}(\theta), \tag{2.43}$$

i.e.,  $\mathbf{f}_{[p,k]}(\theta), \mathbf{h}_{[p,k]}(\theta), \mathbf{e}_{[p,k]}(\theta)$  are the symbols of  $\left\{ \frac{1}{n} \mathbf{K}_n \right\}_n, \left\{ n \mathbf{M}_n \right\}_n, \left\{ \frac{1}{n^2} \mathbf{L}_n \right\}_n$ , respectively ( $\mathbf{L}_n := (\mathbf{M}_n)^{-1} \mathbf{K}_n$ ). The procedure used to obtain these symbols is conceptually the same as in Fig. 16. Note that Fig. 3 is just a special case of Fig. 16, corresponding to the situation in which the blocks of the matrices are  $1 \times 1$ , i.e., scalars. This happens only in the case of maximal smoothness  $k = p - 1$ . As a consequence of (2.41)–(2.43), we get

$$\left\{ \frac{1}{n} \mathbf{K}_n \right\}_n \sim_{\sigma, \lambda} \mathbf{f}_{[p,k]}(\theta), \tag{2.44}$$

$$\left\{ n \mathbf{M}_n \right\}_n \sim_{\sigma, \lambda} \mathbf{h}_{[p,k]}(\theta), \tag{2.45}$$

$$\left\{ \frac{1}{n^2} \mathbf{L}_n \right\}_n \sim_{\sigma, \lambda} \mathbf{e}_{[p,k]}(\theta). \tag{2.46}$$

The singular value distributions in (2.44)–(2.46) are direct consequences of (2.41)–(2.43), as well as the eigenvalue distributions in (2.44)–(2.45) (because the matrices  $\mathbf{K}_n$  and  $\mathbf{M}_n$  are symmetric). The eigenvalue distribution in (2.46) follows from a symmetrization argument applied to the matrix  $\mathbf{L}_n$ .

**Remark 2.1** (Properties of the symbols) We collect here some of the main properties of the functions  $\mathbf{f}_{[p,k]}(\theta), \mathbf{h}_{[p,k]}(\theta), \mathbf{e}_{[p,k]}(\theta)$ . All of them have already been observed in the specific examples considered in Sects. 2.2–2.4. To keep the presentation as simple as possible, the corresponding proofs are omitted. We also state an important property that has been conjectured on the basis of numerical experiments.

- $\mathbf{f}_{[p,k]}(\theta)$  is Hermitian positive semidefinite for every  $\theta \in [-\pi, \pi]$ .
- $\mathbf{h}_{[p,k]}(\theta)$  is Hermitian positive definite for every  $\theta \in [-\pi, \pi]$ .
- The eigenvalue functions  $\lambda_i(\mathbf{f}_{[p,k]}(\theta)), \lambda_i(\mathbf{e}_{[p,k]}(\theta)), i = 1, \dots, p - k$ , are real and non-negative on  $[-\pi, \pi]$ . Moreover, they are symmetric around  $\theta = 0$ , i.e., they are even functions.

- The eigenvalue functions  $\lambda_i(\mathbf{h}_{[p,k]}(\theta)), i = 1, \dots, p - k$ , are real and positive on  $[-\pi, \pi]$ . Moreover, they are symmetric around  $\theta = 0$ .
- [Conjecture]  $\mathbf{f}_{[p,k]}(\theta)$  is Hermitian positive definite for  $\theta \in [-\pi, \pi] \setminus \{0\}$  and singular (with a unique eigenvalue equal to 0) for  $\theta = 0$ . Consequently, the eigenvalue functions  $\lambda_i(\mathbf{f}_{[p,k]}(\theta)), \lambda_i(\mathbf{e}_{[p,k]}(\theta)), i = 1, \dots, p - k$ , are positive on  $[-\pi, \pi]$ , except for the minimal eigenvalue functions  $\lambda_1(\mathbf{f}_{[p,k]}(\theta)), \lambda_1(\mathbf{e}_{[p,k]}(\theta))$ , which are positive on  $[-\pi, \pi] \setminus \{0\}$  but vanish at  $\theta = 0$ .

We point out that the above conjecture was proved in [10] for  $k = p - 1$ . For  $k = 0$  it was proved in [16] in the case where the  $p$ -degree  $C^0$  B-spline basis is replaced by the  $p$ -degree  $C^0$  Lagrangian basis.

**Remark 2.2** (Analytical predictions of the eigenvalue errors) Let  $\lambda_{j,n}, j = 1, \dots, n(p - k) + k - 1$ , be the numerical eigenvalues (i.e., the eigenvalues of  $\mathbf{L}_n$ ) sorted, as always, in increasing order. In view of the eigenvalue distribution  $\{\frac{1}{n^2} \mathbf{L}_n\}_n \sim \lambda \mathbf{e}_{[p,k]}(\theta)$  and the fact that the eigenvalue functions  $\lambda_1(\mathbf{e}_{[p,k]}(\theta)), \dots, \lambda_{p-k}(\mathbf{e}_{[p,k]}(\theta))$  are symmetric around  $\theta = 0$  (see Remark 2.1), we can say that:

- for large values of  $n$ , the eigenvalues of  $\frac{1}{n^2} \mathbf{L}_n$  (except possibly for a small number of outliers) are approximated by uniform samples over  $[0, \pi]$  of the eigenvalue functions  $\lambda_i(\mathbf{e}_{[p,k]}(\theta)), i = 1, \dots, p - k$ ;
- for large values of  $n$ , the eigenvalues of  $\mathbf{L}_n$  (except possibly for a small number of outliers) are approximated by uniform samples over  $[0, \pi]$  of the scaled eigenvalue functions  $n^2 \lambda_i(\mathbf{e}_{[p,k]}(\theta)), i = 1, \dots, p - k$ .

Therefore, also in view of the experience we have gained from Sects. 2.2–2.4, we propose the following procedure to compute the (asymptotic) analytical predictions of the eigenvalue errors

$$\frac{\lambda_{j,n}}{\lambda_j} - 1, \quad j = 1, \dots, n(p - k) + k - 1,$$

in the limit of mesh refinement (when  $n \rightarrow \infty$ ).

- Compute the uniform samples

$$\lambda_i\left(\mathbf{e}_{[p,k]}\left(\frac{j\pi}{n}\right)\right), \quad j = 1, \dots, n, \quad i = 1, \dots, p - k, \tag{2.47}$$

sort them in increasing order, and put them in a vector  $\mathbf{y} := (y_1, \dots, y_{n(p-k)})$ .

- Compute the (asymptotic) analytical predictions of the eigenvalue errors as follows:

$$\frac{\lambda_{j,n}}{\lambda_j} - 1 \approx \frac{n^2 y_j}{\lambda_j} - 1 = \frac{y_j}{\left(\frac{j\pi}{n}\right)^2} - 1, \quad j = 1, \dots, m, \tag{2.48}$$

where  $m := \min(n(p - k), n(p - k) + k - 1)$ .

Let  $h := \frac{1}{n}$  be the mesh stepsize and set  $\omega := \lambda^{1/2}$ . Then, following a canonical notation appearing, e.g., in the appendix of [20], the above sampling procedure, and especially (2.48), can be formally condensed into the formula

$$\frac{\lambda_{1,2,\dots,p-k}^h - \lambda}{\lambda} = \frac{\lambda_{1,2,\dots,p-k}(\mathbf{e}_{[p,k]}(\omega h))}{(\omega h)^2} - 1. \tag{2.49}$$

Note that in general the number of components of  $\lambda := (\lambda_{1,n}, \dots, \lambda_{n(p-k)+k-1,n})$  is different from the number of components of  $\mathbf{y} := (y_1, \dots, y_{n(p-k)})$ . In (2.48) we are assuming that, when  $\lambda$  is longer than  $\mathbf{y}$ , the eigenvalue errors corresponding to indices  $j$  exceeding the length of  $\mathbf{y}$  have no analytical counterpart. Actually, the number of these “excluded” eigenvalue errors is only  $\max(0, k - 1) \leq p - 2$ . Moreover, in the limit of mesh refinement  $n \rightarrow \infty$  we have  $n(p - k) + k - 1 = n(p - k)$ , which means that asymptotically there is no difference between the length of  $\lambda$  and  $\mathbf{y}$  (recall that (2.48) holds precisely in the limit of mesh refinement). We also note that the sampling procedure we followed in Sects. 2.2–2.4 is more precise than the sampling procedure described here. Indeed, in Sects. 2.2–2.4 we added to (2.47) the samples  $\lambda_i(\mathbf{e}_{[p,k]}(0))$  for  $i = 2, \dots, p - k$ , thus obtaining a vector  $\hat{\mathbf{y}}$  longer than  $\mathbf{y}$ , we extracted from  $\hat{\mathbf{y}}$  the subvector  $\mathbf{w}$  consisting of the components of  $\hat{\mathbf{y}}$  that better matched the components of  $\lambda$ , and we used in (2.48) the components of  $\mathbf{w}$  instead of the components of  $\mathbf{y}$ . One could therefore decide to adopt this more precise sampling procedure rather than the one described above. Nevertheless, again in the limit of mesh refinement  $n \rightarrow \infty$ , i.e., for large values of  $n$ , the sampling procedure described here is indistinguishable from the sampling procedure we followed in Sects. 2.2–2.4. In addition, the sampling procedure described here is simpler as it does not require the a priori knowledge of the vector  $\lambda$ .

**Remark 2.3** (Spectral branches) The symbols  $\mathbf{f}_{[p,k]}(\theta), \mathbf{h}_{[p,k]}(\theta), \mathbf{e}_{[p,k]}(\theta)$  are  $(p - k) \times (p - k)$  matrix-valued functions. Note that  $p - k$  is the number of reference functions  $\phi_{1,[p,k]}, \dots, \phi_{p-k,[p,k]}$ . In view of the relations (2.44)–(2.46), we have at most  $p - k$  branches in the spectrum of  $\frac{1}{n} \mathbf{K}_n$  (resp.,  $n \mathbf{M}_n, \frac{1}{n^2} \mathbf{L}_n$ ), i.e., one branch for each of the  $p - k$  eigenvalue functions of  $\mathbf{f}_{[p,k]}(\theta)$  (resp.,  $\mathbf{h}_{[p,k]}(\theta), \mathbf{e}_{[p,k]}(\theta)$ ). As testified by Fig. 29, however, the number of branches

may also be less than  $p - k$ . In general, the spectrum of  $\frac{1}{n}\mathbf{K}_n$  is composed of  $\beta + 1$  branches, where  $\beta$  is the number of indices  $i \in \{1, \dots, p - k - 1\}$  such that

$$\max_{\theta} \lambda_i(\mathbf{f}_{[p,k]}(\theta)) < \min_{\theta} \lambda_{i+1}(\mathbf{f}_{[p,k]}(\theta)).$$

The same consideration applies to the matrices  $n\mathbf{M}_n$  and  $\frac{1}{n^2}\mathbf{L}_n$ . Concerning the symbol  $\mathbf{e}_{[p,k]}(\theta)$ , based on numerical experiments we conjecture that

$$\begin{aligned} \max_{\theta} \lambda_i(\mathbf{e}_{[p,k]}(\theta)) < \min_{\theta} \lambda_{i+1}(\mathbf{e}_{[p,k]}(\theta)), \\ i = 1, \dots, p - k - 1, \end{aligned}$$

for every degree  $p \geq 1$  and every smoothness  $0 \leq k \leq p - 1$ , which means that the spectrum of  $\frac{1}{n^2}\mathbf{L}_n$  (and hence also the spectrum of  $\mathbf{L}_n$  consisting of the numerical eigenvalues  $\lambda_{j,n}$ ) is formed by  $p - k$  branches. The eigenvalue errors (as plotted in Figs. 7, 13, 20, 26, 32, 38) consist of  $p - k$  branches separated by the jumps at  $j/N_n \approx i/(p - k)$ ,  $i = 1, \dots, p - k - 1$ , where  $N_n$  is the total number of degrees of freedom (the size of  $\mathbf{L}_n$ ). Of these  $p - k$  branches, only the first one is “compressed” around the level 0, whereas the other  $p - k - 1$  branches are far away from 0. This means that only the smallest numerical eigenvalues  $\lambda_{j,n}$  (those corresponding to the first eigenvalue function  $\lambda_1(\mathbf{e}_{[p,k]}(\theta))$ ) are good approximations of the corresponding Laplacian eigenvalues  $\lambda_j$ ; their number is about  $N_n/(p - k)$ . The other  $N_n - N_n/(p - k)$  numerical eigenvalues (those corresponding to the eigenvalue functions  $\lambda_i(\mathbf{e}_{[p,k]}(\theta))$  for  $i > 1$ ) are spurious; they have little to do with the corresponding Laplacian eigenvalues. According to the engineering terminology (see, e.g., the appendix of [20]), the first branch is referred to as the “acoustical branch”, whereas the other (spurious) branches are referred to as the “optical branches” (a name which intentionally brings to mind the phenomenon of optical illusion).

It is worth noting that the results obtained in this section allow us to create a very simple algorithm for the computation of the symbols (2.38)–(2.40).

**Algorithm 2.1** (Computation of the symbols) Given the degree  $p$  and the smoothness  $k$ ,

- compute the blocks  $\mathbf{K}_{[p,k]}^{[\ell]}$ ,  $\mathbf{M}_{[p,k]}^{[\ell]}$  in (2.36)–(2.37) for  $\ell = 0, \dots, \eta - 1$  with  $\eta := \lceil \frac{p+1}{p-k} \rceil$ ;
- compute  $\mathbf{f}_{[p,k]}(\theta)$ ,  $\mathbf{h}_{[p,k]}(\theta)$ ,  $\mathbf{e}_{[p,k]}(\theta)$  using (2.38)–(2.40).

Algorithm 2.1 is particularly suited for implementation in symbolic computing environments such as MAPLE or MATHEMATICA, and it is not difficult to derive from it a MATLAB version as well. In a symbolic environment, the integrals in (2.36)–(2.37) are computed exactly so as to

obtain the exact expressions of the blocks  $\mathbf{K}_{[p,k]}^{[\ell]}$ ,  $\mathbf{M}_{[p,k]}^{[\ell]}$  for  $\ell = 0, \dots, \eta - 1$ .<sup>1</sup> In addition, the evaluation point  $\theta$  is defined as a symbolic variable, so as to obtain from (2.38)–(2.40) the exact expressions of  $\mathbf{f}_{[p,k]}(\theta)$ ,  $\mathbf{h}_{[p,k]}(\theta)$ ,  $\mathbf{e}_{[p,k]}(\theta)$ . Once these expressions have been obtained, they can be used to compute the characteristic polynomials  $C_{\mathbf{f}_{[p,k]}(\theta)}(\lambda)$ ,  $C_{\mathbf{h}_{[p,k]}(\theta)}(\lambda)$ ,  $C_{\mathbf{e}_{[p,k]}(\theta)}(\lambda)$ , to evaluate the eigenvalue functions  $\lambda_i(\mathbf{f}_{[p,k]}(\theta))$ ,  $\lambda_i(\mathbf{h}_{[p,k]}(\theta))$ ,  $\lambda_i(\mathbf{e}_{[p,k]}(\theta))$ ,  $i = 1, \dots, p - k$ , and to determine the analytical predictions of the eigenvalue errors as explained in Remark 2.2.

In what follows we focus on some specific cases. In particular, we study the case of maximal smoothness  $C^{p-1}$  and the case of minimal smoothness  $C^0$ . The maximal smoothness is representative of IgA [4, 19], whereas the minimal smoothness is typical of classical FEA [18]. We also consider in some detail the case of smoothness  $C^{p-2}$ , in which the symbols  $\mathbf{f}_{[p,p-2]}(\theta)$ ,  $\mathbf{h}_{[p,p-2]}(\theta)$ ,  $\mathbf{e}_{[p,p-2]}(\theta)$  are  $2 \times 2$  matrix-valued functions and, therefore, some analytical computations are possible (especially, the computation of the eigenvalue functions  $\lambda_i(\mathbf{f}_{[p,p-2]}(\theta))$ ,  $\lambda_i(\mathbf{h}_{[p,p-2]}(\theta))$ ,  $\lambda_i(\mathbf{e}_{[p,p-2]}(\theta))$ ,  $i = 1, 2$ , and, consequently, the determination of the analytical predictions of the eigenvalue errors; see Remark 2.2).

### 2.5.1 $p$ -Degree $C^{p-1}$ B-Spline Discretization

Let  $\phi_{[p]}$  be the B-spline of degree  $p$  corresponding to the knot sequence  $\{0, 1, \dots, p + 1\}$ . Following a classical terminology [2], we refer to  $\phi_{[p]}$  as the cardinal B-spline of degree  $p$ . When assuming the maximal smoothness  $k = p - 1$ , there is a unique reference function  $\phi_{[p,p-1]}$ , which coincides with the cardinal B-spline of degree  $p$ ,

$$\phi_{[p,p-1]} := \phi_{[p]}.$$

The resulting symbols in (2.38)–(2.40) are scalar functions and will be denoted by  $f_p$ ,  $h_p$ ,  $e_p$ , i.e.,

$$f_p := \mathbf{f}_{[p,p-1]}, \quad h_p := \mathbf{h}_{[p,p-1]}, \quad e_p := \mathbf{e}_{[p,p-1]}.$$

Looking at the expressions (2.36)–(2.37), we see that  $\mathbf{K}_{[p,p-1]}^{[\ell]}$  and  $\mathbf{M}_{[p,p-1]}^{[\ell]}$  are two real numbers given by

$$\begin{aligned} \mathbf{K}_{[p,p-1]}^{[\ell]} &:= \int_{\mathbb{R}} \phi'_{[p]}(x) \phi'_{[p]}(x - \ell) dx = -\phi''_{[2p+1]}(p + 1 - \ell), \\ &\ell = 0, 1, 2, \dots \end{aligned} \tag{2.50}$$

<sup>1</sup> This is not computationally expensive as the integrands are piecewise polynomials and the number of integrals to be computed is at most  $2\eta(p - k)^2$ . The latter number can be further reduced by exploiting the specific properties of the B-spline reference functions  $\phi_{1,[p,k]}, \dots, \phi_{p-k,[p,k]}$ .

$$\mathbf{M}_{[p,p-1]}^{[\ell]} := \int_{\mathbb{R}} \phi_{[p]}(x)\phi_{[p]}(x-\ell)dx = \phi_{[2p+1]}(p+1-\ell),$$

$$\ell = 0, 1, 2, \dots \tag{2.51}$$

The last equalities in (2.50)–(2.51) are due to a particular feature of cardinal B-splines [10, 22]: the inner product (of derivatives) of two shifted cardinal B-splines can be interpreted as an evaluation (of a higher-order derivative) of a higher-degree cardinal B-spline. In view of (2.50)–(2.51), the symbols  $f_p, h_p, e_p$  can be expressed as follows:

$$f_p(\theta) = -\phi_{[2p+1]}(p+1) - 2 \sum_{\ell=1}^p \phi_{[2p+1]}(p+1-\ell) \cos(\ell\theta)$$

$$= (2 - 2 \cos \theta)h_{p-1}(\theta), \tag{2.52}$$

$$h_p(\theta) = \phi_{[2p+1]}(p+1) + 2 \sum_{\ell=1}^p \phi_{[2p+1]}(p+1-\ell) \cos(\ell\theta), \tag{2.53}$$

$$e_p(\theta) = \frac{f_p(\theta)}{h_p(\theta)} = \frac{(2 - 2 \cos \theta)h_{p-1}(\theta)}{h_p(\theta)}$$

$$= \frac{(2 - 2 \cos \theta)(\phi_{[2p-1]}(p) + 2 \sum_{\ell=1}^{p-1} \phi_{[2p-1]}(p-\ell) \cos(\ell\theta))}{\phi_{[2p+1]}(p+1) + 2 \sum_{\ell=1}^p \phi_{[2p+1]}(p+1-\ell) \cos(\ell\theta)}, \tag{2.54}$$

where the second identity in (2.52) was proved in [10]. Figure 39 shows the graph of  $e_p(\theta)$  over  $[0, \pi]$  for  $p = 1, \dots, 6$  and the graph of the function  $\theta^2$ , which is denoted by  $e_\infty(\theta)$  because  $e_p(\theta)$  converges to  $\theta^2$  as  $p \rightarrow \infty$  [7]. Since  $e_p(\theta)$  is increasing over  $[0, \pi]$  for all  $p \geq 1$  [7], the analytical predictions of the eigenvalue errors can be expressed according to Remark 2.2 as follows:

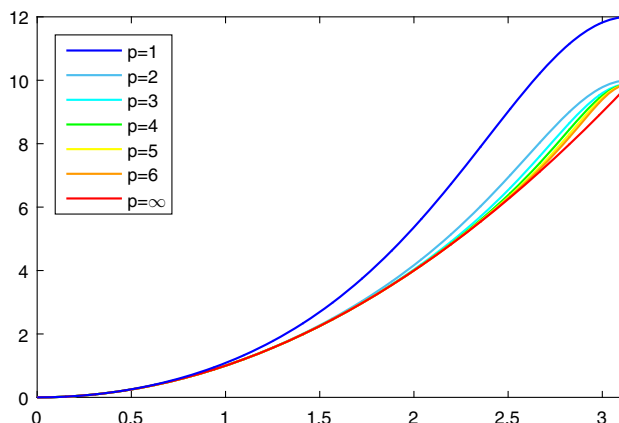


Fig. 39 Graphs of the symbol  $e_p(\theta)$  for  $p = 1, \dots, 6$  and the function  $\theta^2 = e_\infty(\theta)$

$$\frac{\lambda_{j,n}}{\lambda_j} - 1 \approx \frac{e_p(\frac{j\pi}{n})}{(\frac{j\pi}{n})^2} - 1$$

$$= \frac{(2 - 2 \cos \frac{j\pi}{n})(\phi_{[2p-1]}(p) + 2 \sum_{\ell=1}^{p-1} \phi_{[2p-1]}(p-\ell) \cos(\frac{\ell j\pi}{n}))}{(\frac{j\pi}{n})^2 (\phi_{[2p+1]}(p+1) + 2 \sum_{\ell=1}^p \phi_{[2p+1]}(p+1-\ell) \cos(\frac{\ell j\pi}{n}))} - 1, \quad j = 1, \dots, m, \tag{2.55}$$

where  $m := \min(n, n + p - 2)$ . For  $p = 1, \dots, 5$ , Eq. (2.54) gives

$$e_1(\theta) = \frac{6(1 - \cos \theta)}{2 + \cos \theta}, \tag{2.56}$$

$$e_2(\theta) = \frac{20(3 - 2 \cos \theta - \cos(2\theta))}{33 + 26 \cos \theta + \cos(2\theta)}, \tag{2.57}$$

$$e_3(\theta) = \frac{42(40 - 15 \cos \theta - 24 \cos(2\theta) - \cos(3\theta))}{1208 + 1191 \cos \theta + 120 \cos(2\theta) + \cos(3\theta)}, \tag{2.58}$$

$$e_4(\theta) = \frac{72(1225 - 154 \cos \theta - 952 \cos(2\theta) - 118 \cos(3\theta) - \cos(4\theta))}{78095 + 88234 \cos \theta + 14608 \cos(2\theta) + 502 \cos(3\theta) + \cos(4\theta)}, \tag{2.59}$$

$$e_5(\theta) = \frac{110(67956 + 5670 \cos \theta - 59520 \cos(2\theta) - 13605 \cos(3\theta) - 500 \cos(4\theta) - \cos(5\theta))}{7862124 + 9738114 \cos \theta + 2203488 \cos(2\theta) + 152637 \cos(3\theta) + 2036 \cos(4\theta) + \cos(5\theta)}. \tag{2.60}$$

In view of (2.55), Eqs. (2.56)–(2.59) are the analogs of formulas (117), (130), (135), (140) in [20]. Hence, (2.54)–(2.55) can be regarded as the generalization of the latter formulas to any degree  $p$ . Note that we can rewrite (2.55) according to (2.49) as follows:

$$\begin{aligned} \frac{\lambda^h - \lambda}{\lambda} &= \frac{e_p(\omega h)}{(\omega h)^2} - 1 \\ &= \frac{(2 - 2 \cos(\omega h))(\phi_{[2p-1]}(p) + 2 \sum_{\ell=1}^{p-1} \phi_{[2p-1]}(p - \ell) \cos(\ell \omega h))}{(\omega h)^2 (\phi_{[2p+1]}(p+1) + 2 \sum_{\ell=1}^p \phi_{[2p+1]}(p+1 - \ell) \cos(\ell \omega h))} - 1. \end{aligned} \tag{2.61}$$

Figure 40 shows the comparison between the analytical predictions and the eigenvalue errors for  $p = 4, 5, 6, 7$  and  $n = 500$  (for  $p = 1, 2, 3$  and  $n = 500$  we refer the reader to Figs. 7, 13, 26). We see an excellent agreement, up to a few outliers at the end of the numerical spectra, which are not present in the analytical predictions based on the symbol. The number of outliers does not increase with  $n$  and depends only on  $p$ , being  $p - 2$  for even degrees and  $p - 1$  for odd degrees; see [5, 23] for more details. Ignoring the outliers, the agreement becomes perfect in the limit of mesh refinement  $n \rightarrow \infty$ . It should be noted that, as in Fig. 26 for  $p = 3$ , also in Fig. 40 for  $p > 3$  we have some artificial associations, i.e., the associations of  $\lambda_{j,n}$  with  $n^2 e_p(i\pi/n)$  for  $j > n$ . Indeed, as it is clear from (2.55), the numerical eigenvalues  $\lambda_{j,n}$  for  $j > n$  do not have a corresponding analytical prediction, but this is not so disturbing because these eigenvalues are outliers.

### 2.5.2 $p$ -Degree $C^{p-2}$ B-Spline Discretization

When assuming the smoothness  $k = p - 2$ , there are only 2 different B-spline reference functions  $\phi_{j,[p,p-2]}$ ,  $j = 1, 2$ . The resulting symbols  $\mathbf{f}_{[p,p-2]}(\theta)$ ,  $\mathbf{h}_{[p,p-2]}(\theta)$ ,  $\mathbf{e}_{[p,p-2]}(\theta)$  are  $2 \times 2$  matrices for each  $\theta$ , and, consequently, some analytical computations are possible as the eigenvalue functions of the symbols can be computed explicitly by solving quadratic equations. We illustrate this statement by focusing on the eigenvalue functions of  $\mathbf{e}_{[p,p-2]}(\theta)$ , which immediately give the analytical predictions of the eigenvalue errors according to Remark 2.2.

For  $p = 2, \dots, 5$ , the characteristic polynomial of  $\mathbf{e}_{[p,p-2]}(\theta)$  is given by, respectively,<sup>2</sup>

<sup>2</sup> These polynomials have been obtained through a simple MAPLE program implementing Algorithm 2.1. The program first produced the symbolic expression of  $\mathbf{e}_{[p,p-2]}(\theta)$  and then computed  $C_{\mathbf{e}_{[p,p-2]}(\theta)}$  therefrom. For example, for  $p = 2$  the program returned

$$\mathbf{e}_{[2,0]}(\theta) = \frac{4}{3 - \cos \theta} \begin{bmatrix} 15 + 5 \cos \theta & (\cos \theta - 6)(2 + 2e^{i\theta}) \\ -5 - 5e^{-i\theta} & 11 - \cos \theta \end{bmatrix},$$

as in (2.24), and then computed  $C_{\mathbf{e}_{[2,0]}(\theta)}(\lambda)$ .

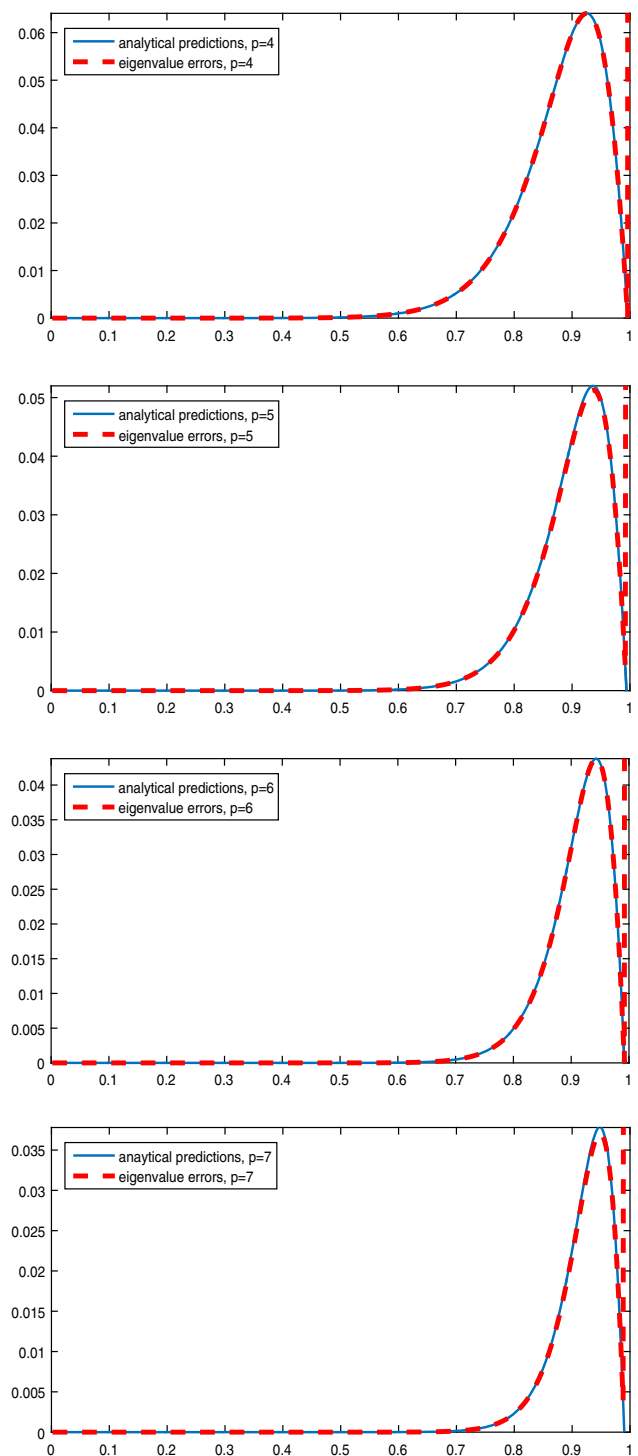


Fig. 40  $p$ -degree  $C^{p-1}$  B-spline discretization for  $p = 4, 5, 6, 7$ : analytical predictions  $e_p(i\pi/n)/(i\pi/n)^2 - 1$  and eigenvalue errors  $\lambda_{j,n}/\lambda_j - 1$  versus  $j/N_n$ ,  $j = 1, \dots, N_n$  ( $N_n = n + p - 2$ ,  $n = 500$ )

$$\begin{aligned}
 C_{\mathbf{e}_{[2,0]}(\theta)}(\lambda) &= \lambda^2 - \frac{8(13 + 2 \cos \theta)}{3 - \cos \theta} \lambda + \frac{240(1 - \cos \theta)}{3 - \cos \theta}, \\
 C_{\mathbf{e}_{[3,1]}(\theta)}(\lambda) &= \lambda^2 - \frac{12(141 - 32 \cos \theta - 4 \cos^2 \theta)}{65 - 36 \cos \theta + \cos^2 \theta} \lambda + \frac{1260(3 - 4 \cos \theta + \cos^2 \theta)}{65 - 36 \cos \theta + \cos^2 \theta}, \\
 C_{\mathbf{e}_{[4,2]}(\theta)}(\lambda) &= \lambda^2 - \frac{48(2455 - 1107 \cos \theta - 90 \cos^2 \theta + 2 \cos^3 \theta)}{4711 - 3459 \cos \theta + 261 \cos^2 \theta - \cos^3 \theta} \lambda + \frac{4032(65 - 101 \cos \theta + 37 \cos^2 \theta - \cos^3 \theta)}{4711 - 3459 \cos \theta + 261 \cos^2 \theta - \cos^3 \theta}, \\
 C_{\mathbf{e}_{[5,3]}(\theta)}(\lambda) &= \lambda^2 - \frac{20(1049629 - 662638 \cos \theta - 16779 \cos^2 \theta + 4016 \cos^3 \theta - 8 \cos^4 \theta)}{847269 - 760798 \cos \theta + 104070 \cos^2 \theta - 1542 \cos^3 \theta + \cos^4 \theta} \lambda \\
 &\quad + \frac{9900(4711 - 8170 \cos \theta + 3720 \cos^2 \theta - 262 \cos^3 \theta + \cos^4 \theta)}{847269 - 760798 \cos \theta + 104070 \cos^2 \theta - 1542 \cos^3 \theta + \cos^4 \theta}.
 \end{aligned}$$

Solving the quadratic equations  $C_{\mathbf{e}_{[p,p-2]}(\theta)}(\lambda) = 0$  for  $\lambda$ , we find

$$\lambda_{1,2}(\mathbf{e}_{[2,0]}(\theta)) = \frac{4(13 + 2 \cos \theta \mp \sqrt{\Delta_{[2,0]}})}{3 - \cos \theta}, \tag{2.62}$$

$$\lambda_{1,2}(\mathbf{e}_{[3,1]}(\theta)) = \frac{6(141 - 32 \cos \theta - 4 \cos^2 \theta \mp \sqrt{\Delta_{[3,1]}})}{65 - 36 \cos \theta + \cos^2 \theta}, \tag{2.63}$$

$$\lambda_{1,2}(\mathbf{e}_{[4,2]}(\theta)) = \frac{24(2455 - 1107 \cos \theta - 90 \cos^2 \theta + 2 \cos^3 \theta \mp \sqrt{\Delta_{[4,2]}})}{4711 - 3459 \cos \theta + 261 \cos^2 \theta - \cos^3 \theta}, \tag{2.64}$$

$$\lambda_{1,2}(\mathbf{e}_{[5,3]}(\theta)) = \frac{10(1049629 - 662638 \cos \theta - 16779 \cos^2 \theta + 4016 \cos^3 \theta - 8 \cos^4 \theta \mp \sqrt{\Delta_{[5,3]}})}{847269 - 760798 \cos \theta + 104070 \cos^2 \theta - 1542 \cos^3 \theta + \cos^4 \theta}, \tag{2.65}$$

where

$$\begin{aligned}
 \Delta_{[2,0]} &:= 124 + 112 \cos \theta - 11 \cos^2 \theta, \\
 \Delta_{[3,1]} &:= 13056 + 3856 \cos \theta - 7524 \cos^2 \theta \\
 &\quad + 1656 \cos^3 \theta - 19 \cos^4 \theta, \\
 \Delta_{[4,2]} &:= 3883520 - 530848 \cos \theta - 3000868 \cos^2 \theta \\
 &\quad + 1322920 \cos^3 \theta - 88847 \cos^4 \theta \\
 &\quad + 1726 \cos^5 \theta - 3 \cos^6 \theta, \\
 \Delta_{[5,3]} &:= 706564096000 - 350923718912 \cos \theta \\
 &\quad - 572059907828 \cos^2 \theta + 417724686832 \cos^3 \theta \\
 &\quad - 64449607643 \cos^4 \theta + 3219216532 \cos^5 \theta \\
 &\quad - 34270886 \cos^6 \theta + 114340 \cos^7 \theta - 35 \cos^8 \theta.
 \end{aligned}$$

In view of (2.49), we can formally express the eigenvalue errors as follows:

$$\frac{\lambda^h - \lambda}{\lambda} = \frac{\lambda_{1,2}(\mathbf{e}_{[p,p-2]}(\omega h))}{(\omega h)^2} - 1. \tag{2.66}$$

It should be said, however, that this formal way of writing could be a bit misleading in this case. Indeed, some numerical experiments reveal that  $\lambda_1(\mathbf{e}_{[p,p-2]}(\theta))$  is

increasing over  $[0, \pi]$  for all  $p$  and converges to  $\theta^2$  as  $p \rightarrow \infty$ , while  $\lambda_2(\mathbf{e}_{[p,p-2]}(\theta))$  is decreasing over  $[0, \pi]$  for all  $p$  and converges to a decreasing limit function as  $p \rightarrow \infty$ . Moreover, as already observed in Remark 2.3,

$$\begin{aligned}
 \lambda_1(\mathbf{e}_{[p,p-2]}(\pi)) &= \max_{\theta} \lambda_1(\mathbf{e}_{[p,p-2]}(\theta)) \\
 &< \min_{\theta} \lambda_2(\mathbf{e}_{[p,p-2]}(\theta)) = \lambda_2(\mathbf{e}_{[p,p-2]}(\pi)),
 \end{aligned}$$

i.e., we have two spectral branches for all  $p$  (although they tend to merge into a unique branch as  $p \rightarrow \infty$ ; see Table 1). Therefore, the analytical predictions of the eigenvalue errors provided by Remark 2.2 should be expressed as follows:

$$\frac{\lambda_{j,n}}{\lambda_j} - 1 \approx \frac{y_j}{\left(\frac{j\pi}{n}\right)^2} - 1, \quad j = 1, \dots, m, \tag{2.67}$$

where  $m := \min(2n, 2n + p - 3)$  and

$$y_j := \begin{cases} \lambda_1\left(\mathbf{e}_{[p,p-2]}\left(\frac{j\pi}{n}\right)\right), & j = 1, \dots, n, \\ \lambda_2\left(\mathbf{e}_{[p,p-2]}\left(\frac{(2n-j+1)\pi}{n}\right)\right), & j = n+1, \dots, 2n. \end{cases} \tag{2.68}$$

**Table 1** Computation of  $\lambda_1(\mathbf{e}_{[p,p-2]}(\pi)) = \max_{\theta} \lambda_1(\mathbf{e}_{[p,p-2]}(\theta))$  and  $\lambda_2(\mathbf{e}_{[p,p-2]}(\pi)) = \min_{\theta} \lambda_2(\mathbf{e}_{[p,p-2]}(\theta))$  for  $p = 2, \dots, 9$

$p$	2	3	4	5	6	7	8	9	$\infty$
$\lambda_1(\mathbf{e}_{[p,p-2]}(\pi))$	10.000000	9.882353	9.870968	9.869754	9.869621	9.869606	9.869605	9.869604	$\pi^2$
$\lambda_2(\mathbf{e}_{[p,p-2]}(\pi))$	12.000000	10.000000	9.882353	9.870968	9.869754	9.869621	9.869606	9.869605	$\pi^2$

Note that the point in which  $\lambda_2(\mathbf{e}_{[p,p-2]}(\theta))$  is evaluated is  $\frac{(2n-j+1)\pi}{n}$  and not  $\frac{j\pi}{n}$ ; this is the reason for which (2.66) could be a bit misleading. Note also that, as explained in Remark 2.2, the sampling procedure adopted in Sects. 2.3.2 and 2.4.2 is based on direct comparisons between the samples of  $\lambda_1(\mathbf{e}_{[p,p-2]}(\theta))$ ,  $\lambda_2(\mathbf{e}_{[p,p-2]}(\theta))$  and the numerical eigenvalues  $\lambda_{j,n}$ , and it is therefore slightly more accurate than the sampling procedure (2.67)–(2.68). However, in the limit of mesh refinement  $n \rightarrow \infty$  (actually, already for  $n = 500$  as in Figs. 20 and 32) these sampling procedures are indistinguishable.

### 2.5.3 $p$ -Degree $C^0$ B-Spline Discretization

When assuming the minimal smoothness  $k = 0$ , there are  $p$  different B-spline reference functions  $\phi_{j,[p,0]}$ ,  $j = 1, \dots, p$ . Inside the interval  $[0, 1]$ , they coincide with Bernstein polynomials of degree  $p$ ; see, e.g., [2]. The resulting symbols  $\mathbf{f}_{[p,0]}(\theta)$ ,  $\mathbf{h}_{[p,0]}(\theta)$ ,  $\mathbf{e}_{[p,0]}(\theta)$  are  $p \times p$  matrices for each  $\theta$  and are given by (2.38)–(2.40) for  $k = 0$ . Since  $\eta = 2$  (see (2.34)), they simplify to

$$\mathbf{f}_{[p,0]}(\theta) = \mathbf{K}_{[p,0]}^{[0]} + \mathbf{K}_{[p,0]}^{[1]} e^{i\theta} + \left(\mathbf{K}_{[p,0]}^{[1]}\right)^T e^{-i\theta}, \tag{2.69}$$

$$\mathbf{h}_{[p,0]}(\theta) = \mathbf{M}_{[p,0]}^{[0]} + \mathbf{M}_{[p,0]}^{[1]} e^{i\theta} + \left(\mathbf{M}_{[p,0]}^{[1]}\right)^T e^{-i\theta}, \tag{2.70}$$

$$\mathbf{e}_{[p,0]}(\theta) = \left(\mathbf{h}_{[p,0]}(\theta)\right)^{-1} \mathbf{f}_{[p,0]}(\theta). \tag{2.71}$$

For  $p = 1, \dots, 5$ , the characteristic polynomial of  $\mathbf{e}_{[p,0]}(\theta)$  is given by, respectively,<sup>3</sup>

$$C_{\mathbf{e}_{[1,0]}(\theta)}(\lambda) = \lambda - \frac{6(1 - \cos \theta)}{2 + \cos \theta}, \tag{2.72}$$

$$C_{\mathbf{e}_{[2,0]}(\theta)}(\lambda) = \lambda^2 - \frac{8(13 + 2 \cos \theta)}{3 - \cos \theta} \lambda + \frac{240(1 - \cos \theta)}{3 - \cos \theta}, \tag{2.73}$$

$$C_{\mathbf{e}_{[3,0]}(\theta)}(\lambda) = \lambda^3 - \frac{30(18 - \cos \theta)}{4 + \cos \theta} \lambda^2 + \frac{360(32 + 3 \cos \theta)}{4 + \cos \theta} \lambda - \frac{25200(1 - \cos \theta)}{4 + \cos \theta}, \tag{2.74}$$

<sup>3</sup> These polynomials have been obtained through a simple MAPLE program implementing Algorithm 2.1. The program first produced the symbolic expression of  $\mathbf{e}_{[p,0]}(\theta)$  and then computed  $C_{\mathbf{e}_{[p,0]}(\theta)}$  therefrom.

$$C_{\mathbf{e}_{[4,0]}(\theta)}(\lambda) = \lambda^4 - \frac{24(75 + 2 \cos \theta)}{5 - \cos \theta} \lambda^3 + \frac{1008(133 - 3 \cos \theta)}{5 - \cos \theta} \lambda^2 - \frac{40320(59 + 4 \cos \theta)}{5 - \cos \theta} \lambda + \frac{5080320(1 - \cos \theta)}{5 - \cos \theta}, \tag{2.75}$$

$$C_{\mathbf{e}_{[5,0]}(\theta)}(\lambda) = \lambda^5 - \frac{70(67 - \cos \theta)}{6 + \cos \theta} \lambda^4 + \frac{6720(128 + \cos \theta)}{6 + \cos \theta} \lambda^3 - \frac{302400(163 - 2 \cos \theta)}{6 + \cos \theta} \lambda^2 + \frac{8467200(94 + 5 \cos \theta)}{6 + \cos \theta} \lambda - \frac{1676505600(1 - \cos \theta)}{6 + \cos \theta}. \tag{2.76}$$

The solutions of the characteristic equation  $C_{\mathbf{e}_{[p,0]}(\theta)}(\lambda) = 0$  with respect to  $\lambda$  are the eigenvalues  $\lambda_i(\mathbf{e}_{[p,0]}(\theta))$ ,  $i = 1, \dots, p$ , which immediately provide the analytical predictions of the eigenvalue errors according to Remark 2.2. Note that the equations  $C_{\mathbf{e}_{[p,0]}(\theta)}(\lambda) = 0$  for  $p = 1, 2, 3, 4$  are the analogs of formulas (116), (141), (144), (146) in [20]. Hence,  $C_{\mathbf{e}_{[p,0]}(\theta)}(\lambda) = 0$  can be regarded as the generalization of the latter formulas to any degree  $p$ . Some numerical experiments reveal that, for all  $p$ , the function  $\lambda_i(\mathbf{e}_{[p,0]}(\theta))$  is increasing or decreasing over  $[0, \pi]$ , depending on whether  $i$  is odd or even; moreover,  $\lambda_1(\mathbf{e}_{[p,0]}(\theta))$  converges to  $\theta^2$  as  $p \rightarrow \infty$ . The numerical experiments also confirm the existence of  $p$  spectral branches as stated in Remark 2.3, because for all  $p$  we have

$$\max_{\theta} \lambda_i(\mathbf{e}_{[p,0]}(\theta)) < \min_{\theta} \lambda_{i+1}(\mathbf{e}_{[p,0]}(\theta)), \quad i = 1, \dots, p - 1. \tag{2.77}$$

Therefore, the analytical predictions of the eigenvalue errors provided by Remark 2.2 are the following:

$$\frac{\lambda_{j,n}}{\lambda_j} - 1 \approx \frac{y_j}{\left(\frac{j\pi}{n}\right)^2} - 1, \quad j = 1, \dots, pn - 1, \tag{2.78}$$

where

$$y_j := \begin{cases} \lambda_1 \left( \mathbf{e}_{[p,0]} \left( \frac{j\pi}{n} \right) \right), & j = 1, \dots, n, \\ \lambda_2 \left( \mathbf{e}_{[p,0]} \left( \frac{(2n-j+1)\pi}{n} \right) \right), & j = n+1, \dots, 2n, \\ \lambda_3 \left( \mathbf{e}_{[p,0]} \left( \frac{(j-2n)\pi}{n} \right) \right), & j = 2n+1, \dots, 3n, \\ \lambda_4 \left( \mathbf{e}_{[p,0]} \left( \frac{(4n-j+1)\pi}{n} \right) \right), & j = 3n+1, \dots, 4n, \\ \vdots & \vdots \\ \lambda_p \left( \mathbf{e}_{[p,0]}(\theta_j) \right), & j = (p-1)n+1, \dots, pn, \end{cases}$$

and

$$\theta_j := \begin{cases} \frac{(j - (p-1)n)\pi}{n}, & \text{if } p \text{ is odd,} \\ \frac{(pn - j + 1)\pi}{n}, & \text{if } p \text{ is even.} \end{cases}$$

Figure 41 shows the comparison between the analytical predictions and the eigenvalue errors for  $p = 4, 5, 6, 7$  and  $n = 500$  (for  $p = 1, 2, 3$  and  $n = 500$  we refer the reader to Figures 7, 20, 38). We see an excellent agreement in all cases. Note that not all the  $p$  branches predicted by Remark 2.3 are visible in Fig. 41. For example, for  $p = 4$  the first and the second branch seem to merge into a single branch because the jump at  $j/N_n \approx 1/4$  is not visible ( $N_n = 4n - 1$ ). However, if we adopt a larger scale as in Fig. 42, then the jump at  $j/N_n \approx 1/4$  becomes evident. To see the actual jump in the curve of the eigenvalue errors one should turn the red dashed line into a continuous line and adopt a larger scale. The inaccuracy in the analytical prediction seems to disappear in the limit of mesh refinement  $n \rightarrow \infty$ . For example, in Fig. 42, with  $n = 500$ , the value of the analytical prediction at  $j/N_n \approx 1/4$  is about  $-0.0037$ . If we take  $n = 1000$ , this value rises to  $-0.0017$ . In order to completely remove the inaccuracy in the analytical prediction also for small values of  $n$ , one should adopt the sampling procedure we used in Sects. 2.2–2.4; see Remark 2.2.

**Remark 2.4** (Divergence of the FEA numerical spectrum with  $p$ ) The case of  $C^0$  B-spline discretization considered in this section corresponds to classical FEA. The spurious behavior of the FEA numerical spectrum, which results in the appearance of  $p - 1$  optical branches, was already observed in the engineering literature; see, e.g., [5, 20, 21, 23]. In particular, it was noted in [21] that the largest optical branch (the one associated with the largest

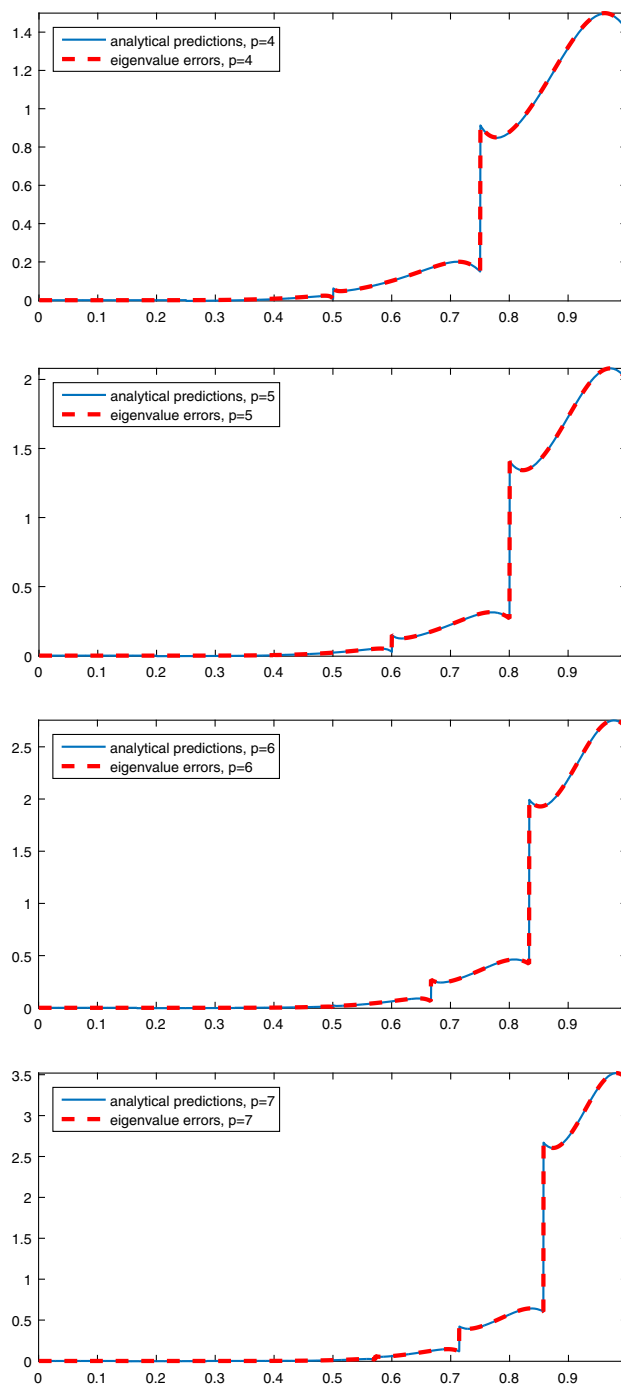


**Fig. 41**  $p$ -degree  $C^0$  B-spline discretization for  $p = 4, 5, 6, 7$ : analytical predictions  $y_j / (\frac{j\pi}{n})^2 - 1$  and eigenvalue errors  $\lambda_{j,n} / \lambda_j - 1$  versus  $j/N_n, j = 1, \dots, N_n$  ( $N_n = np - 1, n = 500$ )

eigenvalue function  $\lambda_p(\mathbf{e}_{[p,0]}(\theta))$  diverges to infinity as  $p \rightarrow \infty$ . Using the analytical predictions (2.78), we can quantify this divergence through the following indicators:

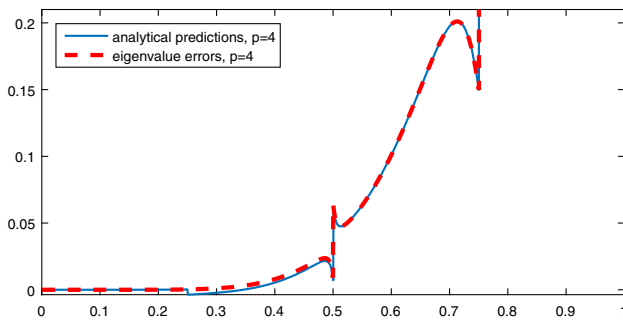


**Fig. 42** Quartic  $C^0$  B-spline discretization: analytical predictions  $y_j/(\frac{j\pi}{n})^2 - 1$  and eigenvalue errors  $\lambda_{j,n}/\lambda_j - 1$  versus  $j/N_n$ ,  $j = 1, \dots, N_n$  ( $N_n = 4n - 1$ ,  $n = 500$ ). To see the presence of the four branches, a larger scale is adopted with respect to Fig. 41

$$m_p := \lim_{n \rightarrow \infty} \min \left\{ \frac{y_j}{(\frac{j\pi}{n})^2} - 1 : j = (p-1)n + 1, \dots, pn - 1 \right\}$$

$$= \min_{\theta \in [0, \pi]} E_p(\theta),$$

$$M_p := \lim_{n \rightarrow \infty} \max \left\{ \frac{y_j}{(\frac{j\pi}{n})^2} - 1 : j = (p-1)n + 1, \dots, pn - 1 \right\}$$

$$= \max_{\theta \in [0, \pi]} E_p(\theta),$$

where

$$E_p(\theta) := \begin{cases} \frac{\lambda_p(\mathbf{e}_{[p,0]}(\theta))}{(\theta + (p-1)\pi)^2} - 1, & \text{if } p \text{ is odd,} \\ \frac{\lambda_p(\mathbf{e}_{[p,0]}(\pi - \theta))}{(\theta + (p-1)\pi)^2} - 1, & \text{if } p \text{ is even.} \end{cases}$$

The values of  $m_p$  and  $M_p$  are reported in Table 2 for  $p = 2, \dots, 14$ . They give a clear idea of the divergence rate with respect to  $p$  of the largest FEA branch.

### 3 Galerkin Discretization of Variable-Coefficient Eigenvalue Problems

Consider now a general one-dimensional variable-coefficient second-order eigenvalue problem:

$$\begin{cases} -(a(x)u_j'(x))' = \lambda_j b(x)u_j(x), & x \in (0, 1), \\ u_j(0) = u_j(1) = 0. \end{cases} \quad (3.1)$$

We assume that  $a, b \in C([0, 1])$  and  $a, b > 0$  on  $(0, 1)$ . The corresponding weak formulation reads as follows: find

eigenvalues  $\lambda_j \in \mathbb{R}^+$  and eigenfunctions  $u_j \in H_0^1([0, 1])$ , for  $j = 1, 2, \dots, \infty$ , such that, for all  $v \in H_0^1([0, 1])$ ,

$$a(u_j, v) = \lambda_j (b u_j, v),$$

where

$$a(u_j, v) := \int_0^1 a(x)u_j'(x)v'(x)dx,$$

$$(b u_j, v) := \int_0^1 b(x)u_j(x)v(x)dx.$$

In the Galerkin method, after fixing a set of basis functions  $\{\varphi_1, \dots, \varphi_{N_n}\} \subset H_0^1([0, 1])$ , we define the approximation space  $\mathcal{W}_n := \text{span}(\varphi_1, \dots, \varphi_{N_n})$  and we obtain approximations of the exact eigenpairs  $(\lambda_j, u_j)$ ,  $j = 1, 2, \dots, \infty$ , by solving the following Galerkin problem: find  $\lambda_{j,n} \in \mathbb{R}^+$  and  $u_{j,n} \in \mathcal{W}_n$ , for  $j = 1, \dots, N_n$ , such that, for all  $v_n \in \mathcal{W}_n$ ,

$$a(u_{j,n}, v_n) = \lambda_{j,n} (b u_{j,n}, v_n). \quad (3.2)$$

Assuming that both the exact and numerical eigenvalues are arranged in non-decreasing order, the pair  $(\lambda_{j,n}, u_{j,n})$  is taken as an approximation of the pair  $(\lambda_j, u_j)$  for all  $j = 1, \dots, N_n$ .

In view of the canonical identification of each function  $v_n \in \mathcal{W}_n$  with its coefficient vector with respect to the basis  $\{\varphi_1, \dots, \varphi_{N_n}\}$ , solving the Galerkin problem (3.2) is equivalent to solving the generalized matrix eigenvalue problem

$$\mathbf{K}_n(a)\mathbf{u}_{j,n} = \lambda_{j,n}\mathbf{M}_n(b)\mathbf{u}_{j,n}, \quad (3.3)$$

where  $\mathbf{u}_{j,n}$  is the coefficient vector of  $u_{j,n}$  with respect to  $\{\varphi_1, \dots, \varphi_{N_n}\}$  and

$$\mathbf{K}_n(a) := [a(\varphi_j, \varphi_i)]_{i,j=1}^{N_n} = \left[ \int_0^1 a(x)\varphi_j'(x)\varphi_i'(x)dx \right]_{i,j=1}^{N_n}, \quad (3.4)$$

$$\mathbf{M}_n(b) := [(b \varphi_j, \varphi_i)]_{i,j=1}^{N_n} = \left[ \int_0^1 b(x)\varphi_j(x)\varphi_i(x)dx \right]_{i,j=1}^{N_n}. \quad (3.5)$$

The matrices  $\mathbf{K}_n(a)$  and  $\mathbf{M}_n(b)$  are referred to as the stiffness and mass matrices. Due to our assumption that  $a, b > 0$  on  $(0, 1)$ , both  $\mathbf{K}_n(a)$  and  $\mathbf{M}_n(b)$  are always symmetric positive definite, regardless of the chosen basis functions  $\varphi_1, \dots, \varphi_{N_n}$ . Moreover, it is clear from (3.3) that

**Table 2** Values of the divergence indicators  $m_p$  and  $M_p$  for  $p = 2, \dots, 14$

$p$	2	3	4	5	6	7	8	9	10	11	12	13	14
$m_p$	0.17	0.46	0.85	1.34	1.93	2.60	3.37	4.21	5.15	6.16	7.26	8.44	9.71
$M_p$	0.66	1.02	1.50	2.08	2.76	3.52	4.37	5.31	6.33	7.44	8.62	9.90	11.25

the numerical eigenvalues  $\lambda_{j,n}, j = 1, \dots, N_n$ , are just the eigenvalues of the matrix

$$\mathbf{L}_n(a, b) := (\mathbf{M}_n(b))^{-1} \mathbf{K}_n(a). \tag{3.6}$$

Note that the matrices  $\mathbf{K}_n(1), \mathbf{M}_n(1), \mathbf{L}_n(1, 1)$  coincide with the matrices considered in Sect. 2:

$$\mathbf{K}_n(1) = \mathbf{K}_n, \quad \mathbf{M}_n(1) = \mathbf{M}_n, \quad \mathbf{L}_n(1, 1) = \mathbf{L}_n.$$

To see this, simply compare Eqs. (2.4)–(2.6) and Eqs. (3.4)–(3.6).

In the following we do a similar spectral analysis for the general eigenvalue problem (3.1) as we did before for the Laplacian eigenvalue problem (2.1) considering B-spline discretizations of various degree and smoothness on uniform meshes.

### 3.1 Linear $C^0$ B-Spline Discretization

In the linear  $C^0$  B-spline discretization of (3.1) on a uniform mesh with stepsize  $\frac{1}{n}$ , the basis functions  $\varphi_1, \dots, \varphi_{N_n}$  are the linear  $C^0$  B-splines  $B_{2,[1,0]}, \dots, B_{n,[1,0]}$  (i.e., the hat-functions; see Fig. 1). The resulting normalized stiffness and mass matrices are given by

$$\begin{aligned} \frac{1}{n} \mathbf{K}_n(a) &:= \frac{1}{n} \left[ \int_0^1 a(x) B'_{j+1,[1,0]}(x) B'_{i+1,[1,0]}(x) dx \right]_{i,j=1}^{n-1}, \\ n \mathbf{M}_n(b) &:= n \left[ \int_0^1 b(x) B_{j+1,[1,0]}(x) B_{i+1,[1,0]}(x) dx \right]_{i,j=1}^{n-1}. \end{aligned}$$

Now, for any function  $\alpha : [0, 1] \rightarrow \mathbb{C}$ , the matrix

$$\mathbf{D}_m(\alpha) := \begin{bmatrix} \alpha\left(\frac{1}{m}\right) & & & \\ & \alpha\left(\frac{2}{m}\right) & & \\ & & \ddots & \\ & & & \alpha(1) \end{bmatrix}$$

is referred to as the  $m$ -th diagonal sampling matrix generated by  $\alpha$ . Thanks to the local support property of the hat-functions, i.e.,

$$\text{supp}(B_{i+1,[1,0]}) = \left[ \frac{i-1}{n}, \frac{i+1}{n} \right], \quad i = 1, \dots, n-1,$$

for large values of  $n$  the support of  $B_{i+1,[1,0]}$  is located near the point  $\frac{i}{n-1}$  for all  $i = 1, \dots, n-1$ . Therefore, the matrices  $\frac{1}{n} \mathbf{K}_n(a)$  and  $n \mathbf{M}_n(b)$  are approximately equal to  $\mathbf{D}_{n-1}(a) \left(\frac{1}{n} \mathbf{K}_n(1)\right)$  and  $\mathbf{D}_{n-1}(b) (n \mathbf{M}_n(1))$ , respectively, as long as  $n$  is large enough. Indeed, for all  $i, j = 1, \dots, n-1$  we have

$$\begin{aligned} \left(\frac{1}{n} \mathbf{K}_n(a)\right)_{ij} &= \frac{1}{n} \int_0^1 a(x) B'_{j+1,[1,0]}(x) B'_{i+1,[1,0]}(x) dx \\ &= \frac{1}{n} \int_{\frac{i-1}{n}}^{\frac{i+1}{n}} a(x) B'_{j+1,[1,0]}(x) B'_{i+1,[1,0]}(x) dx \\ &\approx \frac{1}{n} a\left(\frac{i}{n-1}\right) \int_{\frac{i-1}{n}}^{\frac{i+1}{n}} B'_{j+1,[1,0]}(x) B'_{i+1,[1,0]}(x) dx \\ &= a\left(\frac{i}{n-1}\right) \frac{1}{n} \int_0^1 B'_{j+1,[1,0]}(x) B'_{i+1,[1,0]}(x) dx \\ &= a\left(\frac{i}{n-1}\right) \left(\frac{1}{n} \mathbf{K}_n(1)\right)_{ij}, \end{aligned}$$

or, in matrix form,

$$\frac{1}{n} \mathbf{K}_n(a) \approx \mathbf{D}_{n-1}(a) \left(\frac{1}{n} \mathbf{K}_n(1)\right). \tag{3.7}$$

Similarly,

$$n \mathbf{M}_n(b) \approx \mathbf{D}_{n-1}(b) (n \mathbf{M}_n(1)). \tag{3.8}$$

The approximations (3.7)–(3.8) can be made rigorous by showing that

$$\lim_{n \rightarrow \infty} \left\| \frac{1}{n} \mathbf{K}_n(a) - \mathbf{D}_{n-1}(a) \left(\frac{1}{n} \mathbf{K}_n(1)\right) \right\| = 0, \tag{3.9}$$

$$\lim_{n \rightarrow \infty} \left\| n \mathbf{M}_n(b) - \mathbf{D}_{n-1}(b) (n \mathbf{M}_n(1)) \right\| = 0, \tag{3.10}$$

where  $\|\cdot\|$  is the classical 2-norm of matrices. Since  $\{\mathbf{D}_m(\alpha)\}_m \sim_{\text{GLT}} \alpha(x)$  for all  $\alpha \in C([0, 1])$  and since we know from Sect. 2.2 that

$$\begin{aligned} \left\{ \frac{1}{n} \mathbf{K}_n(1) \right\}_n &\sim_{\text{GLT}} f(\theta) := 2 - 2 \cos \theta, \\ \left\{ n \mathbf{M}_n(1) \right\}_n &\sim_{\text{GLT}} h(\theta) := \frac{2}{3} + \frac{1}{3} \cos \theta, \end{aligned}$$

the theory of GLT sequences yields

$$\begin{aligned} \left\{ \mathbf{D}_{n-1}(a) \left(\frac{1}{n} \mathbf{K}_n(1)\right) \right\}_n &\sim_{\text{GLT}} a(x) f(\theta), \\ \left\{ \mathbf{D}_{n-1}(b) (n \mathbf{M}_n(1)) \right\}_n &\sim_{\text{GLT}} b(x) h(\theta), \end{aligned}$$

and

$$\left\{ \frac{1}{n} \mathbf{K}_n(a) \right\}_n \sim_{\text{GLT}} a(x) f(\theta), \tag{3.11}$$

$$\left\{ n \mathbf{M}_n(b) \right\}_n \sim_{\text{GLT}} b(x) h(\theta), \tag{3.12}$$

$$\left\{ \frac{1}{n^2} \mathbf{L}_n(a, b) \right\}_n \sim_{\text{GLT}} \frac{a(x)}{b(x)} e(\theta) = (b(x) h(\theta))^{-1} a(x) f(\theta), \tag{3.13}$$

where  $\mathbf{L}_n(a, b) := (\mathbf{M}_n(b))^{-1} \mathbf{K}_n(a)$  and

$$e(\theta) := (h(\theta))^{-1}f(\theta) = \frac{6(1 - \cos \theta)}{2 + \cos \theta}.$$

We note in particular that (3.13) follows from (3.11)–(3.12) and the fact that any algebraic combination of GLT sequences is again a GLT sequence with its symbol given by the same algebraic combination of the symbols. In conclusion,  $a(x)f(\theta)$ ,  $b(x)h(\theta)$ ,  $\frac{a(x)}{b(x)}e(\theta)$  are the symbols of  $\{\frac{1}{n}\mathbf{K}_n(a)\}_n$ ,  $\{n\mathbf{M}_n(b)\}_n$ ,  $\{\frac{1}{n^2}\mathbf{L}_n(a, b)\}_n$ , respectively. Figure 43 depicts the diagram for the computation of these symbols. The relations (3.11)–(3.13) imply the singular value and eigenvalue distributions

$$\left\{ \frac{1}{n} \mathbf{K}_n(a) \right\}_n \sim_{\sigma, \lambda} a(x)f(\theta), \tag{3.14}$$

$$\left\{ n \mathbf{M}_n(b) \right\}_n \sim_{\sigma, \lambda} b(x)h(\theta), \tag{3.15}$$

$$\left\{ \frac{1}{n^2} \mathbf{L}_n(a, b) \right\}_n \sim_{\sigma, \lambda} \frac{a(x)}{b(x)}e(\theta). \tag{3.16}$$

In particular, the singular value distributions in (3.14)–(3.16) follow directly from (3.11)–(3.13) and the theory of GLT sequences; the eigenvalue distributions in (3.14)–(3.15) follow from (3.11)–(3.12) and the theory of GLT sequences, taking into account the symmetry of  $\mathbf{K}_n(a)$  and  $\mathbf{M}_n(b)$ ; and the eigenvalue distribution in (3.16) follows from the theory of GLT sequences in combination with the same symmetrization argument that we have applied in Sect. 2.2.

For each positive integer  $r$ , let  $\mathcal{G}_r$  be the uniform grid in  $[0, 1] \times [0, \pi]$  given by

$$\mathcal{G}_r := \left\{ \left( \frac{i}{r}, \frac{j\pi}{r} \right) : i, j = 1, \dots, r \right\}.$$

Compute the samples of the symbols  $a(x)f(\theta)$ ,  $b(x)h(\theta)$ ,  $\frac{a(x)}{b(x)}e(\theta)$  at the grid points  $(x, \theta) \in \mathcal{G}_r$ . Sort the samples of

$a(x)f(\theta)$  (resp.,  $b(x)h(\theta)$ ,  $\frac{a(x)}{b(x)}e(\theta)$ ) in increasing order and put them in a vector  $(w_1, w_2, \dots, w_{r^2})$  (resp.,  $(y_1, y_2, \dots, y_{r^2})$ ,  $(z_1, z_2, \dots, z_{r^2})$ ). Let  $\kappa_r, \xi_r, \zeta_r : [0, 1] \rightarrow \mathbb{R}$  be the piecewise linear non-decreasing functions that interpolate the samples  $(w_0 := w_1, w_1, w_2, \dots, w_{r^2})$ ,  $(y_0 := y_1, y_1, y_2, \dots, y_{r^2})$ ,  $(z_0 := z_1, z_1, z_2, \dots, z_{r^2})$  over the nodes  $(0, \frac{1}{r^2}, \frac{2}{r^2}, \dots, 1)$ , i.e.,

$$\kappa_r \left( \frac{\ell}{r^2} \right) := w_\ell, \quad \ell = 0, \dots, r^2, \tag{3.17}$$

$$\xi_r \left( \frac{\ell}{r^2} \right) := y_\ell, \quad \ell = 0, \dots, r^2, \tag{3.18}$$

$$\zeta_r \left( \frac{\ell}{r^2} \right) := z_\ell, \quad \ell = 0, \dots, r^2. \tag{3.19}$$

It turns out that  $\kappa_r, \xi_r, \zeta_r$  converge to three non-decreasing functions  $\kappa, \xi, \zeta : [0, 1] \rightarrow \mathbb{R}$ , which are referred to as the rearranged versions of  $a(x)f(\theta)$ ,  $b(x)h(\theta)$ ,  $\frac{a(x)}{b(x)}e(\theta)$ , respectively. The rearranged versions are of interest here because the distribution relations (3.14)–(3.16) continue to hold if the symbols are replaced by their rearranged versions, i.e.,

$$\left\{ \frac{1}{n} \mathbf{K}_n(a) \right\}_n \sim_{\sigma, \lambda} \kappa, \tag{3.20}$$

$$\left\{ n \mathbf{M}_n(b) \right\}_n \sim_{\sigma, \lambda} \xi, \tag{3.21}$$

$$\left\{ \frac{1}{n^2} \mathbf{L}_n(a, b) \right\}_n \sim_{\sigma, \lambda} \zeta. \tag{3.22}$$

Moreover, working with  $\kappa, \xi, \zeta$  is simpler than working with  $a(x)f(\theta)$ ,  $b(x)h(\theta)$ ,  $\frac{a(x)}{b(x)}e(\theta)$  because  $\kappa, \xi, \zeta$  are univariate non-decreasing functions defined on the unit interval  $[0, 1]$ . Actually, it can be shown that  $\kappa, \xi, \zeta$  are the unique non-decreasing functions defined on  $[0, 1]$  for which the asymptotic eigenvalue distributions in (3.20)–(3.22) are satisfied.

For some numerical experiments we focus on problem (3.1) with coefficients  $a(x) = 2 + 0.5x$  and  $b(x) = 1$ . Figures 44, 45, 46 show the graphs of the functions  $\kappa_r, \xi_r, \zeta_r$ , respectively, for  $r = 10000$ . Note that these graphs form a very good approximation of the graphs of  $\kappa, \xi, \zeta$ , respectively. The figures also show the eigenvalues of the corresponding matrices  $\frac{1}{n}\mathbf{K}_n(a)$ ,  $n\mathbf{M}_n(b)$ ,  $\frac{1}{n^2}\mathbf{L}_n(a, b)$  for  $n = 40$ . The eigenvalues of  $\frac{1}{n}\mathbf{K}_n(a)$  are arranged in increasing order so as to match the graph of  $\kappa_r$  (and  $\kappa$ ), and are represented by the red asterisks placed at the points  $(\frac{j}{n}, \lambda_j(\frac{1}{n}\mathbf{K}_n(a)))$ ,  $j = 1, \dots, n - 1$ . The same is true for the eigenvalues of  $n\mathbf{M}_n(b)$  and  $\frac{1}{n^2}\mathbf{L}_n(a, b)$ . We see from the figures that the eigenvalues of the matrices  $\frac{1}{n}\mathbf{K}_n(a)$ ,  $n\mathbf{M}_n(b)$ ,  $\frac{1}{n^2}\mathbf{L}_n(a, b)$  are approximately samples of the functions  $\kappa, \xi, \zeta$  over a uniform grid in their

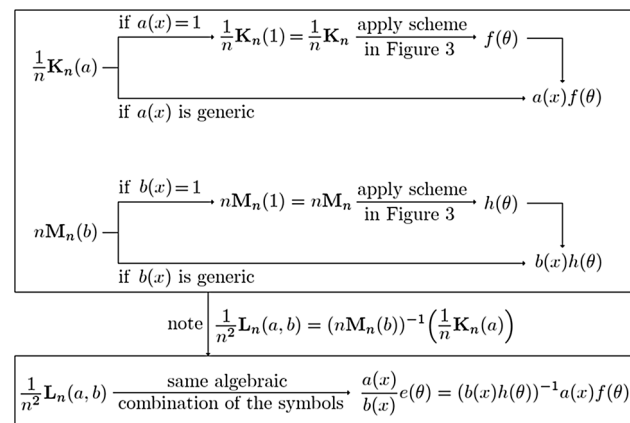
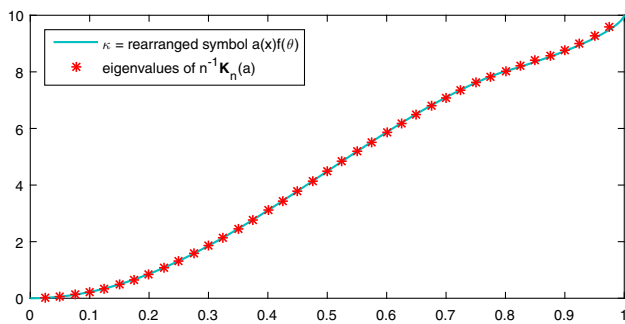
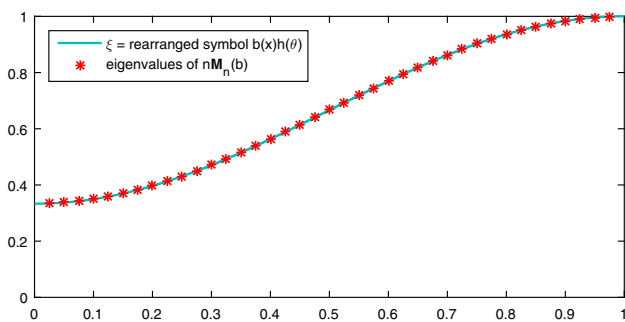


Fig. 43 Diagram for the computation of the symbols  $a(x)f(\theta)$ ,  $b(x)h(\theta)$ ,  $\frac{a(x)}{b(x)}e(\theta)$



**Fig. 44** Linear  $C^0$  B-spline discretization with  $a(x) = 2 + 0.5x$  and  $b(x) = 1$ : comparison between the rearranged version  $\kappa$  of the symbol  $a(x)f(\theta)$  and the eigenvalues of  $\frac{1}{n}\mathbf{K}_n(a)$  for  $n = 40$



**Fig. 45** Linear  $C^0$  B-spline discretization with  $a(x) = 2 + 0.5x$  and  $b(x) = 1$ : comparison between the rearranged version  $\xi$  of the symbol  $b(x)h(\theta)$  and the eigenvalues of  $n\mathbf{M}_n(b)$  for  $n = 40$

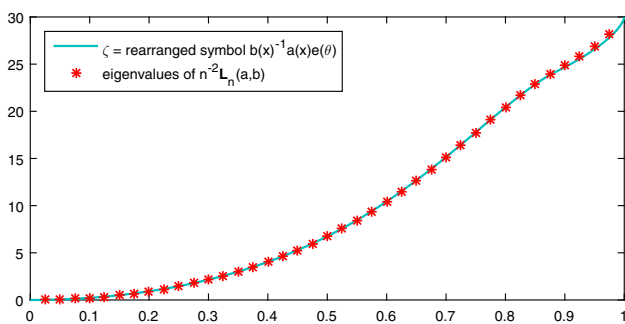


**Fig. 46** Linear  $C^0$  B-spline discretization with  $a(x) = 2 + 0.5x$  and  $b(x) = 1$ : comparison between the rearranged version  $\zeta$  of the symbol  $\frac{a(x)}{b(x)}e(\theta)$  and the eigenvalues of  $\frac{1}{n^2}\mathbf{L}_n(a, b)$  for  $n = 40$

domain  $[0, 1]$ . This agrees with the interpretation of the eigenvalue distributions  $\{\frac{1}{n}\mathbf{K}_n(a)\}_n \sim \lambda\kappa$ ,  $\{n\mathbf{M}_n(b)\}_n \sim \lambda\xi$ ,  $\{\frac{1}{n^2}\mathbf{L}_n(a, b)\}_n \sim \lambda\zeta$  given in Sect. 2.2.

Considering that the eigenvalues of  $\frac{1}{n^2}\mathbf{L}_n(a, b)$  (sorted in increasing order) are approximately equal to the uniform samples  $\zeta(\frac{j}{n})$ ,  $j = 1, \dots, n - 1$ , the eigenvalues of  $\mathbf{L}_n(a, b)$  (i.e., the numerical eigenvalues  $\lambda_{j,n}$ ,  $j = 1, \dots, n - 1$ ) are

approximately equal to  $n^2\zeta(\frac{j}{n})$ ,  $j = 1, \dots, n - 1$ . Consequently, we have

$$\frac{\lambda_{j,n}}{\lambda_j} - 1 \approx \frac{n^2\zeta_r(\frac{j}{n})}{\lambda_j} - 1, \quad j = 1, \dots, n - 1, \quad (3.23)$$

where  $\lambda_j$ ,  $j = 1, 2, \dots, \infty$ , are the exact eigenvalues. The unknown exact eigenvalues  $\lambda_1, \dots, \lambda_{n-1}$  can be approximated by the first  $n - 1$  eigenvalues of  $\mathbf{L}_{n'}(a, b)$  with  $n' \gg n$ . Figure 47 depicts the (approximate) analytical predictions  $n^2\zeta_r(\frac{j}{n})/\lambda_{j,n'} - 1$  and the (approximate) eigenvalue errors  $\lambda_{j,n}/\lambda_{j,n'} - 1$  versus  $j/(n - 1)$ , for  $j = 1, \dots, n - 1$  ( $n = 200$ ,  $n' = 1500$ ,  $r = 10000$ ). We see from the figure that the analytical prediction is excellent for all the eigenvalues except for the very small ones. The inaccuracy for small eigenvalues is (partially) due to the fact that we used  $\zeta_r$  instead of  $\zeta$  as the latter is not explicitly available. Figure 48 shows the improvement in the analytical prediction when  $r$  increases. Note that in Fig. 48 we only plot the smallest eigenvalue errors (one fifth of the spectrum) because for the other eigenvalue errors the analytical predictions remain essentially the same as in Fig. 47 for all  $r \geq 2500$ .

**Remark 3.1** (Numerical instability of the analytical predictions for small eigenvalues) As observed in Fig. 47, the analytical predictions are not very accurate for small eigenvalues. Besides the replacement of  $\zeta$  by  $\zeta_r$ , a possible (more hidden) reason resides in the fact that the approximations (3.23) may not be completely reliable from a numerical point of view. Indeed, while it is true that the eigenvalues  $\frac{1}{n^2}\lambda_{j,n}$  of  $\frac{1}{n^2}\mathbf{L}_n(a, b)$  are approximately equal to the uniform samples  $\zeta(\frac{j}{n})$  — this is the meaning of the eigenvalue distribution  $\{\frac{1}{n^2}\mathbf{L}_n(a, b)\}_n \sim \lambda\zeta$  — it is not necessarily true that the numerical eigenvalues  $\lambda_{j,n}$  are approximately equal to the values  $n^2\zeta(\frac{j}{n})$ : the latter approximations depend on whether  $n^2$  is large or small with respect to the differences  $\frac{1}{n^2}\lambda_{j,n} - \zeta(\frac{j}{n})$ . More precisely, the

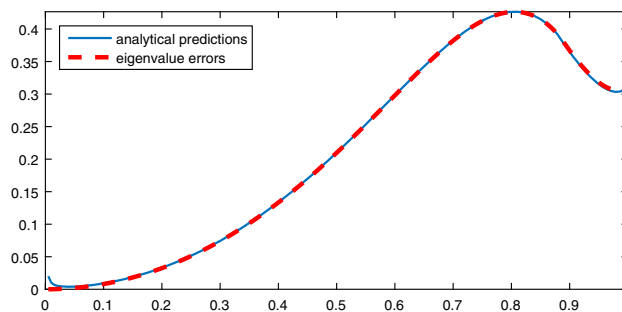


**Fig. 47** Linear  $C^0$  B-spline discretization with  $a(x) = 2 + 0.5x$  and  $b(x) = 1$ : analytical predictions  $n^2\zeta_r(\frac{j}{n})/\lambda_{j,n'} - 1$  and eigenvalue errors  $\lambda_{j,n}/\lambda_{j,n'} - 1$  versus  $j/N_n$ ,  $j = 1, \dots, N_n$  ( $N_n = n - 1$ ,  $n = 200$ ,  $n' = 1500$ ,  $r = 10000$ )

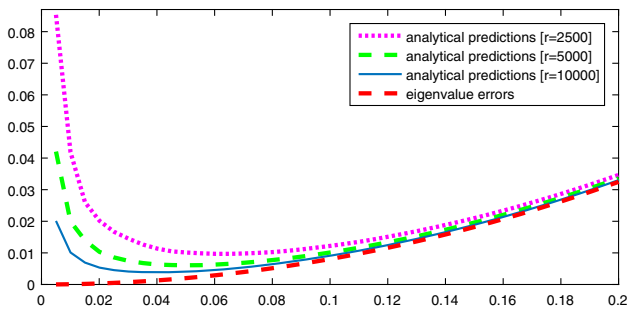


**Fig. 48** Linear  $C^0$  B-spline discretization with  $a(x) = 2 + 0.5x$  and  $b(x) = 1$ : analytical predictions  $n^2\zeta_r(\frac{j}{n})/\lambda_{j,n'} - 1$  and eigenvalue errors  $\lambda_{j,n}/\lambda_{j,n'} - 1$  versus  $j/N_n$ ,  $j = 1, \dots, N_n/5$  ( $N_n = n - 1$ ,  $n = 200$ ,  $n' = 1500$ )

(reliable) approximations  $\zeta(\frac{j}{n}) \approx \frac{1}{n^2} \lambda_{j,n}$  imply the approximations  $\zeta(\frac{j}{n}) - \frac{1}{n^2} \lambda_j \approx \frac{1}{n^2} \lambda_{j,n} - \frac{1}{n^2} \lambda_j$ , which in turn imply the relative approximations

$$\frac{\zeta(\frac{j}{n}) - \frac{1}{n^2} \lambda_j}{\frac{1}{n^2} \lambda_j} \approx \frac{\frac{1}{n^2} \lambda_{j,n} - \frac{1}{n^2} \lambda_j}{\frac{1}{n^2} \lambda_j} \tag{3.24}$$

provided that  $\frac{1}{n^2} \lambda_j$  is not too close to 0. This explains why the analytical predictions (left-hand side of (3.24)) may not be so accurate approximations of the eigenvalue errors (right-hand side of (3.24)) when  $\lambda_j$  is small (with respect to  $n^2$ ).

It should be said at this point that the knowledge of the symbol and its rearranged version  $\zeta$  does not provide us with a unique methodology to obtain analytical predictions for the eigenvalue errors. Actually, the choice of the sampling grid represents a degree of freedom since the sampling procedure described before is not the only possible one to obtain analytical predictions for the eigenvalue errors. Indeed, an eigenvalue distribution such as  $\{\frac{1}{n^2} \mathbf{L}_n(a, b)\}_n \sim \lambda \zeta$  only means that, for large  $n$ , the eigenvalues of  $\frac{1}{n^2} \mathbf{L}_n(a, b)$  are approximately uniform samples of  $\zeta$  over its domain  $[0, 1]$ . This does not specify anything about the sampling grid to be used, except that it should be (almost) uniform. In the following we exploit this observation to improve our results, especially for small eigenvalues.

**Remark 3.2** (The best sampling grid) The sampling grid that gives the best analytical predictions for the eigenvalue errors will be called “the best grid” and will be denoted by  $\{\tau_1, \dots, \tau_{N_n}\}$  with  $N_n = n - 1$ . For each  $j = 1, \dots, N_n$ , the point  $\tau_j \in [0, 1]$  is the point where the distance between  $n^2\zeta(\tau_j)$  and  $\lambda_{j,n}$  is minimal. Is the best grid uniform? The answer is “no” in general, but the crucial aspect is that, as a consequence of the eigenvalue distribution  $\{\frac{1}{n^2} \mathbf{L}_n(a, b)\}_n \sim \lambda \zeta$ , the grid  $\{\tau_1, \dots, \tau_{N_n}\}$  is almost uniform

and, moreover, it tends to a uniform grid in the limit of mesh refinement  $n \rightarrow \infty$ . This shows in particular that an optimal asymptotically uniform grid *always exists*. Moreover, it suffices to choose a uniform grid close to  $\{\tau_1, \dots, \tau_{N_n}\}$  in order to obtain excellent analytical predictions for the eigenvalue errors. We now describe a procedure to approximately compute the best grid.

- Compute the numerical eigenvalues  $\lambda_{j,n}$ ,  $j = 1, \dots, N_n$ . This can be done by using a suitable numerical method (for example, the inverse subspace iteration method).
- Fix a large pair of values  $q, r \in \mathbb{N}$ , and compute the values  $n^2\zeta_r(i/q)$  for  $i = 1, \dots, q$ . For each  $j = 1, \dots, N_n$ , choose the point  $\tau'_j$  of the grid  $\{i/q : i = 1, \dots, q\}$  which minimizes the distance  $|n^2\zeta_r(\tau'_j) - \lambda_{j,n}|$ .

The grid  $\{\tau'_1, \dots, \tau'_{N_n}\}$  is called the approximated best grid. Note that the sequences  $\{\tau_1, \dots, \tau_{N_n}\}$  and  $\{\tau'_1, \dots, \tau'_{N_n}\}$  are both non-decreasing because the sequence  $\{\lambda_{1,n}, \dots, \lambda_{N_n,n}\}$  and the functions  $\zeta, \zeta_r$  are non-decreasing.

Consider again the example with coefficients  $a(x) = 2 + 0.5x$  and  $b(x) = 1$ . We apply the procedure described in Remark 3.2 (with  $r = 10000$  and  $q = 1000000$ ) to compute the approximated best grid  $\{\tau'_1, \dots, \tau'_{n-1}\}$ . The result is shown in Fig. 49, where we see that the approximated best grid is essentially uniform as its graph is essentially a straight line.

**Remark 3.3** (How to find a good sampling grid) The unpleasant aspect of the procedure described in Remark 3.2 to obtain the approximated best grid is that one has to compute all the numerical eigenvalues  $\lambda_{j,n}$  and this is, of course, practically unfeasible. However, the

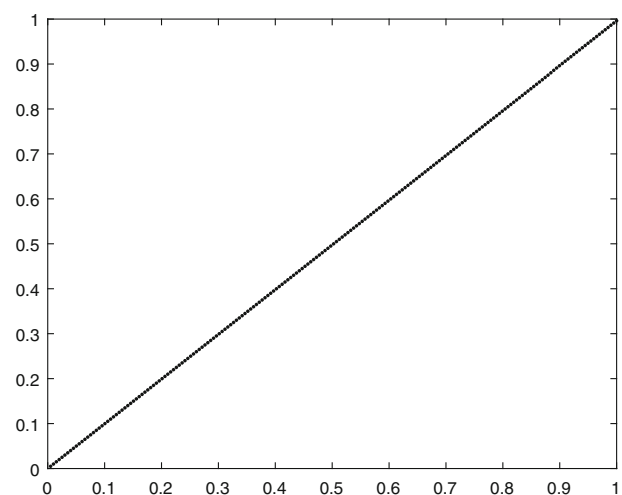


**Fig. 49** Linear  $C^0$  B-spline discretization with  $a(x) = 2 + 0.5x$  and  $b(x) = 1$ : grid points  $\tau'_j$  versus  $j/N_n$ ,  $j = 1, \dots, N_n$  ( $N_n = n - 1$ ,  $n = 200$ ,  $r = 10000$  and  $q = 1000000$ )



$$\mathbf{B}_{\lfloor\sqrt{m}\rfloor} = \alpha\left(\frac{j}{m}\right)\mathbf{T}_{\lfloor\sqrt{m}\rfloor}(2 - 2 \cos \theta) + \mathbf{E}_{\lfloor\sqrt{m}\rfloor},$$

where the error  $\mathbf{E}_{\lfloor\sqrt{m}\rfloor}$  tends to zero in 2-norm as  $m \rightarrow \infty$ . The latter assertion remains true if  $\lfloor\sqrt{m}\rfloor$  is replaced by any integer  $k_m$  such that  $k_m/m \rightarrow 0$  as  $m \rightarrow \infty$ . In other words, if we explore “locally” the matrix  $\mathbf{A}_m$ , using an ideal microscope and considering a large value of  $m$ , then we realize that the “local” structure of  $\mathbf{A}_m$  is approximately the Toeplitz structure generated by  $2 - 2 \cos \theta$  and weighted through the function  $\alpha(x)$ . In this sense the matrix  $\mathbf{A}_m$  is a “locally Toeplitz version” of  $\mathbf{T}_m(2 - 2 \cos \theta)$  weighted through  $\alpha$ ; and the matrix  $\frac{1}{n}\mathbf{K}_n(a)$  is a locally Toeplitz version of  $\frac{1}{n}\mathbf{K}_n(1) = \mathbf{T}_{n-1}(2 - 2 \cos \theta)$  weighted through  $a$ , due to (3.7) and (3.9). The reasoning we have just outlined is the key idea that led to the birth of locally Toeplitz sequences [14, 27] and, subsequently, of GLT sequences [1, 13–15, 17, 25, 26].

### 3.2 Quadratic $C^k$ B-Spline Discretization

We move on to quadratic B-spline discretizations of (3.1) on uniform meshes. As for the Laplacian eigenvalue problem (Sect. 2.3), we separately treat the  $C^1$  and  $C^0$  cases.

#### 3.2.1 Quadratic $C^1$ B-Spline Discretization

In the quadratic  $C^1$  B-spline discretization on a uniform mesh with stepsize  $\frac{1}{n}$ , the basis functions  $\varphi_1, \dots, \varphi_N$  are the quadratic  $C^1$  B-splines  $B_{2,[2,1]}, \dots, B_{n+1,[2,1]}$  (see Fig. 8). The resulting normalized stiffness and mass matrices are given by

$$\begin{aligned} \frac{1}{n}\mathbf{K}_n(a) &= \frac{1}{n} \left[ \int_0^1 a(x)B'_{j+1,[2,1]}(x)B'_{i+1,[2,1]}(x)dx \right]_{i,j=1}^n, \\ n\mathbf{M}_n(b) &= n \left[ \int_0^1 b(x)B_{j+1,[2,1]}(x)B_{i+1,[2,1]}(x)dx \right]_{i,j=1}^n. \end{aligned}$$

The argument to show that  $\{\frac{1}{n}\mathbf{K}_n(a)\}_n$  and  $\{n\mathbf{M}_n(b)\}_n$  are GLT sequences is the same as the argument we have applied in Sect. 3.1. Thanks to the local support property of the B-splines, the support of  $B_{i+1,[2,1]}$  is located near the point  $\frac{i}{n}$  for all  $i = 1, \dots, n$ ; this is clear from Eq. (2.8) and Fig. 8. Therefore, the matrices  $\frac{1}{n}\mathbf{K}_n(a)$  and  $n\mathbf{M}_n(b)$  are approximately equal to  $\mathbf{D}_n(a)(\frac{1}{n}\mathbf{K}_n(1))$  and  $\mathbf{D}_n(b)(n\mathbf{M}_n(1))$ , respectively, as long as  $n$  is large enough. Indeed, for all  $i, j = 1, \dots, n$  we have

$$\begin{aligned} \left(\frac{1}{n}\mathbf{K}_n(a)\right)_{ij} &= \frac{1}{n} \int_0^1 a(x)B'_{j+1,[2,1]}(x)B'_{i+1,[2,1]}(x)dx \\ &= \frac{1}{n} \int_{\text{supp}(B_{i+1,[2,1]})} a(x)B'_{j+1,[2,1]}(x)B'_{i+1,[2,1]}(x)dx \\ &\approx \frac{1}{n} a\left(\frac{i}{n}\right) \int_{\text{supp}(B_{i+1,[2,1]})} B'_{j+1,[2,1]}(x)B'_{i+1,[2,1]}(x)dx \\ &= a\left(\frac{i}{n}\right) \frac{1}{n} \int_0^1 B'_{j+1,[2,1]}(x)B'_{i+1,[2,1]}(x)dx \\ &= a\left(\frac{i}{n}\right) \left(\frac{1}{n}\mathbf{K}_n(1)\right)_{ij}, \end{aligned}$$

or, in matrix form,

$$\frac{1}{n}\mathbf{K}_n(a) \approx \mathbf{D}_n(a) \left(\frac{1}{n}\mathbf{K}_n(1)\right). \tag{3.25}$$

Similarly,

$$n\mathbf{M}_n(b) \approx \mathbf{D}_n(b) \left(n\mathbf{M}_n(1)\right). \tag{3.26}$$

The approximations (3.25)–(3.26) can be made rigorous by showing that

$$\begin{aligned} \lim_{n \rightarrow \infty} \left\| \frac{1}{n}\mathbf{K}_n(a) - \mathbf{D}_n(a) \left(\frac{1}{n}\mathbf{K}_n(1)\right) \right\| &= 0, \\ \lim_{n \rightarrow \infty} \left\| n\mathbf{M}_n(b) - \mathbf{D}_n(b) \left(n\mathbf{M}_n(1)\right) \right\| &= 0. \end{aligned}$$

Since  $\{\mathbf{D}_m(\alpha)\}_m \sim_{\text{GLT}} \alpha(x)$  for all  $\alpha \in C([0, 1])$  and since we know from Sect. 2.3.1 that

$$\begin{aligned} \left\{ \frac{1}{n}\mathbf{K}_n(1) \right\}_n &\sim_{\text{GLT}} f(\theta) := 1 - \frac{2}{3}\cos \theta - \frac{1}{3}\cos(2\theta), \\ \left\{ n\mathbf{M}_n(1) \right\}_n &\sim_{\text{GLT}} h(\theta) := \frac{11}{20} + \frac{13}{30}\cos \theta + \frac{1}{60}\cos(2\theta), \end{aligned}$$

the theory of GLT sequences yields

$$\begin{aligned} \left\{ \mathbf{D}_n(a) \left(\frac{1}{n}\mathbf{K}_n(1)\right) \right\}_n &\sim_{\text{GLT}} a(x)f(\theta), \\ \left\{ \mathbf{D}_n(b) \left(n\mathbf{M}_n(1)\right) \right\}_n &\sim_{\text{GLT}} b(x)h(\theta), \end{aligned}$$

and

$$\left\{ \frac{1}{n}\mathbf{K}_n(a) \right\}_n \sim_{\text{GLT}} a(x)f(\theta), \tag{3.27}$$

$$\left\{ n\mathbf{M}_n(b) \right\}_n \sim_{\text{GLT}} b(x)h(\theta), \tag{3.28}$$

$$\left\{ \frac{1}{n^2}\mathbf{L}_n(a, b) \right\}_n \sim_{\text{GLT}} \frac{a(x)}{b(x)}e(\theta) = (b(x)h(\theta))^{-1}a(x)f(\theta), \tag{3.29}$$

where  $\mathbf{L}_n(a, b) := (\mathbf{M}_n(b))^{-1}\mathbf{K}_n(a)$  and

$$e(\theta) := (h(\theta))^{-1}f(\theta) = \frac{20(3 - 2 \cos \theta - \cos(2\theta))}{33 + 26 \cos \theta + \cos(2\theta)}.$$

The diagram for the computation of the symbols  $a(x)f(\theta)$ ,  $b(x)h(\theta)$ ,  $\frac{a(x)}{b(x)}e(\theta)$  is the same as in Fig. 43. The relations (3.27)–(3.29) imply the singular value and eigenvalue distributions

$$\left\{ \frac{1}{n} \mathbf{K}_n(a) \right\}_n \sim_{\sigma, \lambda} a(x)f(\theta), \tag{3.30}$$

$$\left\{ n \mathbf{M}_n(b) \right\}_n \sim_{\sigma, \lambda} b(x)h(\theta), \tag{3.31}$$

$$\left\{ \frac{1}{n^2} \mathbf{L}_n(a, b) \right\}_n \sim_{\sigma, \lambda} \frac{a(x)}{b(x)}e(\theta). \tag{3.32}$$

Let  $\kappa, \xi, \zeta : [0, 1] \rightarrow \mathbb{R}$  be the rearranged versions of  $a(x)f(\theta), b(x)h(\theta), \frac{a(x)}{b(x)}e(\theta)$ , which are obtained as the limit of the piecewise linear functions  $\kappa_r, \xi_r, \zeta_r : [0, 1] \rightarrow \mathbb{R}$  in (3.17)–(3.19). Exactly as in Sect. 3.1, the distribution relations (3.30)–(3.32) continue to hold if the symbols are replaced by their rearranged versions, i.e.,

$$\left\{ \frac{1}{n} \mathbf{K}_n(a) \right\}_n \sim_{\sigma, \lambda} \kappa, \tag{3.33}$$

$$\left\{ n \mathbf{M}_n(b) \right\}_n \sim_{\sigma, \lambda} \xi, \tag{3.34}$$

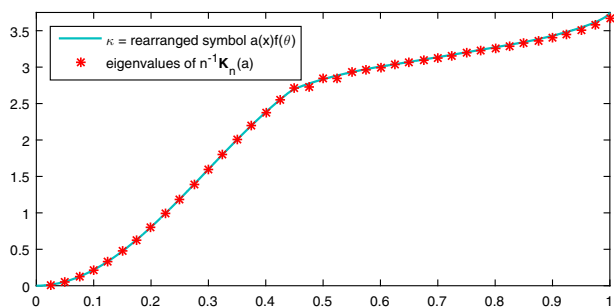


Fig. 51 Quadratic  $C^1$  B-spline discretization with  $a(x) = 2 + 0.5x$  and  $b(x) = 1$ : comparison between the rearranged version  $\kappa$  of the symbol  $a(x)f(\theta)$  and the eigenvalues of  $\frac{1}{n} \mathbf{K}_n(a)$  for  $n = 40$

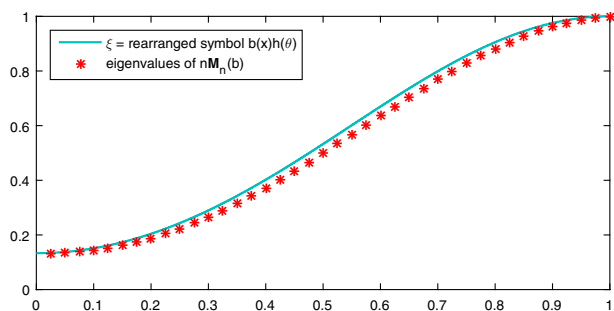


Fig. 52 Quadratic  $C^1$  B-spline discretization with  $a(x) = 2 + 0.5x$  and  $b(x) = 1$ : comparison between the rearranged version  $\xi$  of the symbol  $b(x)h(\theta)$  and the eigenvalues of  $n \mathbf{M}_n(b)$  for  $n = 40$

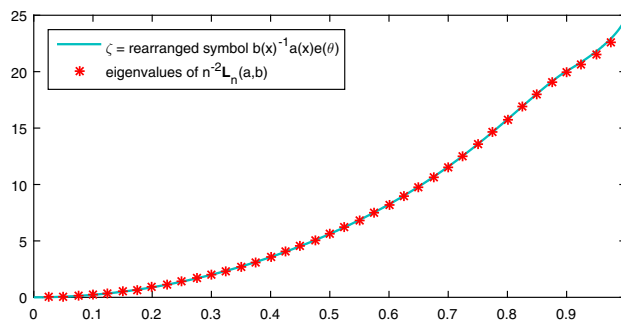


Fig. 53 Quadratic  $C^1$  B-spline discretization with  $a(x) = 2 + 0.5x$  and  $b(x) = 1$ : comparison between the rearranged version  $\zeta$  of the symbol  $\frac{a(x)}{b(x)}e(\theta)$  and the eigenvalues of  $\frac{1}{n^2} \mathbf{L}_n(a, b)$  for  $n = 40$

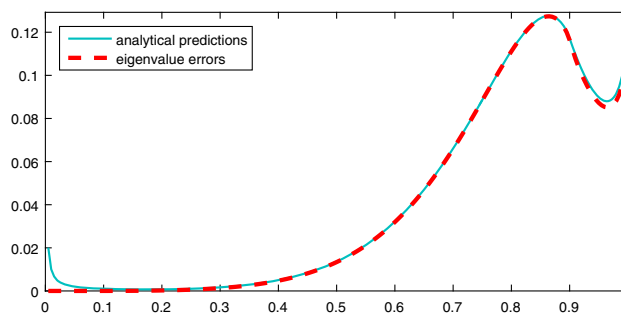


Fig. 54 Quadratic  $C^1$  B-spline discretization with  $a(x) = 2 + 0.5x$  and  $b(x) = 1$ : analytical predictions  $n^2 \zeta_r(\frac{j}{n}) / \lambda_{j,n'} - 1$  and eigenvalue errors  $\lambda_{j,n} / \lambda_{j,n'} - 1$  versus  $j/N_n, j = 1, \dots, N_n$  ( $N_n = n, n = 200, n' = 1500, r = 10000$ )

$$\left\{ \frac{1}{n^2} \mathbf{L}_n(a, b) \right\}_n \sim_{\sigma, \lambda} \zeta. \tag{3.35}$$

For some numerical experiments we focus on problem (3.1) with coefficients  $a(x) = 2 + 0.5x$  and  $b(x) = 1$ . Figures 51, 52, 53 show the graphs of the functions  $\kappa_r, \xi_r, \zeta_r$ , respectively, for  $r = 10000$ . Note that these graphs form a very good approximation of the graphs of  $\kappa, \xi, \zeta$ , respectively. The figures also show the eigenvalues of the corresponding matrices  $\frac{1}{n} \mathbf{K}_n(a), n \mathbf{M}_n(b), \frac{1}{n^2} \mathbf{L}_n(a, b)$  for  $n = 40$ . These eigenvalues are arranged in increasing order and are represented by the red asterisks positioned at  $\frac{j}{n}, j = 1, \dots, n$ . We see from the figures that the eigenvalues of  $\frac{1}{n} \mathbf{K}_n(a), n \mathbf{M}_n(b), \frac{1}{n^2} \mathbf{L}_n(a, b)$  are approximately samples of  $\kappa, \xi, \zeta$  over a uniform grid in  $[0, 1]$ . This agrees with the eigenvalue distributions in (3.33)–(3.35).

Considering that the eigenvalues of  $\frac{1}{n^2} \mathbf{L}_n(a, b)$  (sorted in increasing order) are approximately equal to the uniform samples  $\zeta(\frac{j}{n}), j = 1, \dots, n$ , the eigenvalues of  $\mathbf{L}_n(a, b)$  (i.e., the numerical eigenvalues  $\lambda_{j,n}, j = 1, \dots, n$ ) are approximately equal to  $n^2 \zeta(\frac{j}{n}), j = 1, \dots, n$ . Consequently, we have



i.e., in matrix form,

$$\frac{1}{n} \mathbf{K}_n(a) \approx (\mathbf{D}_n(a) \otimes \mathbf{I}_2)_\dagger \left( \frac{1}{n} \mathbf{K}_n(1) \right). \tag{3.36}$$

Similarly,

$$n\mathbf{M}_n(b) \approx (\mathbf{D}_n(b) \otimes \mathbf{I}_2)_\dagger \left( n\mathbf{M}_n(1) \right). \tag{3.37}$$

The approximations (3.36)–(3.37) can be made rigorous by showing that

$$\lim_{n \rightarrow \infty} \left\| \frac{1}{n} \mathbf{K}_n(a) - (\mathbf{D}_n(a) \otimes \mathbf{I}_2)_\dagger \left( \frac{1}{n} \mathbf{K}_n(1) \right) \right\| = 0,$$

$$\lim_{n \rightarrow \infty} \left\| n\mathbf{M}_n(b) - (\mathbf{D}_n(b) \otimes \mathbf{I}_2)_\dagger \left( n\mathbf{M}_n(1) \right) \right\| = 0.$$

Since  $\{\mathbf{D}_m(\alpha) \otimes \mathbf{I}_2\}_m \sim_{\text{GLT}} \alpha(x)\mathbf{I}_2$  for every  $\alpha \in C([0, 1])$  and since we know from Sect. 2.3.2 that

$$\left\{ \frac{1}{n} \mathbf{K}_n(1) \right\}_n \sim_{\text{GLT}} \mathbf{f}(\theta) := \frac{1}{3} \begin{bmatrix} 4 & -2 - 2e^{i\theta} \\ -2 - 2e^{-i\theta} & 8 - 4 \cos \theta \end{bmatrix},$$

$$\left\{ n\mathbf{M}_n(1) \right\}_n \sim_{\text{GLT}} \mathbf{h}(\theta) := \frac{1}{30} \begin{bmatrix} 4 & 3 + 3e^{i\theta} \\ 3 + 3e^{-i\theta} & 12 + 2 \cos \theta \end{bmatrix},$$

the theory of GLT sequences yields

$$\left\{ (\mathbf{D}_n(a) \otimes \mathbf{I}_2)_\dagger \left( \frac{1}{n} \mathbf{K}_n(1) \right) \right\}_n \sim_{\text{GLT}} a(x)\mathbf{f}(\theta),$$

$$\left\{ (\mathbf{D}_n(b) \otimes \mathbf{I}_2)_\dagger \left( n\mathbf{M}_n(1) \right) \right\}_n \sim_{\text{GLT}} b(x)\mathbf{h}(\theta),$$

and

$$\left\{ \frac{1}{n} \mathbf{K}_n(a) \right\}_n \sim_{\text{GLT}} a(x)\mathbf{f}(\theta), \tag{3.38}$$

$$\left\{ n\mathbf{M}_n(b) \right\}_n \sim_{\text{GLT}} b(x)\mathbf{h}(\theta), \tag{3.39}$$

$$\left\{ \frac{1}{n^2} \mathbf{L}_n(a, b) \right\}_n \sim_{\text{GLT}} \frac{a(x)}{b(x)} \mathbf{e}(\theta) = (b(x)\mathbf{h}(\theta))^{-1} a(x)\mathbf{f}(\theta), \tag{3.40}$$

where  $\mathbf{L}_n(a, b) := (\mathbf{M}_n(b))^{-1} \mathbf{K}_n(a)$  and

$$\mathbf{e}(\theta) := (\mathbf{h}(\theta))^{-1} \mathbf{f}(\theta)$$

$$= \frac{4}{3 - \cos \theta} \begin{bmatrix} 15 + 5 \cos \theta & (\cos \theta - 6)(2 + 2e^{i\theta}) \\ -5 - 5e^{-i\theta} & 11 - \cos \theta \end{bmatrix}.$$

Figure 56 depicts the diagram for the computation of the symbols  $a(x)\mathbf{f}(\theta)$ ,  $b(x)\mathbf{h}(\theta)$ ,  $\frac{a(x)}{b(x)} \mathbf{e}(\theta)$ . The relations (3.38)–(3.40) imply the singular value and eigenvalue distributions

$$\left\{ \frac{1}{n} \mathbf{K}_n(a) \right\}_n \sim_{\sigma, \lambda} a(x)\mathbf{f}(\theta), \tag{3.41}$$

$$\left\{ n\mathbf{M}_n(b) \right\}_n \sim_{\sigma, \lambda} b(x)\mathbf{h}(\theta), \tag{3.42}$$

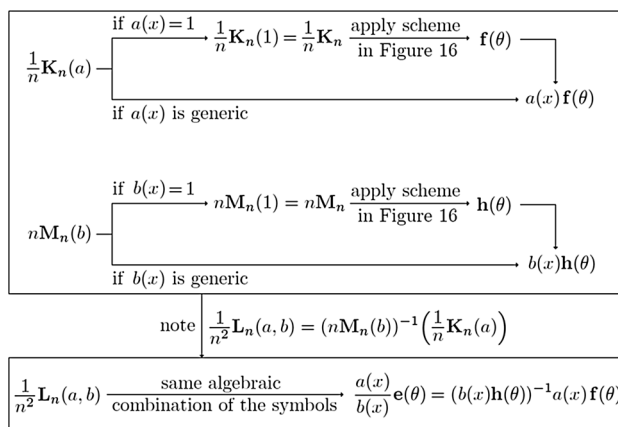


Fig. 56 Diagram for the computation of the symbols  $a(x)\mathbf{f}(\theta)$ ,  $b(x)\mathbf{h}(\theta)$ ,  $\frac{a(x)}{b(x)} \mathbf{e}(\theta)$

$$\left\{ \frac{1}{n^2} \mathbf{L}_n(a, b) \right\}_n \sim_{\sigma, \lambda} \frac{a(x)}{b(x)} \mathbf{e}(\theta). \tag{3.43}$$

The eigenvalue functions of  $a(x)\mathbf{f}(\theta)$ ,  $b(x)\mathbf{h}(\theta)$ ,  $\frac{a(x)}{b(x)} \mathbf{e}(\theta)$  are given by

$$\lambda_{1,2}(a(x)\mathbf{f}(\theta)) = a(x)\lambda_{1,2}(\mathbf{f}(\theta))$$

$$= a(x) \left( 2 - \frac{2}{3} \cos \theta \mp \frac{2}{3} \sqrt{3 + \cos^2 \theta} \right),$$

$$\lambda_{1,2}(b(x)\mathbf{h}(\theta)) = b(x)\lambda_{1,2}(\mathbf{h}(\theta))$$

$$= b(x) \left( \frac{4}{15} + \frac{1}{30} \cos \theta \mp \frac{1}{30} \sqrt{34 + 26 \cos \theta + \cos^2 \theta} \right),$$

$$\lambda_{1,2} \left( \frac{a(x)}{b(x)} \mathbf{e}(\theta) \right) = \frac{a(x)}{b(x)} \lambda_{1,2}(\mathbf{e}(\theta))$$

$$= \frac{a(x)}{b(x)} \frac{4}{3 - \cos \theta} \left( 13 + 2 \cos \theta \mp \sqrt{124 + 112 \cos \theta - 11 \cos^2 \theta} \right).$$

For each positive integer  $r$ , let  $\mathcal{G}_r$  be the uniform grid in  $[0, 1] \times [0, \pi]$  given by

$$\mathcal{G}_r := \left\{ \left( \frac{i}{r}, \frac{j\pi}{r} \right) : i, j = 1, \dots, r \right\}.$$

Compute the samples of the eigenvalue functions  $\lambda_{1,2}(a(x)\mathbf{f}(\theta))$ ,  $\lambda_{1,2}(b(x)\mathbf{h}(\theta))$ ,  $\lambda_{1,2}(\frac{a(x)}{b(x)} \mathbf{e}(\theta))$  at the grid points  $(x, \theta) \in \mathcal{G}_r$ . Sort the samples of  $\lambda_{1,2}(a(x)\mathbf{f}(\theta))$  (resp.,  $\lambda_{1,2}(b(x)\mathbf{h}(\theta))$ ,  $\lambda_{1,2}(\frac{a(x)}{b(x)} \mathbf{e}(\theta))$ ) in increasing order and put them in a vector  $(w_1, w_2, \dots, w_{2r^2})$  (resp.,  $(y_1, y_2, \dots, y_{2r^2})$ ,  $(z_1, z_2, \dots, z_{2r^2})$ ). Let  $\kappa_r, \xi_r, \zeta_r : [0, 1] \rightarrow \mathbb{R}$  be the piecewise linear non-decreasing functions that interpolate the samples  $(w_0 := w_1, w_1, w_2, \dots, w_{2r^2})$ ,  $(y_0 := y_1, y_1, y_2, \dots, y_{2r^2})$ ,  $(z_0 := z_1, z_1, z_2, \dots, z_{2r^2})$  over the nodes  $(0, \frac{1}{2r^2}, \frac{2}{2r^2}, \dots, 1)$ , i.e.,

$$\kappa_r\left(\frac{\ell}{2r^2}\right) := w_\ell, \quad \ell = 0, \dots, 2r^2, \tag{3.44}$$

$$\xi_r\left(\frac{\ell}{2r^2}\right) := y_\ell, \quad \ell = 0, \dots, 2r^2, \tag{3.45}$$

$$\zeta_r\left(\frac{\ell}{2r^2}\right) := z_\ell, \quad \ell = 0, \dots, 2r^2. \tag{3.46}$$

It turns out that  $\kappa_r, \xi_r, \zeta_r$  converge to three non-decreasing functions  $\kappa, \xi, \zeta : [0, 1] \rightarrow \mathbb{R}$ , which will be referred to as the rearranged versions of  $a(x)\mathbf{f}(\theta), b(x)\mathbf{h}(\theta), \frac{a(x)}{b(x)}\mathbf{e}(\theta)$ , respectively. The rearranged versions are of interest because the eigenvalue distributions in (3.41)–(3.43) continue to hold if the symbols are replaced by their rearranged versions, i.e.,

$$\left\{\frac{1}{n}\mathbf{K}_n(a)\right\}_n \sim \lambda \kappa, \tag{3.47}$$

$$\left\{n\mathbf{M}_n(b)\right\}_n \sim \lambda \xi, \tag{3.48}$$

$$\left\{\frac{1}{n^2}\mathbf{L}_n(a, b)\right\}_n \sim \lambda \zeta. \tag{3.49}$$

Moreover, working with  $\kappa, \xi, \zeta$  is much simpler than working with  $a(x)\mathbf{f}(\theta), b(x)\mathbf{h}(\theta), \frac{a(x)}{b(x)}\mathbf{e}(\theta)$  because  $\kappa, \xi, \zeta$  are scalar univariate non-decreasing functions defined on the unit interval  $[0, 1]$ . Again, it can be shown that  $\kappa, \xi, \zeta$  are the *unique* non-decreasing functions defined on  $[0, 1]$  for which the asymptotic eigenvalue distributions (3.47)–(3.49) are satisfied.

For some numerical experiments we focus on problem (3.1) with coefficients  $a(x) = 2 + 0.5x$  and  $b(x) = 1$ . Figures 57, 58, 59 show the graphs of the functions  $\kappa_r, \xi_r, \zeta_r$ , respectively, for  $r = 10000$ . Note that these graphs form a very good approximation of the graphs of  $\kappa, \xi, \zeta$ , respectively. The figures also show the eigenvalues of the corresponding matrices  $\frac{1}{n}\mathbf{K}_n(a), n\mathbf{M}_n(b), \frac{1}{n^2}\mathbf{L}_n(a, b)$  for  $n = 40$ . These eigenvalues are arranged in increasing order and are represented by the red asterisks positioned at  $\frac{j}{2n}$ ,

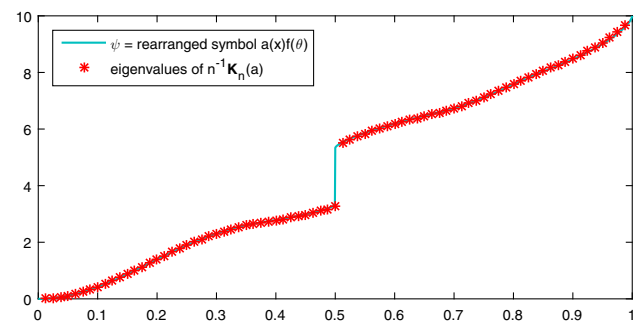


Fig. 57 Quadratic  $C^0$  B-spline discretization with  $a(x) = 2 + 0.5x$  and  $b(x) = 1$ : comparison between the rearranged version  $\kappa$  of the symbol  $a(x)\mathbf{f}(\theta)$  and the eigenvalues of  $\frac{1}{n}\mathbf{K}_n(a)$  for  $n = 40$

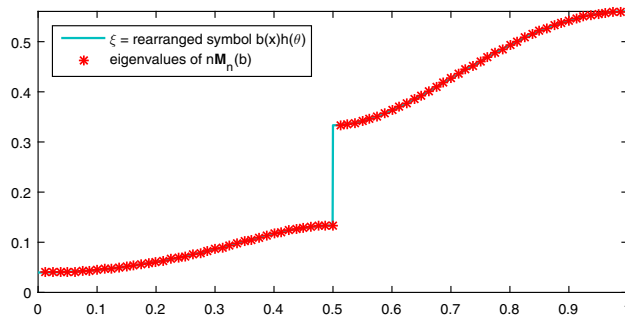


Fig. 58 Quadratic  $C^0$  B-spline discretization with  $a(x) = 2 + 0.5x$  and  $b(x) = 1$ : comparison between the rearranged version  $\xi$  of the symbol  $b(x)\mathbf{h}(\theta)$  and the eigenvalues of  $n\mathbf{M}_n(b)$  for  $n = 40$

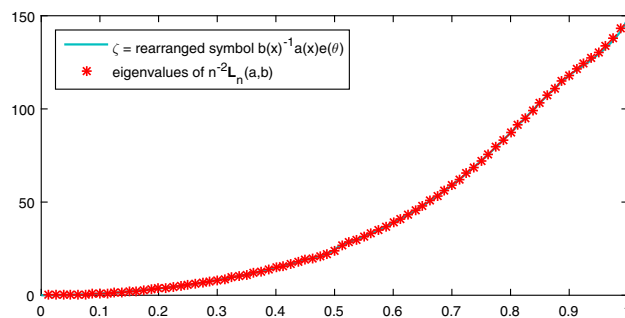


Fig. 59 Quadratic  $C^0$  B-spline discretization with  $a(x) = 2 + 0.5x$  and  $b(x) = 1$ : comparison between the rearranged version  $\zeta$  of the symbol  $\frac{a(x)}{b(x)}\mathbf{e}(\theta)$  and the eigenvalues of  $\frac{1}{n^2}\mathbf{L}_n(a, b)$  for  $n = 40$

$j = 1, \dots, 2n - 1$ . We see from the figures that the eigenvalues of  $\frac{1}{n}\mathbf{K}_n(a), n\mathbf{M}_n(b), \frac{1}{n^2}\mathbf{L}_n(a, b)$  are approximately samples of  $\kappa, \xi, \zeta$  over a uniform grid in  $[0, 1]$ . This agrees with the eigenvalue distributions (3.47)–(3.49).

Considering that the eigenvalues of  $\frac{1}{n^2}\mathbf{L}_n(a, b)$  (sorted in increasing order) are approximately equal to the uniform samples  $\zeta(\frac{j}{2n}), j = 1, \dots, 2n - 1$ , the eigenvalues of  $\mathbf{L}_n(a, b)$  (i.e., the numerical eigenvalues  $\lambda_{j,n}, j = 1, \dots, 2n - 1$ ) are approximately equal to  $n^2\zeta(\frac{j}{2n}), j = 1, \dots, 2n - 1$ . Consequently, we have

$$\frac{\lambda_{j,n}}{\lambda_j} - 1 \approx \frac{n^2\zeta\left(\frac{j}{2n}\right)}{\lambda_j} - 1, \quad j = 1, \dots, 2n - 1,$$

where  $\lambda_j, j = 1, 2, \dots, \infty$ , are the exact eigenvalues. The unknown exact eigenvalues  $\lambda_1, \dots, \lambda_{2n-1}$  can be approximated by the first  $2n - 1$  eigenvalues of  $\mathbf{L}_{n'}(a, b)$  with  $n' \gg n$ . Figure 60 depicts the (approximate) analytical predictions  $n^2\zeta_r(\frac{j}{2n})/\lambda_{j,n'} - 1$  and the (approximate) eigenvalue errors  $\lambda_{j,n}/\lambda_{j,n'} - 1$  versus  $j/(2n - 1)$ , for  $j = 1, \dots, 2n - 1$  ( $n = 200, n' = 1500, r = 10000$ ). We see that the analytical prediction is excellent for all eigenvalues except for the very small ones. Exactly as explained in Sect. 3.1, the accuracy can be substantially improved by



$$\begin{aligned} \left(\frac{1}{n}\mathbf{K}_n(a)\right)_{ij} &= \int_0^1 a(x)B'_{j+1,[p,k]}(x)B'_{i+1,[p,k]}(x)dx \\ &= \int_{\text{supp}(B_{i+1,[p,k]})} a(x)B'_{j+1,[p,k]}(x)B'_{i+1,[p,k]}(x)dx \\ &\approx a\left(\frac{[i/(p-k)]}{n}\right) \int_{\text{supp}(B_{i+1,[p,k]})} B'_{j+1,[p,k]}(x)B'_{i+1,[p,k]}(x)dx \\ &= a\left(\frac{[i/(p-k)]}{n}\right) \int_0^1 B'_{j+1,[p,k]}(x)B'_{i+1,[p,k]}(x)dx \\ &= a\left(\frac{[i/(p-k)]}{n}\right) \left(\frac{1}{n}\mathbf{K}_n(1)\right)_{ij}, \end{aligned}$$

i.e.,

$$\frac{1}{n}\mathbf{K}_n(a) \approx (\mathbf{D}_n(a) \otimes \mathbf{I}_{p-k}) \dagger \left(\frac{1}{n}\mathbf{K}_n(1)\right). \tag{3.50}$$

Similarly,

$$n\mathbf{M}_n(a) \approx (\mathbf{D}_n(b) \otimes \mathbf{I}_{p-k}) \dagger (n\mathbf{M}_n(1)). \tag{3.51}$$

The approximations (3.50)–(3.51) can be made rigorous by showing that

$$\begin{aligned} \lim_{n \rightarrow \infty} \left\| \frac{1}{n}\mathbf{K}_n(a) - (\mathbf{D}_n(a) \otimes \mathbf{I}_{p-k}) \dagger \left(\frac{1}{n}\mathbf{K}_n(1)\right) \right\| &= 0, \\ \lim_{n \rightarrow \infty} \left\| n\mathbf{M}_n(b) - (\mathbf{D}_n(b) \otimes \mathbf{I}_{p-k}) \dagger (n\mathbf{M}_n(1)) \right\| &= 0. \end{aligned}$$

Since  $\{\mathbf{D}_m(\alpha) \otimes \mathbf{I}_{p-k}\}_m \sim_{\text{GLT}} \alpha(x)\mathbf{I}_{p-k}$  for every  $\alpha \in C([0, 1])$  and since we know from Sect. 2.5 that

$$\begin{aligned} \left\{\frac{1}{n}\mathbf{K}_n(1)\right\}_n &\sim_{\text{GLT}} \mathbf{f}_{[p,k]}(\theta), \\ \left\{n\mathbf{M}_n(1)\right\}_n &\sim_{\text{GLT}} \mathbf{h}_{[p,k]}(\theta), \end{aligned}$$

with  $\mathbf{f}_{[p,k]}(\theta)$  and  $\mathbf{h}_{[p,k]}(\theta)$  being the  $(p-k) \times (p-k)$  matrix-valued functions in (2.38)–(2.39), the theory of GLT sequences yields

$$\begin{aligned} \left\{(\mathbf{D}_n(a) \otimes \mathbf{I}_{p-k}) \dagger \left(\frac{1}{n}\mathbf{K}_n(1)\right)\right\}_n &\sim_{\text{GLT}} a(x)\mathbf{f}_{[p,k]}(\theta), \\ \left\{(\mathbf{D}_n(b) \otimes \mathbf{I}_{p-k}) \dagger (n\mathbf{M}_n(1))\right\}_n &\sim_{\text{GLT}} a(x)\mathbf{h}_{[p,k]}(\theta), \end{aligned}$$

and

$$\left\{\frac{1}{n}\mathbf{K}_n(a)\right\}_n \sim_{\text{GLT}} a(x)\mathbf{f}_{[p,k]}(\theta), \tag{3.52}$$

$$\left\{n\mathbf{M}_n(b)\right\}_n \sim_{\text{GLT}} b(x)\mathbf{h}_{[p,k]}(\theta), \tag{3.53}$$

$$\begin{aligned} \left\{\frac{1}{n^2}\mathbf{L}_n(a, b)\right\}_n &\sim_{\text{GLT}} \frac{a(x)}{b(x)}\mathbf{e}_{[p,k]}(\theta) \\ &= (b(x)\mathbf{h}_{[p,k]}(\theta))^{-1}a(x)\mathbf{f}_{[p,k]}(\theta), \end{aligned} \tag{3.54}$$

where  $\mathbf{L}_n(a, b) := (\mathbf{M}_n(b))^{-1}\mathbf{K}_n(a)$  and

$$\mathbf{e}_{[p,k]}(\theta) := (\mathbf{h}_{[p,k]}(\theta))^{-1}\mathbf{f}_{[p,k]}(\theta).$$

The procedure to obtain the symbols  $a(x)\mathbf{f}_{[p,k]}(\theta)$ ,  $b(x)\mathbf{h}_{[p,k]}(\theta)$ ,  $\frac{a(x)}{b(x)}\mathbf{e}_{[p,k]}(\theta)$  is the same as in Fig. 56. Note that Fig. 43 is just a special case of Fig. 56, corresponding to the situation in which the block symbols have size  $1 \times 1$ , i.e., they are scalar symbols. This happens only in the case of maximal smoothness  $k = p - 1$ . The relations (3.52)–(3.54) imply the singular value and eigenvalue distributions

$$\left\{\frac{1}{n}\mathbf{K}_n(a)\right\}_n \sim_{\sigma, \lambda} a(x)\mathbf{f}_{[p,k]}(\theta), \tag{3.55}$$

$$\left\{n\mathbf{M}_n(b)\right\}_n \sim_{\sigma, \lambda} b(x)\mathbf{h}_{[p,k]}(\theta), \tag{3.56}$$

$$\left\{\frac{1}{n^2}\mathbf{L}_n(a, b)\right\}_n \sim_{\sigma, \lambda} \frac{a(x)}{b(x)}\mathbf{e}_{[p,k]}(\theta). \tag{3.57}$$

For each positive integer  $r$ , let  $\mathcal{G}_r$  be the uniform grid in  $[0, 1] \times [0, \pi]$  given by

$$\mathcal{G}_r := \left\{ \left(\frac{i}{r}, \frac{j\pi}{r}\right) : i, j = 1, \dots, r \right\}.$$

Compute the samples at the grid points  $(x, \theta) \in \mathcal{G}_r$  of the eigenvalue functions

$$\begin{aligned} \lambda_{1,2,\dots,p-k}(a(x)\mathbf{f}_{[p,k]}(\theta)) &= a(x)\lambda_{1,2,\dots,p-k}(\mathbf{f}_{[p,k]}(\theta)), \\ \lambda_{1,2,\dots,p-k}(b(x)\mathbf{h}_{[p,k]}(\theta)) &= b(x)\lambda_{1,2,\dots,p-k}(\mathbf{h}_{[p,k]}(\theta)), \\ \lambda_{1,2,\dots,p-k}\left(\frac{a(x)}{b(x)}\mathbf{e}_{[p,k]}(\theta)\right) &= \frac{a(x)}{b(x)}\lambda_{1,2,\dots,p-k}(\mathbf{e}_{[p,k]}(\theta)). \end{aligned}$$

Sort the samples of  $\lambda_{1,2,\dots,p-k}(a(x)\mathbf{f}_{[p,k]}(\theta))$  (resp.,  $\lambda_{1,2,\dots,p-k}(b(x)\mathbf{h}_{[p,k]}(\theta))$ ,  $\lambda_{1,2,\dots,p-k}\left(\frac{a(x)}{b(x)}\mathbf{e}_{[p,k]}(\theta)\right)$ ) in increasing order and put them in a vector  $(w_1, w_2, \dots, w_{(p-k)r^2})$  (resp.,  $(y_1, y_2, \dots, y_{(p-k)r^2})$ ,  $(z_1, z_2, \dots, z_{(p-k)r^2})$ ). Let

$$\kappa_{r,[p,k]}, \xi_{r,[p,k]}, \zeta_{r,[p,k]} : [0, 1] \rightarrow \mathbb{R}$$

be the piecewise linear non-decreasing functions that interpolate the samples  $(w_0 := w_1, w_1, w_2, \dots, w_{(p-k)r^2})$ ,  $(y_0 := y_1, y_1, y_2, \dots, y_{(p-k)r^2})$ ,  $(z_0 := z_1, z_1, z_2, \dots, z_{(p-k)r^2})$  over the nodes  $(0, \frac{1}{(p-k)r^2}, \frac{2}{(p-k)r^2}, \dots, 1)$ , i.e.,

$$\kappa_{r,[p,k]} \left(\frac{\ell}{(p-k)r^2}\right) := w_\ell, \quad \ell = 0, \dots, (p-k)r^2, \tag{3.58}$$

$$\xi_{r,[p,k]} \left(\frac{\ell}{(p-k)r^2}\right) := y_\ell, \quad \ell = 0, \dots, (p-k)r^2, \tag{3.59}$$

$$\zeta_{r,[p,k]} \left(\frac{\ell}{(p-k)r^2}\right) := z_\ell, \quad \ell = 0, \dots, (p-k)r^2. \tag{3.60}$$

It turns out that  $\kappa_{r,[p,k]}, \xi_{r,[p,k]}, \zeta_{r,[p,k]}$  converge, as  $r \rightarrow \infty$ , to three non-decreasing functions

$$\kappa_{[p,k]}, \zeta_{[p,k]}, \zeta'_{[p,k]} : [0, 1] \rightarrow \mathbb{R},$$

which will be referred to as the rearranged versions of  $a(x)\mathbf{f}_{[p,k]}(\theta)$ ,  $b(x)\mathbf{h}_{[p,k]}(\theta)$ ,  $\frac{a(x)}{b(x)}\mathbf{e}_{[p,k]}(\theta)$ , respectively. The eigenvalue distributions in (3.55)–(3.57) continue to hold if the symbols are replaced by their rearranged versions:

$$\left\{ \frac{1}{n} \mathbf{K}_n(a) \right\}_n \sim_{\lambda} \kappa_{[p,k]}, \tag{3.61}$$

$$\left\{ n \mathbf{M}_n(b) \right\}_n \sim_{\lambda} \zeta'_{[p,k]}, \tag{3.62}$$

$$\left\{ \frac{1}{n^2} \mathbf{L}_n(a, b) \right\}_n \sim_{\lambda} \zeta_{[p,k]}. \tag{3.63}$$

It can be shown that  $\kappa_{[p,k]}, \zeta_{[p,k]}, \zeta'_{[p,k]}$  are the *unique* non-decreasing functions defined on  $[0, 1]$  for which the asymptotic eigenvalue distributions (3.61)–(3.63) are satisfied.

**Remark 3.5** (Analytical predictions of the eigenvalue errors) Let  $\lambda_{j,n}, j = 1, \dots, n(p - k) + k - 1$ , be the numerical eigenvalues (i.e., the eigenvalues of  $\mathbf{L}_n(a, b)$ ) sorted, as always, in increasing order. In view of the eigenvalue distribution  $\left\{ \frac{1}{n^2} \mathbf{L}_n(a, b) \right\}_n \sim_{\lambda} \zeta_{[p,k]}$ , we can say that:

- for large values of  $n$ , the eigenvalues of  $\frac{1}{n^2} \mathbf{L}_n(a, b)$  (except possibly for a small number of outliers) are approximated by uniform samples over  $[0, 1]$  of  $\zeta_{[p,k]}$ ;
- for large values of  $n$ , the eigenvalues of  $\mathbf{L}_n(a, b)$  (except possibly for a small number of outliers) are approximated by uniform samples over  $[0, 1]$  of  $n^2 \zeta'_{[p,k]}$ .

Therefore, we propose the following procedure to compute the (asymptotic) analytical predictions of the eigenvalue errors

$$\frac{\lambda_{j,n}}{\lambda_j} - 1, \quad j = 1, \dots, n(p - k) + k - 1,$$

in the limit of mesh refinement (when  $n \rightarrow \infty$ ).

- Compute the uniform samples

$$\zeta_{[p,k]} \left( \frac{j}{n(p - k)} \right), \quad j = 1, \dots, n(p - k). \tag{3.64}$$

- Compute the asymptotic analytical predictions of the eigenvalue errors as follows:

$$\frac{\lambda_{j,n}}{\lambda_j} - 1 \approx \frac{n^2 \zeta_{[p,k]} \left( \frac{j}{n(p - k)} \right)}{\lambda_j} - 1, \quad j = 1, \dots, m, \tag{3.65}$$

where  $m := \min(n(p - k), n(p - k) + k - 1)$ .

In practical applications, since the exact eigenvalues  $\lambda_j$  are not available, we replace them in (3.65) by  $\lambda_{j,n'}$ , where  $n'$  is chosen so that  $n' \gg n$ . Moreover, if also  $\zeta_{[p,k]}$  is not

available, we replace it in (3.65) by  $\zeta_{r,[p,k]}$  with a large  $r$ . In (3.65) we are assuming that the eigenvalue errors corresponding to indices  $j$  exceeding  $n(p - k)$  have no analytical counterpart. Actually, the number of these “excluded” eigenvalue errors is only  $\max(0, k - 1) \leq p - 2$ , and can be neglected in the limit of mesh refinement  $n \rightarrow \infty$  (recall that (3.65) holds precisely in this limit).

**Remark 3.6** (How to find a good sampling grid) When using a naively chosen uniform grid such as (3.64), it might happen that the analytical predictions are not very accurate for small eigenvalues. This could be improved by taking a better sampling grid. The following procedure computes, at a reasonable cost, a good sampling grid yielding more accurate analytical predictions (in the same spirit as Remark 3.3).

- Compute the smallest  $\varsigma$  numerical eigenvalues  $\lambda_{j,n}, j = 1, \dots, \varsigma$ , with  $\varsigma$  being a very small number. This can be done by using a suitable numerical method (for example, the inverse subspace iteration method).
- Fix a large pair of values  $q, r \in \mathbb{N}$ , and compute the values  $n^2 \zeta_{r,[p,k]}(i/q)$  for  $i = 1, \dots, q$ . For each  $j = 1, \dots, \varsigma$ , choose the point  $\tau''_j$  of the grid  $\{i/q : i = 1, \dots, q\}$  which minimizes the distance  $|n^2 \zeta_{r,[p,k]}(\tau''_j) - \lambda_{j,n}|$ .
- Make a uniform sampling of  $\zeta_{r,[p,k]}$  from  $\tau''_{\varsigma}$  till the end of the interval  $[0, 1]$ . Here, we assume to sample  $\zeta_{r,[p,k]}$  over the uniform grid  $\{\tau''_{\varsigma}, \dots, \tau''_{n(p-k)}\}$ , where

$$\tau''_{\varsigma+j} := \tau''_{\varsigma} + j \frac{1 - \tau''_{\varsigma}}{n(p - k) - \varsigma}, \quad j = 1, \dots, n(p - k) - \varsigma.$$

The grid  $\{\tau''_1, \dots, \tau''_{n(p-k)}\}$  can be used to obtain analytical predictions for the eigenvalue errors. Of course, if  $\zeta_{[p,k]}$  is available, then the second and third steps of the above procedure should be performed with  $\zeta_{[p,k]}$  instead of  $\zeta_{r,[p,k]}$ .

### 3.3.1 $p$ -Degree $C^{p-1}$ B-Spline Discretization

When assuming the maximal smoothness  $k = p - 1$ , the relations (3.55)–(3.57) simplify to

$$\left\{ \frac{1}{n} \mathbf{K}_n(a) \right\}_n \sim_{\sigma, \lambda} a(x) f_p(\theta), \tag{3.66}$$

$$\left\{ n \mathbf{M}_n(b) \right\}_n \sim_{\sigma, \lambda} b(x) h_p(\theta), \tag{3.67}$$

$$\left\{ \frac{1}{n^2} \mathbf{L}_n(a, b) \right\}_n \sim_{\sigma, \lambda} \frac{a(x)}{b(x)} e_p(\theta), \tag{3.68}$$

where  $f_p := \mathbf{f}_{[p,p-1]}$ ,  $h_p := \mathbf{h}_{[p,p-1]}$ ,  $e_p := \mathbf{e}_{[p,p-1]}$  are the scalar functions in (2.52)–(2.54); see [11]. According to Remark 3.5, analytical predictions of the eigenvalue errors

can be expressed in terms of the rearranged version  $\zeta_{[p,p-1]}$  of the symbol  $\frac{a(x)}{b(x)}e_p(\theta)$ , as follows:

$$\frac{\lambda_{j,n}}{\lambda_j} - 1 \approx \frac{n^2 \zeta_{[p,p-1]}(\frac{\lambda_j}{n})}{\lambda_j} - 1, \quad j = 1, \dots, m,$$

where  $m := \min(n, n + p - 2)$ . Alternatively, taking into account Remark 3.6 with  $k = p - 1$ ,

$$\frac{\lambda_{j,n}}{\lambda_j} - 1 \approx \frac{n^2 \zeta_{[p,p-1]}(\tau_j'')}{\lambda_j} - 1, \quad j = 1, \dots, m.$$

For some numerical experiments we first focus on problem (3.1) with coefficients  $a(x) = 1 + x^2$  and  $b(x) = 1 - 0.5x$ . Figure 62 shows the comparison between the (approximate) analytical predictions  $n^2 \zeta_{r,[p,p-1]}(\tau_j'') / \lambda_{j,n'} - 1$ ,  $j = 1, \dots, n$ , and the (approximate) eigenvalue errors  $\lambda_{j,n} / \lambda_{j,n'} - 1$ ,  $j = 1, \dots, n + p - 2$ , for  $p = 2, 3, 4, 5$  and  $n = 200$ . The approximation parameters have been chosen as  $n' = 1500$ ,  $r = 10000$ ,  $q = 1000000$  and  $\zeta = 1$ . Moreover, the eigenvalues  $\lambda_{j,n'}$  have been taken from the matrix  $L_{n'}(a, b)$  corresponding to the maximal degree  $p = 5$ . This was done because, as it is clear from Fig. 62, the discretization with  $p = 5$  is the most accurate, and hence it provides the best approximations  $\lambda_{j,n'}$  to the exact eigenvalues  $\lambda_j$ , at least until  $j$  is not too large. We see from the figure that the eigenvalue errors match the analytical predictions, except at the end for  $p \geq 3$ . This mismatch is due to the presence of a few outliers at the end of the numerical spectra. Note, however, that the eigenvalue errors corresponding to the outliers actually do not have a corresponding analytical prediction as the blue line of the analytical predictions stops before the outliers. Indeed, the total number of analytical predictions is  $n$ , while the total number of eigenvalue errors is  $n + p - 2$ , so the last  $p - 2$  eigenvalue errors do not have a corresponding analytical prediction (see Remark 3.5). The precomputation of the smallest eigenvalue ( $\zeta = 1$ ) helps again circumvent the numerical instability at the small frequencies.

**Example 3.1** (Steel tapered rod with linearly varying cross-sectional area) Consider problem (3.1) with coefficients  $a(x) = 2.1 \cdot 10^9 + 1.05 \cdot 10^9 x$  and  $b(x) = 80 + 40x$ . This corresponds to the model of a steel tapered rod whose cross-sectional area varies linearly according to the equation  $A(x) = 0.01 + 0.005x$  (m<sup>2</sup>). Indeed, taking into account that the Young elasticity modulus and the density of the steel are, respectively,  $E = 210 \cdot 10^9$  Pa and  $\rho = 8000$  kg/m<sup>3</sup>, the squares of the natural frequencies  $\lambda_j$  and the normal modes  $u_j$  associated with the longitudinal vibrations of the rod are the solutions of the eigenvalue problem (3.1) with  $a(x) = E \cdot A(x) = 2.1 \cdot 10^9 + 1.05 \cdot 10^9 x$  and  $b(x) = \rho A(x) = 80 + 40x$ , as above.

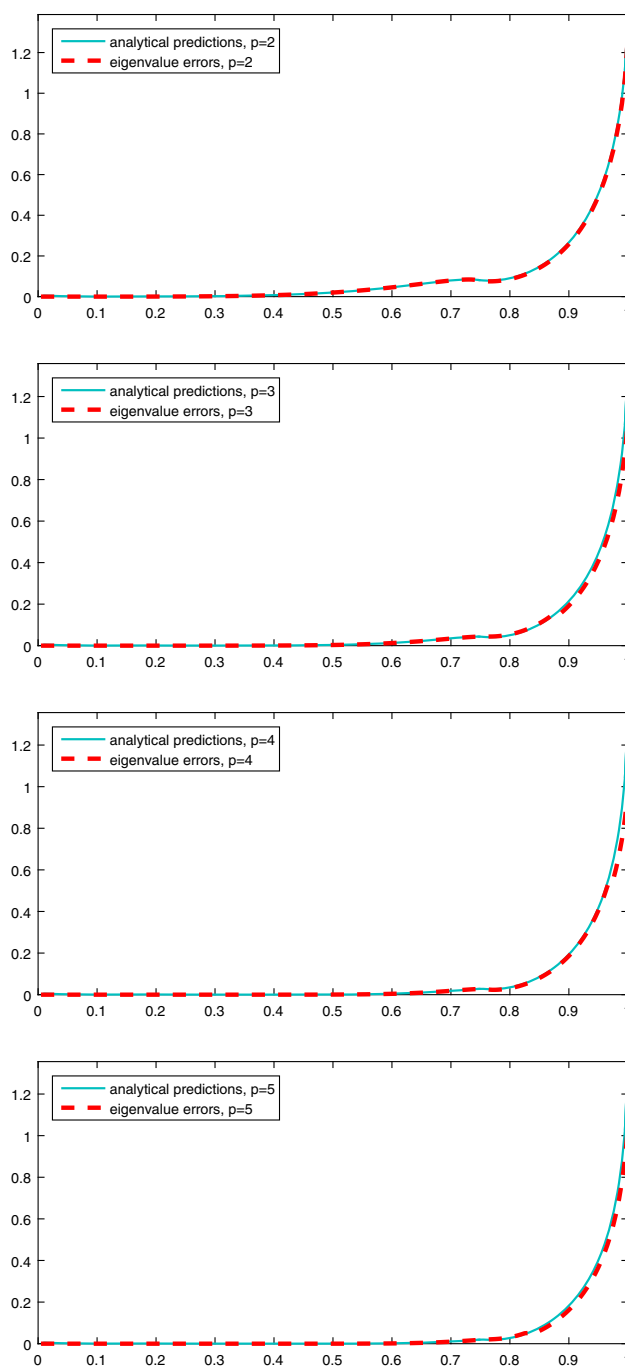


**Fig. 62**  $p$ -degree  $C^{p-1}$  B-spline discretization for  $p = 2, 3, 4, 5$  with  $a(x) = 1 + x^2$  and  $b(x) = 1 - 0.5x$ : analytical predictions  $n^2 \zeta_{r,[p,p-1]}(\tau_j'') / \lambda_{j,n'} - 1$  and eigenvalue errors  $\lambda_{j,n} / \lambda_{j,n'} - 1$  versus  $\tau_j''$ ,  $j = 1, \dots, N_n$  ( $N_n = n + p - 2 \approx 200$ ,  $n = 200$ ,  $n' = 1500$ ,  $r = 10000$ ,  $q = 1000000$ ,  $\zeta = 1$ )

Figure 63 shows the comparison between the (approximate) analytical predictions  $n^2 \zeta_{[p,p-1]}(\tau_j'') / \lambda_{j,n'} - 1$ ,  $j = 1, \dots, n$ , and the (approximate) eigenvalue errors  $\lambda_{j,n} / \lambda_{j,n'} - 1$ ,  $j = 1, \dots, n + p - 2$ , for  $p = 2, 3, 4, 5$  and

$n = 200$ , corresponding to the problem described in Example 3.1. Note that in this case the symbol in (3.68) becomes

$$\frac{a(x)}{b(x)} e_p(\theta) = 26250000 e_p(\theta),$$

i.e., it is just a scaled version of the symbol  $e_p(\theta)$  obtained in the constant-coefficient case.

Its rearranged version is explicitly given by<sup>4</sup>

$$\zeta_{[p,p-1]}(\tau) = 26250000 e_p(\pi\tau), \quad \tau \in [0, 1].$$

The approximation parameters have been chosen as  $n' = 1500$ ,  $q = 1000000$  and  $\varsigma = 1$ . The eigenvalues  $\lambda_{j,n'}$  have been taken from the matrix  $\mathbf{L}_{n'}(a, b)$  corresponding to the maximal degree  $p = 5$ , because the discretization with  $p = 5$  is the most accurate. We see from Fig. 63 that the eigenvalue errors match the analytical predictions, except at the end for  $p \geq 3$  due to the outliers. The precomputation of the smallest eigenvalue helps again circumvent the numerical instability at the small frequencies.

### 3.3.2 $p$ -Degree $C^0$ B-Spline Discretization

When assuming the minimal smoothness  $k = 0$ , the relations (3.55)–(3.57) become

$$\left\{ \frac{1}{n} \mathbf{K}_n(a) \right\}_n \sim_{\sigma, \lambda} a(x) \mathbf{f}_{[p,0]}(\theta), \tag{3.69}$$

$$\left\{ n \mathbf{M}_n(b) \right\}_n \sim_{\sigma, \lambda} b(x) \mathbf{h}_{[p,0]}(\theta), \tag{3.70}$$

$$\left\{ \frac{1}{n^2} \mathbf{L}_n(a, b) \right\}_n \sim_{\sigma, \lambda} \frac{a(x)}{b(x)} \mathbf{e}_{[p,0]}(\theta), \tag{3.71}$$

where  $\mathbf{f}_{[p,0]}$ ,  $\mathbf{h}_{[p,0]}$ ,  $\mathbf{e}_{[p,0]}$  are the  $p \times p$  matrix-valued functions in (2.69)–(2.71). According to Remark 3.5, analytical predictions of the eigenvalue errors can be expressed in terms of the rearranged version  $\zeta_{[p,0]}$  of the symbol  $\frac{a(x)}{b(x)} \mathbf{e}_{[p,0]}$ , as follows:

$$\frac{\lambda_{j,n}}{\lambda_j} - 1 \approx \frac{n^2 \zeta_{[p,0]} \left( \frac{j}{np} \right)}{\lambda_j} - 1, \quad j = 1, \dots, np - 1.$$

<sup>4</sup> To see this, recall that  $e_p(\theta)$  is increasing on  $[0, \pi]$  and  $\zeta_{[p,p-1]}$  is the unique non-decreasing function on  $[0, 1]$  satisfying  $\left\{ \frac{1}{n^2} \mathbf{L}_n(a, b) \right\}_n \sim_{\lambda} \zeta_{[p,p-1]}$ . Take also into account that, for every constant  $C > 0$ , the asymptotic eigenvalue distribution  $\{\mathbf{X}_n\}_n \sim_{\lambda} g$ , with  $g: [\alpha, \beta] \rightarrow \mathbb{R}$ , is equivalent to the asymptotic eigenvalue distribution  $\{\mathbf{X}_n\}_n \sim_{\lambda} \tilde{g}$ , where  $\tilde{g}: [C\alpha, C\beta] \rightarrow \mathbb{R}$  is defined as  $\tilde{g}(\tau) = g(C^{-1}\tau)$ . This result is intuitively clear in the light of the meaning of the distribution relations  $\{\mathbf{X}_n\}_n \sim_{\lambda} g$  and  $\{\mathbf{X}_n\}_n \sim_{\lambda} \tilde{g}$ ; a formal proof can be given using the precise definitions reported in Appendix.

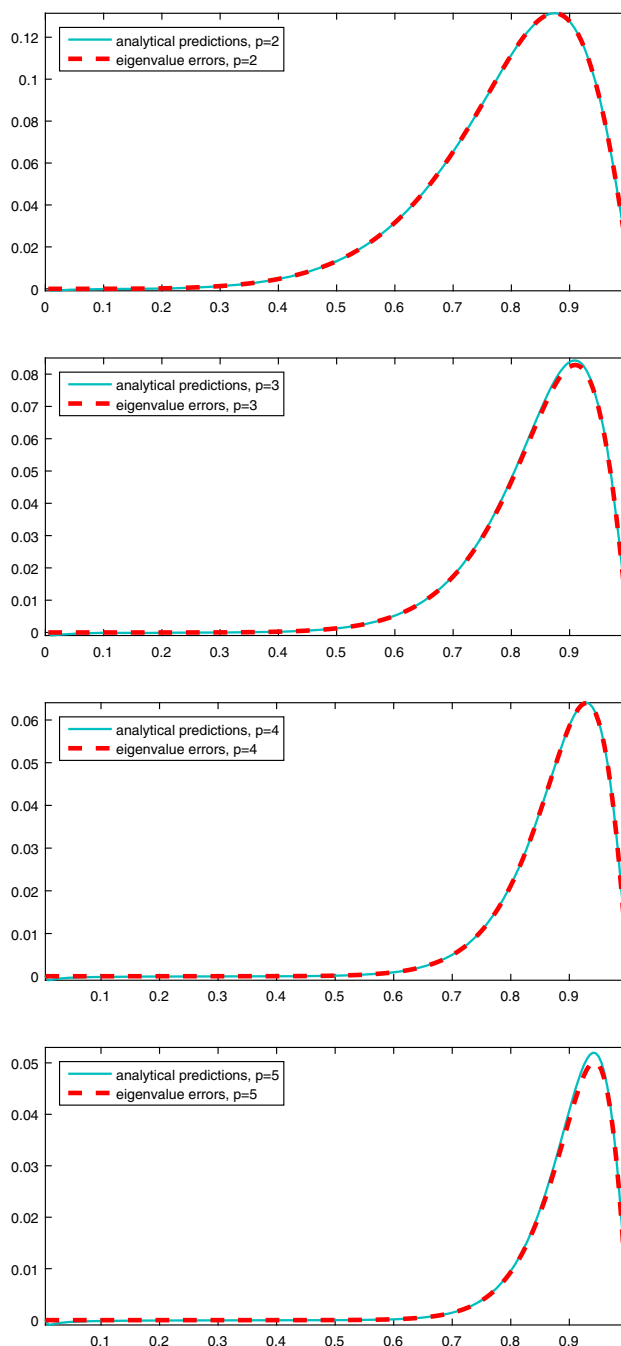


**Fig. 63**  $p$ -degree  $C^{p-1}$  B-spline discretization for  $p = 2, 3, 4, 5$  with  $a(x) = 2.1 \cdot 10^9 + 1.05 \cdot 10^9 x$  and  $b(x) = 80 + 40x$ : analytical predictions  $n^2 \zeta_{[p,p-1]}(\tau_j'')/\lambda_{j,n'} - 1$  and eigenvalue errors  $\lambda_{j,n}/\lambda_{j,n'} - 1$  versus  $\tau_j''$ ,  $j = 1, \dots, N_n$  ( $N_n = n + p - 2 \approx 200$ ,  $n = 200$ ,  $n' = 1500$ ,  $q = 1000000$ ,  $\varsigma = 1$ )

Alternatively, taking into account Remark 3.6 with  $k = 0$ ,

$$\frac{\lambda_{j,n}}{\lambda_j} - 1 \approx \frac{n^2 \zeta_{[p,0]} \left( \tau_j'' \right)}{\lambda_j} - 1, \quad j = 1, \dots, np - 1.$$

For some numerical experiments we first focus on problem (3.1) with coefficients  $a(x) = 1 + x^2$  and  $b(x) = 1 - 0.5x$ . Figure 64 shows the comparison between the (approximate) analytical predictions  $n^2 \zeta_{r,[p,0]}(\tau_j'') / \lambda_{j,n'} - 1$ ,  $j = 1, \dots, np$ , and the (approximate) eigenvalue errors  $\lambda_{j,n} / \lambda_{j,n'} - 1$ ,  $j = 1, \dots, np - 1$ , for  $p = 2, 3, 4, 5$  and  $n = 100, 67, 50, 40$ . The choice of the pairs  $(p, n) = (2, 100), (3, 67), (4, 50), (5, 40)$  was made to ensure that the total number of degrees of freedom  $N_n = np - 1$  remains approximately equal to 200, like in Fig. 62. This allows for a comparison between Figs. 62 and 64. The approximation parameters have been chosen as  $n' = 1500, r = 10000, q = 1000000$  and  $\zeta = 1$ . We see from Fig. 64 that the eigenvalue errors match the analytical predictions.

Consider now again the model of a steel tapered rod with linearly varying cross-sectional area from Example 3.1. Figure 65 shows the comparison between the (approximate) analytical predictions  $n^2 \zeta_{r,[p,0]}(\tau_j'') / \lambda_{j,n'} - 1$ ,  $j = 1, \dots, np$ , and the (approximate) eigenvalue errors  $\lambda_{j,n} / \lambda_{j,n'} - 1$ ,  $j = 1, \dots, np - 1$ , for  $p = 2, 3, 4, 5$  and  $n = 100, 67, 50, 40$ , corresponding to this problem. Note that in this case the symbol in (3.71) becomes

$$\frac{a(x)}{b(x)} \mathbf{e}_{[p,0]}(\theta) = 26250000 \mathbf{e}_{[p,0]}(\theta),$$

i.e., it is just a scaled version of the symbol  $\mathbf{e}_{[p,0]}(\theta)$  obtained in the constant-coefficient case. The choice of the pairs  $(p, n) = (2, 100), (3, 67), (4, 50), (5, 40)$  was made to ensure that the total number of degrees of freedom  $N_n = np - 1$  remains approximately equal to 200, like in Fig. 63. The approximation parameters have again been chosen as  $n' = 1500, r = 10000, q = 1000000$  and  $\zeta = 1$ . We see from Fig. 65 that the eigenvalue errors match the analytical predictions.

### 3.4 Isogeometric Galerkin Discretization of Variable-Coefficient Eigenvalue Problems

In the isogeometric Galerkin method, the physical domain  $[0, 1]$  in problem (3.1) is described by a global geometry map  $G : [0, 1] \rightarrow [0, 1]$ . We assume that  $G$  is invertible,  $C^1$  smooth, and satisfies  $G(0) = 0$  and  $G(1) = 1$ . We fix a set of basis functions  $\{\varphi_1, \dots, \varphi_{N_n}\}$  defined on the reference (parametric) domain  $[0, 1]$  and vanishing on the boundary. Then, we consider the basis functions

$$\psi_i(x) := \varphi_i(G^{-1}(x)) = \varphi_i(t), \quad x = G(t), \quad i = 1, \dots, N_n,$$

and we define the approximation space  $\mathcal{W}_n := \text{span}(\psi_1, \dots, \psi_{N_n}) \subset H_0^1(\Omega)$ . Using this space, we arrive at the following generalized matrix eigenvalue problem

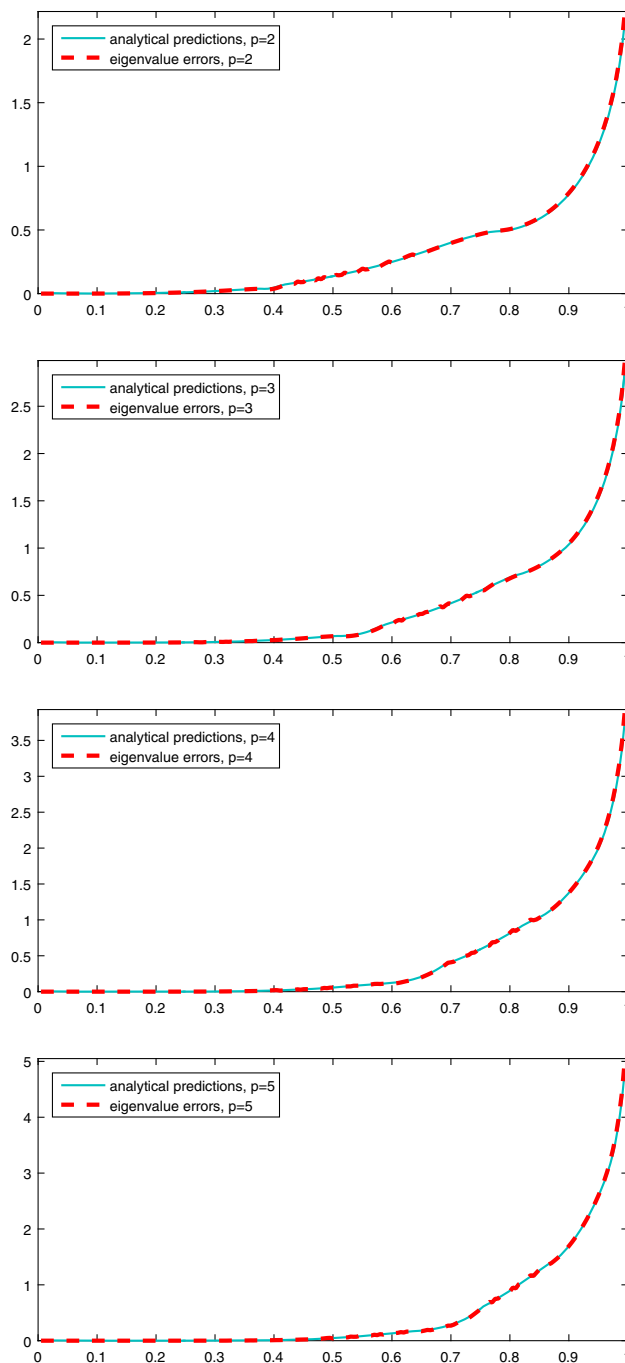
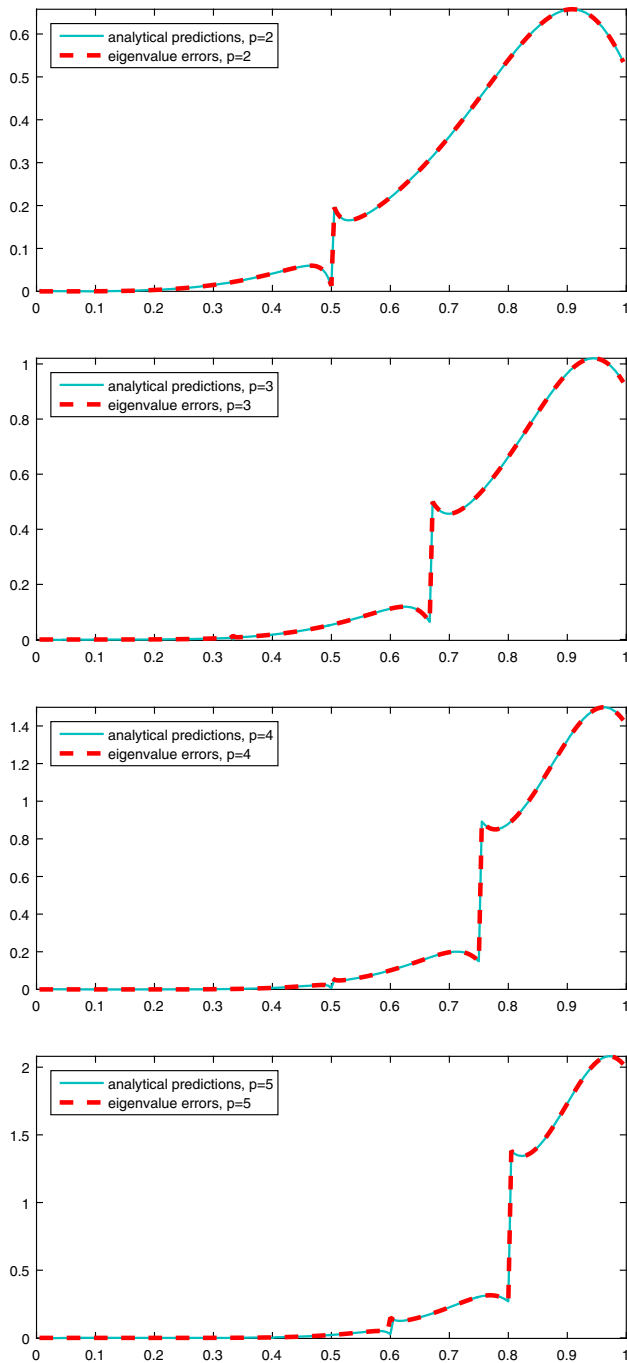


Fig. 64  $p$ -degree  $C^0$  B-spline discretization for  $p = 2, 3, 4, 5$  with  $a(x) = 1 + x^2$  and  $b(x) = 1 - 0.5x$ : analytical predictions  $n^2 \zeta_{r,[p,0]}(\tau_j'') / \lambda_{j,n'} - 1$  and eigenvalue errors  $\lambda_{j,n} / \lambda_{j,n'} - 1$  versus  $\tau_j''$ ,  $j = 1, \dots, N_n$  ( $N_n = np - 1 \approx 200$ ,  $n = 100, 67, 50, 40$ ,  $n' = 1500$ ,  $r = 10000$ ,  $q = 1000000$ ,  $\zeta = 1$ )

$$\mathbf{K}_n(a, G) \mathbf{u}_{j,n} = \lambda_{j,n} \mathbf{M}_n(b, G) \mathbf{u}_{j,n}, \tag{3.72}$$

where  $\mathbf{u}_{j,n}$  is the coefficient vector with respect to  $\{\psi_1, \dots, \psi_{N_n}\}$ ,



**Fig. 65**  $p$ -degree  $C^0$  B-spline discretization for  $p = 2, 3, 4, 5$  with  $a(x) = 2.1 \cdot 10^9 + 1.05 \cdot 10^9 x$  and  $b(x) = 80 + 40x$ : analytical predictions  $n^2 \zeta_{r,[p,0]}(\tau_j'') / \lambda_{j,n'} - 1$  and eigenvalue errors  $\lambda_{j,n} / \lambda_{j,n'} - 1$  versus  $\tau_j''$ ,  $j = 1, \dots, N_n$  ( $N_n = np - 1 \approx 200$ ,  $n = 100, 67, 50, 40$ ,  $n' = 1500$ ,  $r = 10000$ ,  $q = 1000000$ ,  $\zeta = 1$ )

$$\begin{aligned} \mathbf{K}_n(a, G) &:= [a(\psi_j, \psi_i)]_{i,j=1}^{N_n} = \left[ \int_0^1 a(x) \psi_j'(x) \psi_i'(x) dx \right]_{i,j=1}^{N_n} \\ &= \left[ \int_0^1 \frac{a(G(t))}{|G'(t)|} \varphi_j'(t) \varphi_i'(t) dt \right]_{i,j=1}^{N_n}, \end{aligned} \tag{3.73}$$

and

$$\begin{aligned} \mathbf{M}_n(b, G) &:= [(b \psi_j, \psi_i)]_{i,j=1}^{N_n} = \left[ \int_0^1 b(x) \psi_j(x) \psi_i(x) dx \right]_{i,j=1}^{N_n} \\ &= \left[ \int_0^1 b(G(t)) |G'(t)| \varphi_j(t) \varphi_i(t) dt \right]_{i,j=1}^{N_n}. \end{aligned} \tag{3.74}$$

The matrices  $\mathbf{K}_n(a, G)$  and  $\mathbf{M}_n(b, G)$  are, respectively, the stiffness and mass matrices. Due to our assumption that  $a, b > 0$  on  $(0, 1)$ , both  $\mathbf{K}_n(a, G)$  and  $\mathbf{M}_n(b, G)$  are always symmetric positive definite, regardless of the chosen basis functions  $\varphi_1, \dots, \varphi_{N_n}$  and the map  $G$ . Moreover, it is clear from (3.72) that the numerical eigenvalues  $\lambda_{j,n}$ ,  $j = 1, \dots, N_n$ , are just the eigenvalues of the matrix

$$\mathbf{L}_n(a, b, G) := (\mathbf{M}_n(b, G))^{-1} \mathbf{K}_n(a, G). \tag{3.75}$$

By comparing (3.4)–(3.6) and (3.73)–(3.75), we see that

$$\begin{aligned} \mathbf{K}_n(a, G) &= \mathbf{K}_n(a_G), & \mathbf{M}_n(b, G) &= \mathbf{M}_n(b_G), \\ \mathbf{L}_n(a, b, G) &= \mathbf{L}_n(a_G, b_G), \end{aligned}$$

where

$$a_G(t) := \frac{a(G(t))}{|G'(t)|}, \quad b_G(t) := b(G(t)) |G'(t)|.$$

Therefore, all the results obtained in the previous sections for the matrices  $\mathbf{K}_n(a)$ ,  $\mathbf{M}_n(b)$ ,  $\mathbf{L}_n(a, b)$  also apply to the matrices  $\mathbf{K}_n(a, G)$ ,  $\mathbf{M}_n(b, G)$ ,  $\mathbf{L}_n(a, b, G)$ ; it suffices to replace  $a$  and  $b$  with  $a_G$  and  $b_G$ . In particular, if  $a_G, b_G \in C([0, 1])$  and the basis functions  $\varphi_1, \dots, \varphi_{N_n}$  are chosen as the  $p$ -degree  $C^k$  B-splines  $B_{2,[p,k]}, \dots, B_{n(p-k)+k,[p,k]}$ , then

$$\begin{aligned} \mathbf{K}_n(a, G) &= \mathbf{K}_n(a_G) \\ &= \left[ \int_0^1 \frac{a(G(t))}{|G'(t)|} B_{j+1,[p,k]}'(t) B_{i+1,[p,k]}'(t) dt \right]_{i,j=1}^{n(p-k)+k-1}, \end{aligned} \tag{3.76}$$

and

$$\begin{aligned} \mathbf{M}_n(a, G) &= \mathbf{M}_n(b_G) \\ &= \left[ \int_0^1 b(G(t)) |G'(t)| B_{j+1,[p,k]}(t) B_{i+1,[p,k]}(t) dt \right]_{i,j=1}^{n(p-k)+k-1}. \end{aligned} \tag{3.77}$$

From (3.52)–(3.57) we get

$$\left\{ \frac{1}{n} \mathbf{K}_n(a, G) \right\}_n \sim_{\text{GLT}} \frac{a(G(t))}{|G'(t)|} \mathbf{f}_{[p,k]}(\theta), \tag{3.78}$$

$$\left\{ n \mathbf{M}_n(b, G) \right\}_n \sim_{\text{GLT}} b(G(t)) |G'(t)| \mathbf{h}_{[p,k]}(\theta), \tag{3.79}$$

$$\left\{ \frac{1}{n^2} \mathbf{L}_n(a, b, G) \right\}_n \sim_{\text{GLT}} \frac{a(G(t))}{b(G(t)) |G'(t)|^2} \mathbf{e}_{[p,k]}(\theta), \tag{3.80}$$

and as a consequence,

$$\left\{ \frac{1}{n} \mathbf{K}_n(a, G) \right\}_n \sim_{\sigma, \lambda} \frac{a(G(t))}{|G'(t)|} \mathbf{f}_{[p,k]}(\theta), \tag{3.81}$$

$$\left\{ n \mathbf{M}_n(b, G) \right\}_n \sim_{\sigma, \lambda} b(G(t)) |G'(t)| \mathbf{h}_{[p,k]}(\theta), \tag{3.82}$$

$$\left\{ \frac{1}{n^2} \mathbf{L}_n(a, b, G) \right\}_n \sim_{\sigma, \lambda} \frac{a(G(t))}{b(G(t)) |G'(t)|^2} \mathbf{e}_{[p,k]}(\theta). \tag{3.83}$$

Moreover, from (3.61)–(3.63) we obtain

$$\left\{ \frac{1}{n} \mathbf{K}_n(a, G) \right\}_n \sim_{\lambda} \kappa_{[p,k]}, \tag{3.84}$$

$$\left\{ n \mathbf{M}_n(b, G) \right\}_n \sim_{\lambda} \xi_{[p,k]}, \tag{3.85}$$

$$\left\{ \frac{1}{n^2} \mathbf{L}_n(a, b, G) \right\}_n \sim_{\lambda} \zeta_{[p,k]}, \tag{3.86}$$

where  $\kappa_{[p,k]}$ ,  $\xi_{[p,k]}$ ,  $\zeta_{[p,k]}$  are the rearranged versions of  $\frac{a(G(t))}{|G'(t)|} \mathbf{f}_{[p,k]}(\theta)$ ,  $b(G(t)) |G'(t)| \mathbf{h}_{[p,k]}(\theta)$ ,  $\frac{a(G(t))}{b(G(t)) |G'(t)|^2} \mathbf{e}_{[p,k]}(\theta)$ , respectively. Analytical predictions of the eigenvalue errors can be obtained through the procedure described in Remark 3.5:

$$\frac{\lambda_{j,n}}{\lambda_j} - 1 \approx \frac{n^2 \zeta_{[p,k]} \left( \frac{j}{n(p-k)} \right)}{\lambda_j} - 1, \quad j = 1, \dots, m,$$

where  $m := \min(n(p-k), n(p-k) + k - 1)$ . Alternatively, taking into account Remark 3.6,

$$\frac{\lambda_{j,n}}{\lambda_j} - 1 \approx \frac{n^2 \zeta_{[p,k]}(\tau_j'')}{\lambda_j} - 1, \quad j = 1, \dots, m.$$

Note that, in the above spectral analysis, the considered geometry map  $G$  can be given in any representation and is not confined to the B-spline form as prescribed by the isogeometric analysis paradigm.

Consider now the model of a steel tapered rod with linearly varying cross-sectional area from Example 3.1. Fix  $p = 4$  and the geometry map

$$G : [0, 1] \rightarrow [0, 1], \quad G(t) := \frac{1.1t}{0.1+t}.$$

The graph of the geometry map is depicted in Fig. 66. In Fig. 67 we compare the (approximate) analytical predictions  $n^2 \zeta_{r,[4,k]}(\tau_j'') / \lambda_{j,n'} - 1$ ,  $j = 1, \dots, n(4-k)$ , and the

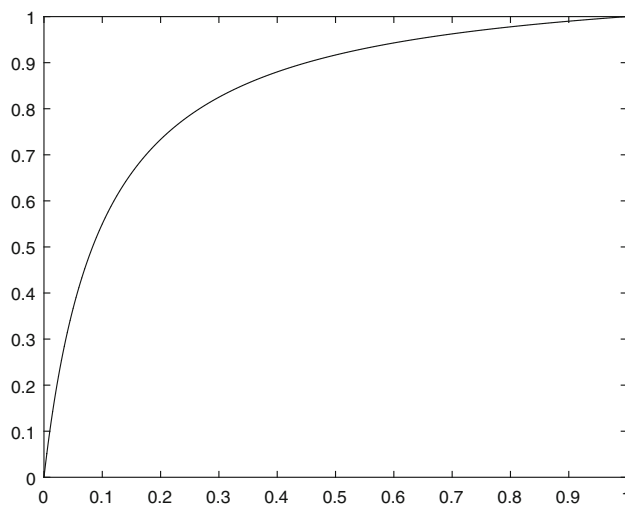
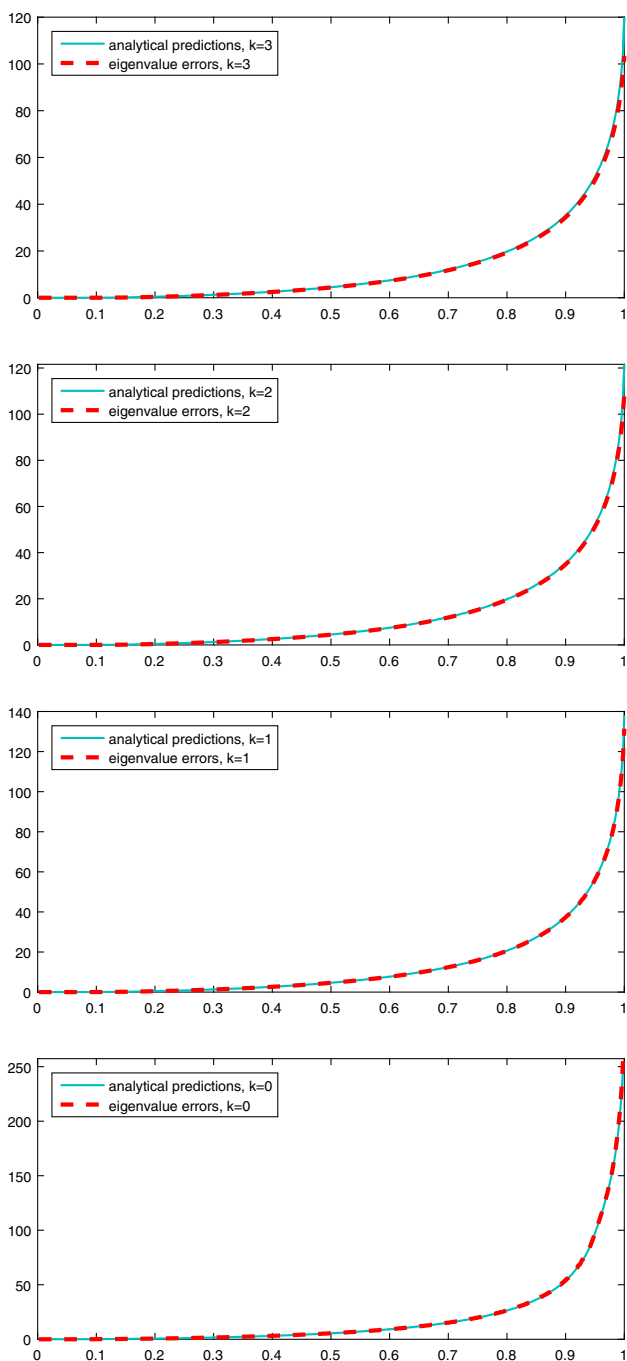


Fig. 66 Graph of the geometry map  $G(t) = \frac{1.1t}{0.1+t}$

(approximate) eigenvalue errors  $\lambda_{j,n} / \lambda_{j,n'} - 1$ ,  $j = 1, \dots, n(4-k) + k - 1$ , for  $k = 3, 2, 1, 0$  and  $n = 500, 250, 167, 125$ . The choice of the pairs  $(k, n) = (3, 500), (2, 250), (1, 167), (0, 125)$  was made in order to ensure that the total number of degrees of freedom  $N_n = n(4-k) + k - 1$  remains approximately equal to 500 in all cases. The approximation parameters have been chosen as  $n' = 1500$ ,  $r = 10000$ ,  $q = 1000000$  and  $\varsigma = 1$ . The eigenvalues  $\lambda_{j,n'}$  have been taken from the matrix  $\mathbf{L}_{n'}(a, b)$  corresponding to the degree  $p = 5$  and  $k = 4$ . We see from Fig. 67 that the eigenvalue errors match the analytical predictions. We also see that the large eigenvalues are badly approximated in all cases. This is due to the effect of the geometry map  $G$  which highly “deforms” the domain  $[0, 1]$ . In particular, the minimum of  $G'(t) = 0.1 / (0.1 + t)^2$  is achieved at  $t = 1$  and equals  $G'(1) \approx 0.0826$ . Since  $1 / |G'(1)|^2 \approx 146$  and  $|G'(t)|^2$  appears at the denominator of the symbol in (3.83), it is no surprise to see such bad approximations of large eigenvalues. Note that the maximum of both the analytical predictions and eigenvalue errors for  $k = 3, 2, 1$  is between 120 and 140, which is relatively close to 146.

### 4 Conclusions and Future Directions

Spectral analysis provides valuable insights into the behavior of discrete approximations to differential equations. Recent progress in symbol-based spectral analysis has extended the scope of spectral analysis, but these advances are highly technical and have so far been confined to the mathematics literature. This paper is an effort to bring these ideas to the attention of the computational engineering community. To this end, we have presented an



**Fig. 67** Isogeometric quartic  $C^k$  B-spline discretization for  $k = 3, 2, 1, 0$  with  $a(x) = 2.1 \cdot 10^9 + 1.05 \cdot 10^9 x$ ,  $b(x) = 80 + 40x$  and  $G(t) = \frac{1+t}{0.1+t}$ . analytical predictions  $n^2 \zeta_{r,[4,k]}(\tau_j'') / \lambda_{j,n'} - 1$  and eigenvalue errors  $\lambda_{j,n} / \lambda_{j,n'} - 1$  versus  $\tau_j''$ ,  $j = 1, \dots, N_n$  ( $N_n = n(4 - k) + k - 1 \approx 500$ ,  $n = 500, 250, 167, 125$ ,  $n' = 1500$ ,  $r = 10000$ ,  $q = 1000000$ ,  $\varsigma = 1$ )

example-based exposition and review of symbol-based spectral analysis. In particular, we have analyzed constant- and variable-coefficient one-dimensional eigenvalue problems discretized through the (isogeometric) Galerkin method based on B-splines of degree  $p$  and smoothness  $C^k$ ,

$0 \leq k \leq p - 1$ . For each of these problems, we have illustrated the procedure to compute the symbol of the related discretization matrices  $\mathbf{L}_n$ . The symbol describes the asymptotic singular value and eigenvalue distribution of the sequence  $\{\mathbf{L}_n\}_n$  and has allowed us:

- to formulate analytical predictions for the eigenvalue errors, so as to recover and extend some analytical spectral results of [5, 20, 21, 23];
- to predict the existence, for the one-dimensional Laplacian eigenvalue problem, of  $p - k$  spectral branches (one “acoustical” and  $p - k - 1$  “optical”), to provide explicit and implicit analytical expressions for these branches, and to quantify the divergence to infinity with respect to  $p$  of the largest optical branch in the case of minimal smoothness  $k = 0$  (the classical FEA case).

We end by outlining some extensions that are interesting directions of further investigation.

### 4.1 Extension to the Case of $L^1$ Coefficients

The GLT relations (3.11)–(3.13) have been proved under the assumption that the coefficients  $a$  and  $b$  are continuous in (3.1). Through the theory of GLT sequences one can show that (3.11)–(3.13) (and hence also (3.14)–(3.16)) continue to hold under the weaker assumption that  $a, b \in L^1([0, 1])$ .

Let us sketch the argument for proving (3.11)–(3.13) in the  $L^1$  case. First, we note that (3.12) is proved in the same way as (3.11). Second, we note that (3.13) follows from (3.11)–(3.12) and the theory of GLT sequences (any algebraic combination of GLT sequences is again a GLT sequence with its symbol given by the same algebraic combination of the symbols). It is therefore sufficient to prove (3.11) for  $a \in L^1([0, 1])$ . Let  $a \in L^1([0, 1])$  and take any sequence of continuous functions  $a_m$  such that  $a_m$  converges to  $a$  in  $L^1([0, 1])$ . Since  $a_m$  is continuous, we have  $\{\frac{1}{n} \mathbf{K}_n(a_m)\}_n \sim_{\text{GLT}} a_m(x) f(\theta)$ . Moreover, using the fact that  $a_m \rightarrow a$  in  $L^1([0, 1])$ ,

- it is clear from Fubini’s theorem that  $a_m(x) f(\theta)$  converges to  $a(x) f(\theta)$  in  $L^1([0, 1] \times [-\pi, \pi])$ ,
- it can be shown that the sequence  $\{\frac{1}{n} \mathbf{K}_n(a_m)\}_n$  converges to  $\{\frac{1}{n} \mathbf{K}_n(a)\}_n$  in a suitable sense (the sense of the “approximating classes of sequences”; see [3, Section 2]).

This is enough to conclude that (3.11) holds for  $a \in L^1([0, 1])$ . A similar argument can be used for higher degrees as well. For a detailed mathematical presentation of the argument outlined here, we refer the reader to [3, Section 4] and also [9].

Despite this theoretical argument, we have observed a more severe failure of the small eigenvalue prediction in the  $L^1$  coefficient case than in the continuous coefficient case. The proposed fix in Remark 3.6 does not seem to work properly anymore when dealing with discontinuous coefficients. This requires further investigation.

## 4.2 Improving the Analytical Predictions

According to Remarks 3.5 and 3.6, we rely solely on uniform samplings to compute the analytical predictions of the eigenvalue errors, in particular, to approximate the rearranged version of the symbol (parameter  $r$ ) and to set up the sampling grid (parameter  $q$ ). However, very dense samplings (high values of  $r$  and  $q$ ) might be required to get a high accuracy. This could be avoided by using non-uniform samplings so that the total number of samplings can be lowered. Furthermore, it might be interesting to consider an interpolation–extrapolation procedure, in the spirit of the works [7, 8], to make better analytical predictions (especially for the small eigenvalues).

## 4.3 Other Discretizations and Eigenvalue Problems

The symbol-based analysis carried out in this paper can be extended to isogeometric collocation methods and to the multidimensional setting. Toward these extensions, some work has already been done in [6, 11], where the symbols have been computed for the stiffness (and mass) matrices arising from the discretization of multidimensional variable-coefficient advection-diffusion-reaction problems through isogeometric collocation and Galerkin methods based on (tensor-product) B-splines of maximal smoothness. A collection of properties of these symbols can be found in [11, 12].

**Acknowledgements** The authors express their gratitude to Emanuele Corti for his invaluable informatics support and for his help with the numerical experiments. C. Garoni is a Marie-Curie fellow of INdAM (Istituto Nazionale di Alta Matematica) under grant agreement PCOFUND-GA-2012-600198. H. Speleers was partially supported by the Mission Sustainability Program of the University of Rome Tor Vergata through the project “IDEAS”, and by INdAM Finanziamenti Premiali through the project “SUNRISE”. S-E. Ekström was supported by the FMB – Swedish National Graduate School of Mathematics and Computing. A. Reali was partially supported by Fondazione Cariplo – Regione Lombardia through the project “Verso nuovi strumenti di simulazione super veloci ed accurati basati sull’analisi isogeometrica”, within the program RST – rafforzamento. S. Serra-Capizzano was supported in part by the Donation KAW 2013.0341 from the Knut & Alice Wallenberg Foundation in collaboration with the Royal Swedish Academy of Sciences. T.J.R. Hughes was partially supported by the Office of Naval Research (Grant Nos. N00014-17-1-2119, N00014-17-1-2039, and N00014-13-1-0500), and by the Army Research Office (Grant No.

W911NF-13-1-0220). C. Garoni, A. Reali, S. Serra-Capizzano, and H. Speleers are members of the INdAM Research group GNCS (Gruppo Nazionale per il Calcolo Scientifico).

## Compliance with Ethical Standards

**Conflict of interest** The authors declare that there is no conflict of interest.

## Appendix: Singular Value and Eigenvalue Distribution of a Sequence of Matrices

A sequence of matrices is any sequence of the form  $\{\mathbf{X}_n\}_n$ , where  $\mathbf{X}_n$  is a square matrix such that  $\text{size}(\mathbf{X}_n) \rightarrow \infty$  as  $n \rightarrow \infty$ . In this appendix we provide the precise definitions of asymptotic singular value and eigenvalue distributions for a given sequence of matrices. We also discuss the informal meaning behind these definitions.

Let  $\mu_d$  be the Lebesgue measure in  $\mathbb{R}^d$  and let  $C_c(\mathbb{C})$  be the space of continuous complex-valued functions with bounded support defined on  $\mathbb{C}$ . If  $\mathbf{X}$  is an  $m \times m$  matrix, the singular values and the eigenvalues of  $\mathbf{X}$  are denoted by  $\sigma_1(\mathbf{X}), \dots, \sigma_m(\mathbf{X})$  and  $\lambda_1(\mathbf{X}), \dots, \lambda_m(\mathbf{X})$ , respectively.

**Definition A.1** Let  $\{\mathbf{X}_n\}_n$  be a sequence of matrices, let  $N_n := \text{size}(\mathbf{X}_n)$ , and let  $g : D \subset \mathbb{R}^d \rightarrow \mathbb{C}$  be a measurable function defined on a set  $D$  with  $0 < \mu_d(D) < \infty$ .

- We say that  $\{\mathbf{X}_n\}_n$  has an (asymptotic) singular value distribution described by  $g$ , and we write  $\{\mathbf{X}_n\}_n \sim \sigma g$ , if

$$\begin{aligned} & \lim_{n \rightarrow \infty} \frac{1}{N_n} \sum_{i=1}^{N_n} F(\sigma_i(\mathbf{X}_n)) \\ &= \frac{1}{\mu_d(D)} \int_D F(|g(y_1, \dots, y_d)|) dy_1 \cdots dy_d, \quad \forall F \in C_c(\mathbb{C}). \end{aligned}$$

- We say that  $\{\mathbf{X}_n\}_n$  has an (asymptotic) eigenvalue distribution described by  $g$ , and we write  $\{\mathbf{X}_n\}_n \sim \lambda g$ , if

$$\begin{aligned} & \lim_{n \rightarrow \infty} \frac{1}{N_n} \sum_{i=1}^{N_n} F(\lambda_i(\mathbf{X}_n)) \\ &= \frac{1}{\mu_d(D)} \int_D F(g(y_1, \dots, y_d)) dy_1 \cdots dy_d, \quad \forall F \in C_c(\mathbb{C}). \end{aligned}$$

The informal meaning behind the eigenvalue distribution  $\{\mathbf{X}_n\}_n \sim \lambda g$  is the following: for all sufficiently large  $n$ , the eigenvalues of  $\mathbf{X}_n$  (except possibly for a small number of outliers)<sup>5</sup> are approximated by the samples of  $g$  over a uniform grid in  $D$  (the domain of  $g$ ). For example, if

<sup>5</sup> It can be shown that the number of outliers divided by the matrix size  $N_n$  converges to 0 as  $n \rightarrow \infty$ . Using Landau’s symbols, this is expressed by saying that the number of outliers is  $o(N_n)$ .

$d = 1$ ,  $N_n = n$  and  $D = [a, b]$ , then the eigenvalues of  $\mathbf{X}_n$  are approximately equal to

$$g\left(a + j\frac{b-a}{n}\right), \quad j = 1, \dots, n,$$

for  $n$  large enough. Likewise, if  $d = 2$ ,  $N_n = n^2$  and  $D = [a_1, b_1] \times [a_2, b_2]$ , then the eigenvalues of  $\mathbf{X}_n$  are approximately equal to

$$g\left(a_1 + j_1\frac{b_1-a_1}{n}, a_2 + j_2\frac{b_2-a_2}{n}\right), \quad j_1, j_2 = 1, \dots, n,$$

for  $n$  large enough. The informal meaning behind the singular value distribution  $\{\mathbf{X}_n\}_n \sim \sigma g$  is completely analogous: for all sufficiently large  $n$ , the singular values of  $\mathbf{X}_n$  (except possibly for  $o(N_n)$  outliers) are approximated by the samples of  $|g|$  over a uniform grid in the domain  $D$ .

**Remark A.1** (Rearrangement) Let  $g : D \subset \mathbb{R}^d \rightarrow \mathbb{R}$  and suppose that  $D$  is a rectangle in  $\mathbb{R}^d$ , say  $D := [\alpha_1, \beta_1] \times \dots \times [\alpha_d, \beta_d]$ . For each positive integer  $r$ , let  $\mathcal{G}_r$  be the uniform grid in  $D$  given by

$$\mathcal{G}_r := \left\{ \left( x_1 + \frac{i_1}{r}(\beta_1 - \alpha_1), \dots, x_d + \frac{i_d}{r}(\beta_d - \alpha_d) \right) : i_1, \dots, i_d = 1, \dots, r \right\}.$$

Compute the samples of  $g$  at the grid points  $(y_1, \dots, y_d) \in \mathcal{G}_r$ , sort them in increasing order and put them in a vector  $(q_1, q_2, \dots, q_{r^d})$ . Let  $\eta_r : [0, 1] \rightarrow \mathbb{R}$  be the piecewise linear non-decreasing function that interpolates the samples  $(q_0 := q_1, q_1, q_2, \dots, q_{r^d})$  over the nodes  $(0, \frac{1}{r^d}, \frac{2}{r^d}, \dots, 1)$ , i.e.,

$$\eta_r\left(\frac{\ell}{r^d}\right) := q_\ell, \quad \ell = 0, \dots, r^d.$$

Under certain conditions on  $g$ , which are normally satisfied in practice, the function  $\eta_r$  converges (a.e.) as  $r \rightarrow \infty$  to a non-decreasing function  $\eta : [0, 1] \rightarrow \mathbb{R}$ , which is referred to as the rearranged version of  $g$ . What is important about  $\eta$  in view of Definition A.1 is that

$$\int_D F(|g(y_1, \dots, y_d)|) dy_1 \dots dy_d = \int_0^1 F(|\eta(t)|) dt, \quad \forall F \in C_c(\mathbb{C}), \tag{A.1}$$

and

$$\int_D F(g(y_1, \dots, y_d)) dy_1 \dots dy_d = \int_0^1 F(\eta(t)) dt, \quad \forall F \in C_c(\mathbb{C}). \tag{A.2}$$

Therefore, if we have  $\{\mathbf{X}_n\}_n \sim \sigma g$  (resp.,  $\{\mathbf{X}_n\}_n \sim \lambda g$ ), then we also have  $\{\mathbf{X}_n\}_n \sim \sigma \eta$  (resp.,  $\{\mathbf{X}_n\}_n \sim \lambda \eta$ ). It is also important to point out that  $\eta$  is the unique non-decreasing

function defined on  $[0, 1]$  satisfying (A.2); see, e.g., [14, Exercise 3.1].

Definition A.1 addresses the case where the singular value and eigenvalue distributions of a sequence of matrices are described by a scalar function  $g$ . Definition A.2 deals with the case of a matrix-valued function. If  $\mathbf{g} : D \subset \mathbb{R}^d \rightarrow \mathbb{C}^{s \times s}$  is an  $s \times s$  matrix-valued function, we say that  $\mathbf{g}$  is measurable if its  $s^2$  components  $g_{ij} : D \rightarrow \mathbb{C}$ ,  $i, j = 1, \dots, s$ , are measurable.

**Definition A.2** Let  $\{\mathbf{X}_n\}_n$  be a sequence of matrices, let  $N_n := \text{size}(\mathbf{X}_n)$ , and let  $\mathbf{g} : D \subset \mathbb{R}^d \rightarrow \mathbb{C}^{s \times s}$  be a measurable  $s \times s$  matrix-valued function defined on a set  $D$  with  $0 < \mu_d(D) < \infty$ .

- We say that  $\{\mathbf{X}_n\}_n$  has an (asymptotic) singular value distribution described by  $\mathbf{g}$ , and we write  $\{\mathbf{X}_n\}_n \sim \sigma \mathbf{g}$ , if

$$\begin{aligned} & \lim_{n \rightarrow \infty} \frac{1}{N_n} \sum_{i=1}^{N_n} F(\sigma_i(\mathbf{X}_n)) \\ &= \frac{1}{\mu_d(D)} \int_D \frac{\sum_{i=1}^s F(\sigma_i(\mathbf{g}(y_1, \dots, y_d)))}{s} dy_1 \dots dy_d, \\ & \forall F \in C_c(\mathbb{C}), \end{aligned}$$

where  $\sigma_i(\mathbf{g}(y_1, \dots, y_d))$ ,  $i = 1, \dots, s$ , are the singular values of the  $s \times s$  matrix  $\mathbf{g}(y_1, \dots, y_d)$ .

- We say that  $\{\mathbf{X}_n\}_n$  has an (asymptotic) eigenvalue distribution described by  $\mathbf{g}$ , and we write  $\{\mathbf{X}_n\}_n \sim \lambda \mathbf{g}$ , if

$$\begin{aligned} & \lim_{n \rightarrow \infty} \frac{1}{N_n} \sum_{i=1}^{N_n} F(\lambda_i(\mathbf{X}_n)) \\ &= \frac{1}{\mu_d(D)} \int_D \frac{\sum_{i=1}^s F(\lambda_i(\mathbf{g}(y_1, \dots, y_d)))}{s} dy_1 \dots dy_d, \\ & \forall F \in C_c(\mathbb{C}), \end{aligned}$$

where  $\lambda_i(\mathbf{g}(y_1, \dots, y_d))$ ,  $i = 1, \dots, s$ , are the eigenvalues of the  $s \times s$  matrix  $\mathbf{g}(y_1, \dots, y_d)$ .

Note that Definition A.1 is a special case of Definition A.2 (set  $s = 1$  in Definition A.2 to obtain Definition A.1). The informal meaning behind the eigenvalue distribution  $\{\mathbf{X}_n\}_n \sim \lambda \mathbf{g}$  is the following: for all sufficiently large  $n$ , the eigenvalues of  $\mathbf{X}_n$  can be subdivided into  $s$  different subsets of approximately the same cardinality; and the eigenvalues belonging to the  $i$ -th subset (except possibly for  $o(N_n)$  outliers) are approximated by the samples of the  $i$ -th eigenvalue function  $\lambda_i(\mathbf{g}(y_1, \dots, y_d))$  over a uniform grid in  $D$  (the domain of  $\mathbf{g}$ ). For example, if  $d = 1$ ,  $N_n = ns$  and  $D = [a, b]$ , then the eigenvalues of  $\mathbf{X}_n$  are approximately equal to

$$\lambda_i\left(\mathbf{g}\left(a + j\frac{b-a}{n}\right)\right), \quad j = 1, \dots, n, \quad i = 1, \dots, s,$$

for  $n$  large enough. Likewise, if  $d = 2$ ,  $N_n = n^2s$  and  $D = [a_1, b_1] \times [a_2, b_2]$ , then the eigenvalues of  $\mathbf{X}_n$  are approximately equal to

$$\lambda_i \left( \mathbf{g} \left( a_1 + j_1 \frac{b_1 - a_1}{n}, a_2 + j_2 \frac{b_2 - a_2}{n} \right) \right),$$

$$j_1, j_2 = 1, \dots, n, \quad i = 1, \dots, s,$$

for  $n$  large enough. The informal meaning behind the singular value distribution  $\{\mathbf{X}_n\}_n \sim \sigma \mathbf{g}$  is completely analogous: for all sufficiently large  $n$ , the singular values of  $\mathbf{X}_n$  can be subdivided into  $s$  different subsets of approximately the same cardinality; and the singular values belonging to the  $i$ -th subset (except possibly for  $o(N_n)$  outliers) are approximated by the samples of the  $i$ -th singular value function  $\sigma_i(\mathbf{g}(y_1, \dots, y_d))$  over a uniform grid in the domain  $D$ .

**Remark A.2** (Rearrangement) Let  $\mathbf{g} : D \subset \mathbb{R}^d \rightarrow \mathbb{C}^{s \times s}$  and suppose that  $D$  is a rectangle in  $\mathbb{R}^d$ , say  $D := [\alpha_1, \beta_1] \times \dots \times [\alpha_d, \beta_d]$ . We also assume that the eigenvalues  $\lambda_1(\mathbf{g}(y_1, \dots, y_d)), \dots, \lambda_s(\mathbf{g}(y_1, \dots, y_d))$  are real for all  $(y_1, \dots, y_d) \in D$ . For each positive integer  $r$ , let  $\mathcal{G}_r$  be the uniform grid in  $D$  given by

$$\mathcal{G}_r := \left\{ \left( \alpha_1 + \frac{i_1}{r}(\beta_1 - \alpha_1), \dots, \alpha_d + \frac{i_d}{r}(\beta_d - \alpha_d) \right) : i_1, \dots, i_d = 1, \dots, r \right\}.$$

Compute the samples of the eigenvalue functions  $\lambda_1(\mathbf{g}(y_1, \dots, y_d)), \dots, \lambda_s(\mathbf{g}(y_1, \dots, y_d))$  at the points  $(y_1, \dots, y_d) \in \mathcal{G}_r$ , sort them in increasing order and put them in a vector  $(q_1, q_2, \dots, q_{sr^d})$ . Let  $\eta_r : [0, 1] \rightarrow \mathbb{R}$  be the piecewise linear non-decreasing function that interpolates the samples  $(q_0 := q_1, q_1, q_2, \dots, q_{sr^d})$  over the nodes  $(0, \frac{1}{sr^d}, \frac{2}{sr^d}, \dots, 1)$ , i.e.,

$$\eta_r \left( \frac{\ell}{sr^d} \right) := q_\ell, \quad \ell = 0, \dots, sr^d.$$

Under certain (normally satisfied) conditions on  $\mathbf{g}$ , the function  $\eta_r$  converges (a.e.) as  $r \rightarrow \infty$  to a non-decreasing function  $\eta : [0, 1] \rightarrow \mathbb{R}$ , which is referred to as the rearranged version of  $\mathbf{g}$ . What is important about  $\eta$  in view of Definition A.2 is that

$$\int_D \frac{\sum_{i=1}^s F(\lambda_i(\mathbf{g}(y_1, \dots, y_d)))}{s} dy_1 \dots dy_d$$

$$= \int_0^1 F(\eta(t)) dt, \quad \forall F \in C_c(\mathbb{C}). \tag{A.3}$$

Therefore, if we have  $\{\mathbf{X}_n\}_n \sim \lambda \mathbf{g}$ , then we also have  $\{\mathbf{X}_n\}_n \sim \lambda \eta$ . Moreover, by adapting the argument used in the solution of [14, Exercise 3.1], it can be shown that  $\eta$  is the unique non-decreasing function defined on  $[0, 1]$  satisfying (A.3).

## References

1. Barbarino G (2017) Equivalence between GLT sequences and measurable functions. *Linear Algebra Appl* 529:397–412
2. de Boor C (2001) *A practical guide to splines*, Revised edn. Springer, New York
3. Böttcher A, Garoni C, Serra-Capizzano S (2017) Exploration of Toeplitz-like matrices with unbounded symbols is not a purely academic journey. *Sb Math* 208:1602–1627
4. Cottrell JA, Hughes TJR, Bazilevs Y (2009) *Isogeometric analysis: toward integration of CAD and FEA*. Wiley, Chichester
5. Cottrell JA, Reali A, Bazilevs Y, Hughes TJR (2006) *Isogeometric analysis of structural vibrations*. *Comput Methods Appl Mech Eng* 195:5257–5296
6. Donatelli M, Garoni C, Manni C, Serra-Capizzano S, Speleers H (2016) Spectral analysis and spectral symbol of matrices in isogeometric collocation methods. *Math Comp* 85:1639–1680
7. Ekström S-E, Furci I, Garoni C, Manni C, Serra-Capizzano S, Speleers H (2018) Are the eigenvalues of the B-spline isogeometric analysis approximation of  $-\Delta u = \lambda u$  known in almost closed form? *Numer Linear Algebra Appl* 25:e2198
8. Ekström S-E, Garoni C. A matrix-less and parallel interpolation–extrapolation algorithm for computing the eigenvalues of preconditioned banded symmetric Toeplitz matrices. *Numer Algor* <https://doi.org/10.1007/s11075-018-0508-0>
9. Garoni C (2018) Spectral distribution of PDE discretization matrices from isogeometric analysis: the case of  $L^1$  coefficients and non-regular geometry. *J Spectral Theory* 8:297–313
10. Garoni C, Manni C, Pelosi F, Serra-Capizzano S, Speleers H (2014) On the spectrum of stiffness matrices arising from isogeometric analysis. *Numer Math* 127:751–799
11. Garoni C, Manni C, Serra-Capizzano S, Sesana D, Speleers H (2017) Spectral analysis and spectral symbol of matrices in isogeometric Galerkin methods. *Math Comp* 86:1343–1373
12. Garoni C, Manni C, Serra-Capizzano S, Sesana D, Speleers H (2017) Lusin theorem, GLT sequences and matrix computations: an application to the spectral analysis of PDE discretization matrices. *J Math Anal Appl* 446:365–382
13. Garoni C, Mazza M, Serra-Capizzano S (2018) Block generalized locally Toeplitz sequences: from the theory to the applications. *Axioms* 7:49
14. Garoni C, Serra-Capizzano S (2017) *Generalized locally Toeplitz sequences: theory and applications (Volume I)*. Springer, Cham
15. Garoni C, Serra-Capizzano S. *Generalized locally Toeplitz sequences: theory and applications (Volume II)*. Springer (to appear)
16. Garoni C, Serra-Capizzano S, Sesana D (2015) Spectral analysis and spectral symbol of  $d$ -variate  $\mathbb{Q}_p$  Lagrangian FEM stiffness matrices. *SIAM J Matrix Anal Appl* 36:1100–1128
17. Garoni C, Serra-Capizzano S, Sesana D. Block generalized locally Toeplitz sequences: topological construction, spectral distribution results, and star-algebra structure. To appear in a volume of the Springer INdAM Series
18. Hughes TJR (2000) *The finite element method: linear static and dynamic finite element analysis*. Dover Publications, New York
19. Hughes TJR, Cottrell JA, Bazilevs Y (2005) *Isogeometric analysis: CAD, finite elements, NURBS, exact geometry and mesh refinement*. *Comput Methods Appl Mech Eng* 194:4135–4195
20. Hughes TJR, Evans JA, Reali A (2014) Finite element and NURBS approximations of eigenvalue, boundary-value, and initial-value problems. *Comput Methods Appl Mech Eng* 272:290–320
21. Hughes TJR, Reali A, Sangalli G (2008) Duality and unified analysis of discrete approximations in structural dynamics and wave propagation: comparison of  $p$ -method finite elements with

- k*-method NURBS. *Comput Methods Appl Mech Eng* 197:4104–4124
22. Lyche T, Manni C, Speleers H (2018) Foundations of spline theory: B-splines, spline approximation, and hierarchical refinement. In: Lyche T et al (eds) *Splines and PDEs: from approximation theory to numerical linear algebra*, Lecture Notes in Mathematics 2219, pp 1–76, Springer International Publishing
  23. Reali A (2006) An isogeometric analysis approach for the study of structural vibrations. *J Earthq Eng* 10:1–30
  24. Schumaker LL (2007) *Spline functions: basic theory*, 3rd edn. Cambridge University Press, Cambridge
  25. Serra-Capizzano S (2003) Generalized locally Toeplitz sequences: spectral analysis and applications to discretized partial differential equations. *Linear Algebra Appl* 366:371–402
  26. Serra-Capizzano S (2006) The GLT class as a generalized Fourier analysis and applications. *Linear Algebra Appl* 419:180–233
  27. Tilli P (1998) Locally Toeplitz sequences: spectral properties and applications. *Linear Algebra Appl* 278:91–120